Optimization of Cu_2ZnSnS_4 Absorber Layers via Sulfurization of Electrodeposited Cu-Zn-Sn Precursors for Photovoltaic Applications

---

A Dissertation

Presented to

the faculty of the School of Engineering and Applied Science

University of Virginia

---

in partial fulfillment

of the requirements for the degree

Doctor of Philosophy

by

Begum Unveroglu

August

2017

APPROVAL SHEET

The dissertation
is submitted in partial fulfillment of the requirements
for the degree of
Doctor of Philosophy

AUTHOR

The dissertation has been read and approved by the examining committee:

Giovanni Zangari
Advisor

Petra Reinke

Robert G. Kelly

Jerrold Floro

Joshua Choi

Accepted for the School of Engineering and Applied Science:

Craig H. Benson, Dean, School of Engineering and Applied Science

August
2017

Acknowledgments

My deep gratitude first goes to my PhD advisor, Dr. Giovanni Zangari, who guided me through my graduate education. His trust in me and my studies encouraged me to engage my work deeply. I am thankful for all his support and patient during the last five years.

I would like to thank my PhD. defense committee members Dr. Petra Reinke, Dr. Robert G. Kelly, Dr. Jerrold Floro and Dr. Joshua Choi for their dedication and effort in ensuring my PhD studies.

Great thanks to my sponsor, Minister of National Education of the Republic of Turkey, for giving me the opportunity to have a PhD. in United States and for all their support during the last five years.

My graduate extents to all UVA family, especially, to the CESE; I cannot thank enough for their support during my PhD. studies. Special thanks go to my group mates, Defu Liang, Lok-kun Tsui and Yin Xu whose research discussion and help improved my studies and made our lab full of happiness. In particular, I am grateful to Dr. Rakesh Agrawal and Dr. Mark Koeper from Purdue University for their discussion and help on the fabrication and the characterization of solar cells in this dissertation.

My appreciation also goes to my close friends and to the reminders of joy all around the world; I will not be able to finish my PhD. without your generous love and compassion.

Finally, I want to thank my family, my parents, Güngör and Okşan Ünveroğlu and my brother, Ogün, who have been incredibly supportive throughout my life with their guidance, patient and benevolent love.

Table of Contents

List of Tables

List of Figures

Abstract

Solar cells based on thin film absorbers provide an inexpensive and versatile technology to directly convert solar energy to electricity. Recent manufacturing developments have led to a significant decrease in the cost of solar energy, which has recently become lower than that of electricity from the grid, thus making this renewable energy option much more attractive. Kesterite solar cells comprised of a Cu_2ZnSnS_4 (CZTS) absorber layer are unique among thin film solar cell architectures since they are made up of earth-abundant, non-toxic elements, potentially enabling a widespread adoption of this technology, in contrast to current CdTe or Cu(In,Ga)Se2 which contain toxic elements. Unfortunately, CdTe and $Cu(In,Ga)Se_2$ achieve efficiencies above 20%, while the record efficiency of thin film solar cells based on CZTS absorber films is only 12%. A simple, inexpensive, and scalable method for growing CZTS absorbers is electrodeposition of Cu-Zn-Sn metallic precursor and sulfurization method; so far CZTS grown with this method however is still only around 5%, and the origin of this limitation is not understood. On the basis of this knowledge gap, this dissertation investigates in detail the electrochemical synthesis and characterization of CZTS absorber layers with the aim to achieve a highly uniform, single phase material with a high conversion efficiency and good stability.

Electrodeposition of Cu-Zn-Sn (CZT) films followed by vapor phase sulfurization is an environmentally friendly and practical method to grow kesterite Cu_2ZnSnS_4 (CZTS) absorber layers on Mo substrates. In this work we discuss the influence of CZT alloy composition, its compositional spread, and sulfurization parameters on the formation of secondary phases and structural inhomogeneity, which negatively affect the performance of CZTS layers.

The stoichiometric composition for Cu2ZnSnS4 is Cu: 25 at%, Zn: 12.5 at%, Sn: 12.5 % and S: 50 at%, however slightly off stoichiometric Zn-rich and Cu-poor CZTS films have been reported to give higher efficiency than the stoichiometric ones. The compositional ratios that best correlate

with performance in CZTS materials are the Zn/Sn and Cu/(Zn+Sn) ratio. Zn-rich films have Zn/Sn > 1.0 ratio and Cu-rich films have Cu/(Zn+Sn) < 1 ratio. Therefore, in our studies we target Zn-rich and Cu-poor CZTS films and for this purpose, we deposited Cu-poor CZT metallic precursors with different Zn/Sn ratios before sulfurization of the layers. Electrodeposition of CZT was carried out using two distinct chemistries: an acidic citrate solution and an alkaline pyrophosphate solution. The main difference between these two electrolytes was the reduction potential of zinc, which was deposited only after the hydrogen evolution reaction, significantly influencing the morphology of the CZT metallic precursors. In addition, the alkaline solution contained potassium, which acted as a growth modifier during the growth of CZTS films, increasing the size of the grains.

CZT alloys obtained from the acidic electrolyte were sulfurized at various temperatures and the influence of Zn/Sn ratio of the resulting CZTS layers on the film quality was studied. We found that Zn-rich (27-29%) and Cu-poor (47-49 at %) CZT metallic precursors formed fewer amounts of secondary phases and showed better crystallinity after sulfurization. Furthermore, CZTS layers with a higher Zn/Sn ratio showed improved photoelectrochemical (pec) response, up to 0.5 mA/cm^2 and 0.99 mA/cm^2 for sulfurization temperatures of 500 °C and 550 °C, respectively. The photoelectrochemical response was correlated to the phase purity and crystallinity of the CZTS, as determined from XRD and Raman Spectroscopy analyses.

In order to understand the influence of the electrodeposition current distribution on the standard deviation of the alloy composition, we deposited the CZT metallic precursors with a basic electrolyte, using vertical and horizontal deposition experimental set ups; the latter configuration avoided natural convection and thus enhanced flow uniformity. The compositional standard deviation of CZT metallic precursors did indeed decrease by using the horizontal deposition set up, and higher pec response was observed owing to the improved phase purity of the CZTS layers, as seen from compositional mapping of the films. Despite the improved uniformity however, the highest pec response (0.4 mA/cm^2) of CZTS films from the basic solution was lower than that of CZTS films grown from an acidic solution. Even though Raman spectra results showed similar crystallographic properties at the surface of the CZTS layers, XRD analyses suggested the presence of slightly more secondary phases for the bulk of the CZTS layers grown from the alkaline solution in comparison to the acidic solution, which was found to be the reason for lower pec performance.

In a parallel effort, we deposited CZT metallic precursors with the addition of small amounts of bismuth (< 1 at%, CZT-Bi) from an acidic citrate solution to investigate the dopant role of bismuth and its influence on the performance of CZTS based materials. These films showed the highest pec, 2.65 mA/cm^2, with the optimum amount of Bi (~0.5 at%) in Zn-rich CZTS layers. The increased pec response was attributed to the enhanced growth of the CZTS grains and improved phase purity with respect to CZTS films without any dopant addition.

Even though reasonably good pec responses were obtained with CZTS based films, the solar cell efficiency of the CZTS layers was less than 1%. The highest solar cell efficiency was 0.64% for CZTS films formed via sulfurization of CZT precursors grown from the acidic electrolyte. We found that the solar cell performance was compromised in presence of secondary phases, particularly the conductive phase Cu_xS_y , which lowered the short circuit current by acting as a shunt path. Time resolved photoluminescence and measurements of the external quantum efficiency also suggested the presence of a high density of recombination centers, which lowered the open circuit voltage, hence the efficiency of the CZTS based cells. Various possible solutions towards improved material and higher performance are also outlined.

Chapter 1-Introduction

I. Global Energy Needs and Thin Film Photovoltaics

The world population is about to reach 8-11 billion by 2050, and as a consequence the global energy consumption is estimated to double by that time [1]. World's increasing demand for energy is a concerning problem due to our significant dependence on carbon-based fossil fuels and the related need to increase the reliance on renewable and carbon neutral energy sources. The majority of the electricity generation worldwide (~ 85%) is currently provided from carbon-based fuels such as oil, natural gas, and coal[2, 3]. The remainder of energy use is generated from hydroelectricity, nuclear power and 2% of electricity from wind, solar, geothermal, and biomass[2, 3]. According to the IEA report Technology Roadmap: Solar Photovoltaic Energy, 16 % of the total power requirement could potentially be generated by photovoltaics (PVs) in 2050[4].

Photovoltaic devices absorb solar radiation (i.e. photons) at a semiconductor absorber, where a photon generates an electron-hole pair that is separated at a p-n junction, generating a photon induced current. PV solar cells are the fastest growing energy technology in the world and a leading candidate for Tera-watt scale and carbon-free electricity generation by the mid-century [5]. Solar cell technologies are usually classified in four distinct generations; the first generation includes the most mature version. i.e. the single crystal Si device; the second generation includes amorphous and polycrystalline and amorphous Si, as well as thin film absorber cells; the third generation comprises various advanced architecture such as quantum dots and dye sensitized solar cells; finally the fourth generation covers hybrid/inorganic crystals including the perovskites. Thin film solar cells are particularly important since the energy payback time in these systems is significantly decreased, owed to the enhanced light absorption that allows usage of lower amounts of raw material[6].

Unfortunately, only 1 % of the world’s electricity was provided from PVs in 2015[5]. In order to achieve 10% of energy generation, the market needs to significantly expand its capacity. The major obstacles towards widespread market expansion are the cost of conventional silicon-based solar cell and material resource limitations in thin film devices, where essential elements such as Te and Ga are expensive and in limited supply [7]. Crystalline silicon-based PVs are currently the dominant technology, due to their high power conversion efficiency and proven manufacturability[8]. However, even though the price of silicon based PVs has declined dramatically after 2010, the device cost may still be a hindrance to a robust PV market expansion.

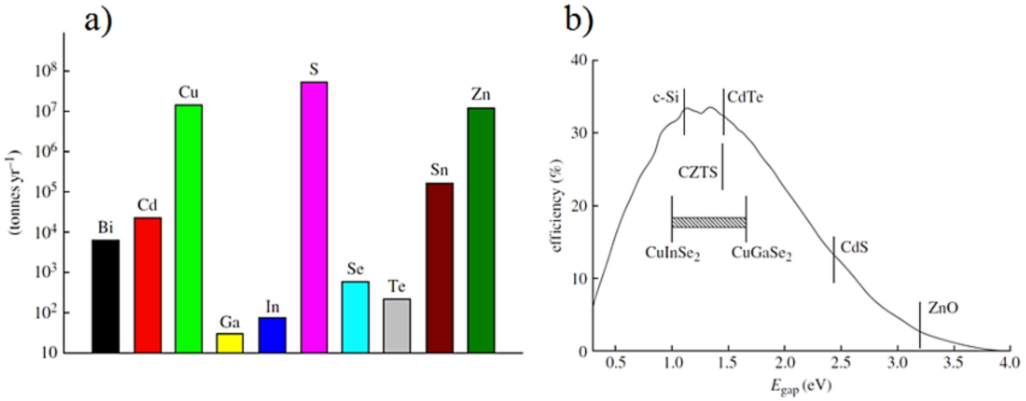

Figure 1.1a) Annual production of the main elements used in thin film solar cell manufacturing and b) efficiency vs. band gap graph for PVs from Ref. [9]

Currently, commercial thin film technologies are based on CdTe or CuInGaS(Se)$_2$ light absorbers[5, 6, 8, 10–12]. However, gallium, indium, and tellurium are in the list for supply risk, and their price is expected to increase over time **(Figure 1.1.a)** [9]. The market share for CdTe and CuInGaS(Se$_2$) based absorber layer thin film PVs is in fact most likely to be limited by the supply of indium and tellurium[9, 13]. Therefore, there is a need for an absorber layer consisting of earth-abundant elements for alternative thin film PVs. In **Figure 1.1.a,** the annual production of the main elements used in thin film solar cell manufacturing is shown. As it can be seen the most abundant elements are copper, tin, zinc, and sulfur, therefore it is important to use these elemental sources wisely to manufacture semiconductor materials suitable for PV applications. **Figure 1.1.b** shows the maximum theoretical efficiency of a solar cell calculated from the semiconductor band gap under AM 1.5 illumination [9]. The kesterite-phase $Cu_2ZnSn(S_xSe_{1-x})_4$ (CZTSSe), is within the desirable band gap range and has the potential to be an wide spectrum absorber layer for a high efficiency PV device (**Figure 1.1.b)**. In this dissertation we will only focus on CZTS materials, even if the CZTSSe exhibit higher efficiency; this is due to the Se being relatively scarce and toxic.

II. Cu_2ZnSnS_4 (CZTS) as Absorber Layer for Thin Film Photovoltaics

New generation PV devices made of materials containing earth-abundant elements include perovskites, polymers, quantum dots, and CZTS based solar cells [14–20]. For each of these, material complexity and manufacturing methods are bottlenecks towards the implementation of efficient earth-abundant based PVs. CZTS absorber layers in particular are characterized by a direct band gap, which is located in the optimum region of the solar spectrum (Fig. 1.1.b); these materials exhibit high absorption coefficient, and feature low cost and significant abundance of the raw elements[21–23]. With these properties, CZTS is considered to be one of the most promising next generation solar cells. The theoretical efficiency of CZTS based solar cells is as high as 30 % according to the Shockley-Queisser limit, however the proven efficiency of these devices are only around 13 % for a small area solar cell with a CZTSSe absorber [24, 25].

To understand the reasons behind the low efficiency of CZTS cells, it is important to first consider the basic operation of a solar cells. A solar cell transforms solar radiant energy directly into the electrical energy by using a semiconductor based device. A typical solar cell architecture of a CZTS based solar cell is shown in **Figure 1.2.a**; the same architecture is shared by high efficiency CIGS solar cells[26]. A p-n junction is made by depositing a n-type CdS film onto the p-type CZTS absorber. Photons having energy higher than the band gap are absorbed by the semiconductor absorber layer and generate an electron-hole (e-h) pair that populate energy levels above the conduction band and below the valence band, respectively. The electron and hole are separated at the p-n junction by the built-in potential generated by the difference in chemical potential of electrons and holes. Far from the p-n junction the charge carriers drift in opposite directions; recombination processes may occur due to scattering processes or the presence of a series of defects; important types of defects in CZTS will be discussed in the following. Eventually, the electrons and holes will be injected in the external circuits to generate the output current. Other components necessary in a solar cell include the window layers (wide band gap materials such as ZnO and ITO), the back contact (Mo/lime glass) and the front contact (Ni/Al metal grids).

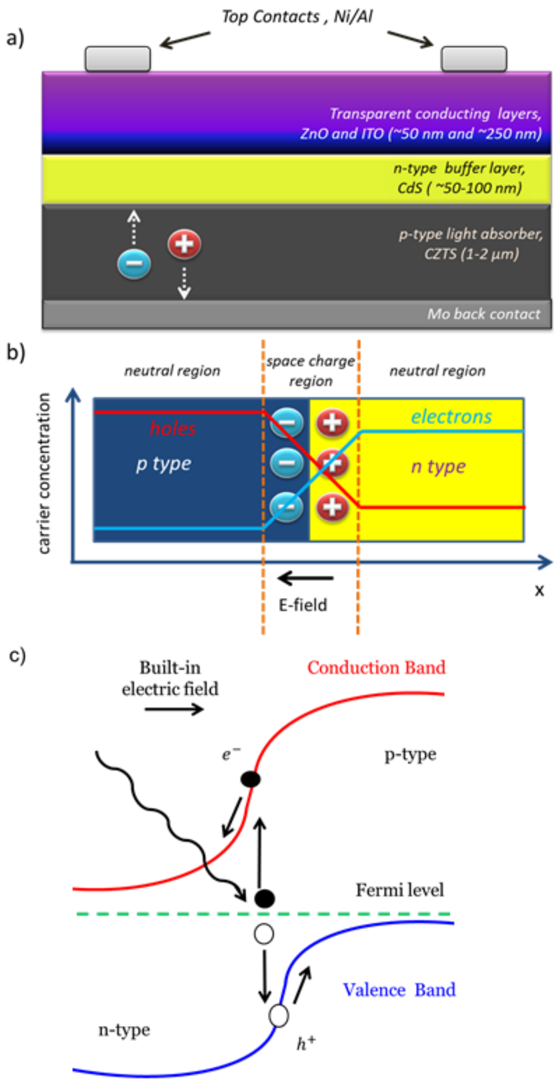

Figure 1.2 a) CZTS absorber layer based solar cell structure, b) p-n junction in thermal equilibrium and c) electronic structure of the p-n junction together with schematics of light absorption as well as of electron-hole separation and drift.

Since the absorber layer is the site where electron-hole pairs are generated and successively diffuse to the p-n junction, it is, the key component that determines the efficiency limitations. The drawbacks of the CZTS absorber layers in enabling a long free path for the minority carriers are unique structural inhomogeneities, such as the coexistence of ordered and disordered type kesterite phase, and phase inhomogeneity due to the narrow equilibrium stability region of pure CZTS [27–29]. Besides the above issues, there are some obstacles related to solar cells manufacturing, such as the ability to grow a continuous film without pinholes to prevent shorting the solar cell circuit. In addition, a high quality growth process becomes even more challenging when attempting to grow phase pure CZTS films with large grains of ordered type kesterite on a suitable substrate to manufacture solar cells, all being important characteristics for an efficient device.

A. Crystallographic Properties of CZTS Layers

The quaternary compound CZTS can crystallize in a zinc blende-derived structure similar to that of CdTe and CIGS(e) [30]. CZTS may adopt this structure, which is formed by substituting the In/Ga sites in CIGS(e) with Zn and Sn atoms[30]. However, at variance with CIGS(e), Cu_2ZnSnS_4 phase can also crystallize as kesterite (space group $I\bar{4}$) , stannite (space group $I\bar{4}2m$) or as disordered kesterite (space group $I\bar{4}2m$) [31–33] (Figure 1.3). In this section, first we will look at the structural differences between kesterite and stannite and then at the differences between ordered and disordered kesterite.

The modifications between kesterite and stannite are due to the alternation of the cation and anion positions. The kesterite type structure is characterized by the presence of alternating cation layers of Cu-Sn, Cu-Zn, Cu-S and Cu-Zn at z=0, 1/4, 1/2 and 3/4 respectively (**Figure 1.3.a** and **1.3.b**). On the other hand, Zn-Sn layers alternate with Cu_2 layers in the stannite type structure. Sn is located at the same structural site in both types of the structure. The anion in the kesterite type structure occupies a (x,y,z) position whereas anions in the stannite type structure lie on the (110) mirror plane of that (x,y,z) position.

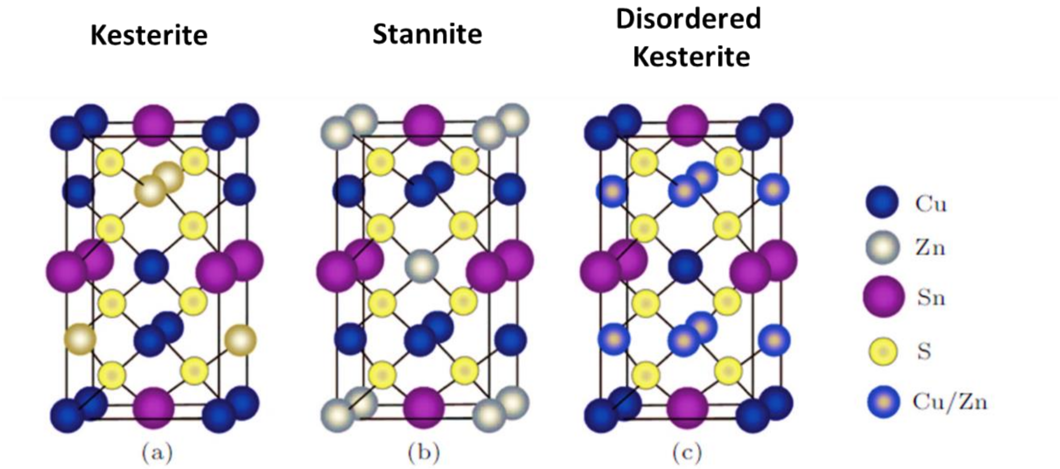

Figure 1.3 CZTS a) Kesterite type and b) stannite type and c) disordered kesterite type structures. Taken from Ref [33]

Distinguishing kesterite type and stannite type structures with conventional X-ray diffraction method is almost impossible, because the main Bragg peaks are the same due to the similar structural configuration. [29] The only difference between the two phases consists in the additional reflections which occur due to the ordered distribution of cations (the superstructure reflections). However, these reflections have low intensity and they may not be detected for some CZTS materials. The strongest superstructure peak is the (101) Bragg peak at around 2θ = 18° using a CuKα radiation[34]. The kesterite phase is more stable than the stannite phase, but the former has a free energy only a 3.2 kJ/mol (formula unit)$^{-1}$ more negative than the latter [34, 35] Since this difference is relatively low the formation of both structures is likely, and it is beneficial to investigate the superstructure peaks in addition to the main Bragg reflections to clearly distinguish between the two.

Neutron diffraction could better discern the position of Cu and Zn, and therefore determine anti-site defects in the CZTS materials, allowing to estimate the fraction of disordered kesterite (**Figure 1.3.c**). As seen in **Figure 1.3**, this phase is slightly different from either the kesterite or stannite structures. The schematics for the ordered and disordered kesterite structures are shown in **Figure 1.4**. In the disordered kesterite structure, the 2c and 2d Wyckoff sites at the z=0.25 plane are randomly occupied by Cu^+ and Zn^{2+} ions. If there is complete disorder, the crystal adopts a new symmetry $I\bar{4}2m$ instead of ordered kesterite $I\bar{4}$ [28].The band gap of the disordered kesterite in addition is lower than that of ordered kesterite, therefore, characterization and analysis of the disordered kesterite structure is important, since light absorption will vary [28].The characterization of disordered kesterite is in alternative possible by the analysis of the peak width and intensity from Raman spectra. Detailed characterization analysis is discussed in Chapter 2.

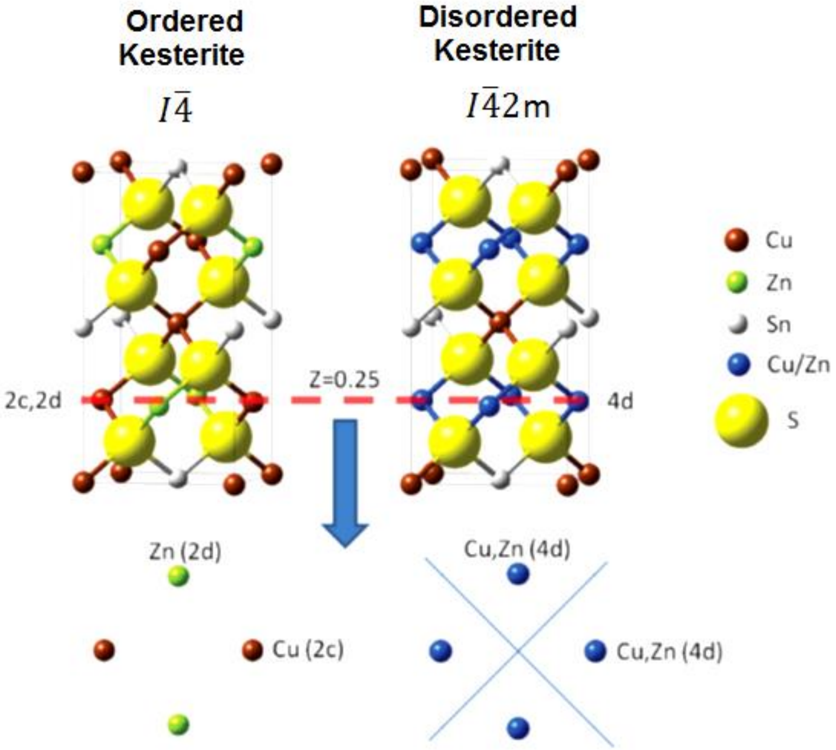

Figure 1.4 Ordered and disordered kesterite structures with a projected view of the z=0.25 plane at the bottom. Taken from Ref [36].

B. Equilibrium Conditions for Kesterite and Formation of Secondary Phases

Thin film solar cells with polycrystalline CZTS materials require a single-phase kesterite absorber layer in order to achieve high efficiency. **Figure 1.5** shows an isothermal section of the phase diagram for the Cu_2S-SnS_2-ZnS system at 670 K, suitable to form kesterite by for example solution-based methods. The thermodynamically stable region for Cu_2ZnSnS_4 is in the center of the ternary diagram, labeled as **1**. This phase pure region for CZTS is thermodynamically stable in a small compositional range at the above temperature. Outside of this region various secondary phases can form besides the primary phase CZTS. Therefore, composition control of CZTS materials during synthesis is crucial.

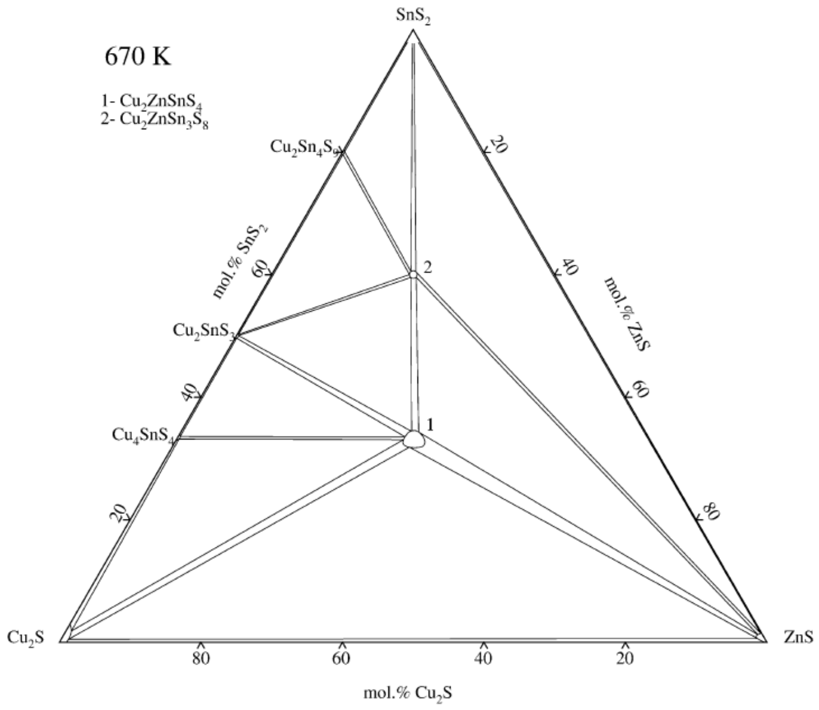

Figure 1.5 Isothermal section of the Cu_2S-SnS_2-ZnS system at 670 K, taken from Ref [37]. The region (1) in the center is the region of thermodynamic stability of kesterite CZTS.

The most common binary and ternary secondary phases are also shown in **Figure 1.5**. The presence of these secondary phases has distinct influences on the device performance. **Table 1.1** shows the properties of some of the binary and ternary phases that are present at the synthesis conditions above. Also, the quaternary compounds of the Cu-Zn-Sn-S system are not limited to the Cu_2ZnSnS_4 phase, but include also another quaternary phase $Cu_2ZnSn_3S_8$[37], of which few reports are available.

Ternary compounds derived from the Cu-Zn-Sn-S system include the Cu-Sn-S subsystem[29, 37–39]. Other subsystems such as Cu-Zn-S and Zn-Sn-S should thermodynamically form binary phases such as Cu_2S and ZnS for the former subsystem, and ZnS, SnS_2 for the latter subsystem[37, 40]. The $Cu_xSn_yS_z$ (CTS) ternary phases include $Cu_2Sn_3S_7$, Cu_3SnS_4 and Cu_2SnS_3, which can be formed at temperature as low as 350 °C, and can be stable at temperatures as high as 700 °C [38, 41, 42]. The most common ternary phase observed in CZTS films is Cu_2SnS_3 (CTS) which has a band gap around 0.8-1.35 eV. A narrower band gap of the CTS phase in comparison to CZTS would lower the solar cell efficiency due to the limited absorption. Therefore, the presence of this phase is detrimental to the solar cell performance.

Binary systems include the most common secondary phases of the Cu-Zn-Sn-S system. [20, 39, 43–45]. The Sn-S subsystem includes three possible phases: SnS, Sn_2S_3, SnS_2; all these phases can be present between room temperature and 600 °C [46–48]. The SnS phase usually presents a flake shape when present at the surface of CZTS. This is a problem, because in the presence of these features the CdS layer may not fully coat the CZTS surface due to the rough morphology of these flakes.

The ZnS phase may exist in a wide range of temperatures with polymorphic phases from room temperature α-ZnS to β-ZnS above 1020 °C[49–51]. The presence of ZnS in CZTS films lowers the open circuit voltage and stifles charge collection due to (i) its relatively high band gap with respect to CZTS and (ii) misalignment of the band structure and the presence of a quantum well that may favor recombination [52]. Finally, Cu-S presents binary phases with distinct stoichiometry at different temperatures [37, 53]. Monoclinic Cu_2S is stable from room temperature up to 103.5 °C and hexagonal Cu_2S exists up to 435 °C [53, 54]. The Cu-S phase becomes Cu-poor and forms $Cu_{2-x}S$ phases at higher temperatures. Cu-S is the most detrimental secondary phase with regard to device performance, especially if it extends throughout the film thickness and is in contact with the substrate. In this case in fact, it may form high conductivity pathways due to the small band gap of $Cu_{2-x}S$ phases[55].

Table 1.1 Enthalpy of formation, crystallographic space group, and band gap, for CZTS and some of the common secondary phases. Enthalpies of formations are reported at 298.15 K and 1 bar pressure [47, 55–61]

Phase	**Enthalpy of Formation** $\Delta H_f^o (kJmol^{-1})$	**Space Group**	**Band Gap** (eV)
Cu_2ZnSnS_4	-396.13	$I\bar{4}$	1.49-1.64
$Cu_{2-x}S$	-46.24	$P2_1/c$	0.5-1.21
ZnS	-156.74	$F\bar{4}3m$	3.7
SnS	-97.70	$Pnma$	0.9-1.35
SnS_2	-120.97	$P\bar{3}m1$	2.2
Cu_2SnS_3	-	$Cc, P1, I\bar{4}2m$	0.8-1.35

The composition of CZTS films is also important in determining the performance of photovoltaic devices. Champion CZTS based solar cells devices with high efficiency suggest that absorber layers with Zn-rich (Zn/Sn~1.2) and Cu-poor (Cu/(Zn+Sn)~0.8) composition perform better than the stoichiometric (Cu/(Zn+Sn)=1 and Zn/Sn=1) or Sn–rich (Zn/Sn<1) ones. The science behind CZTS defect chemistry is still not clear and there are only a few studies on the defects of kesterite based materials; nonetheless, some arguments for this behavior can be given. The high efficiency of Zn-rich and Cu-poor layers is attributed to the formation of shallow donor and acceptor levels. The point defects formed in Zn-rich and Cu-poor materials are the Cu vacancy (V_{Cu}) and Zn antisites (Zn_{Cu} and Zn_{Sn}), generated by the following reactions; $2Cu \rightarrow Zn_{Cu} + V_{Cu}$ and $2Cu+Sn \rightarrow 2Zn_{Cu}+ Zn_{Sn}$. **Figure 1.6** shows the ionization levels of intrinsic defects in the bandgap of CZTS. As shown in the figure, the acceptor V_{Cu} and Zn_{Sn} and the donor Zn_{Cu} are shallow level defects and are relatively less detrimental comparing to defects such as Sn_{Cu} or Cu_{Sn}, which form deep trap states within the band gap of the absorber layer[26].

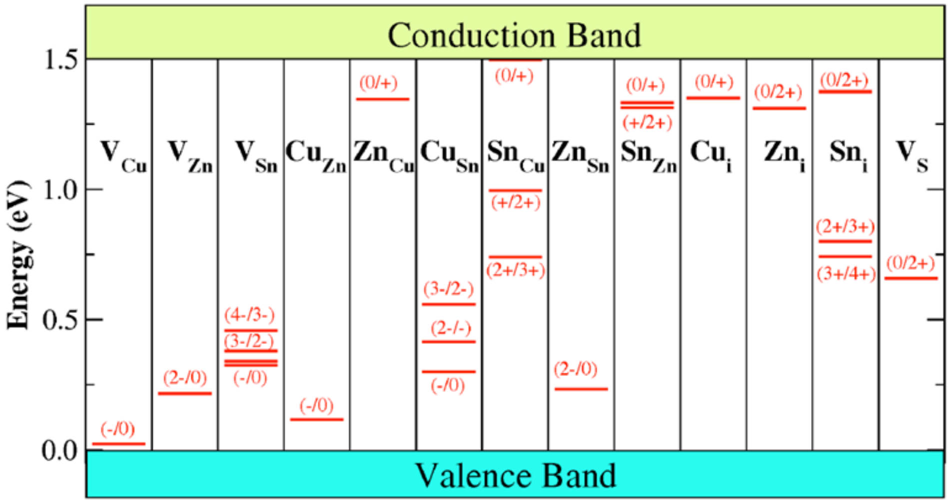

Figure 1.6 The ionization levels of intrinsic defects in the bandgap of CZTS, taken from Ref [62].

In summary, compositional control during the synthesis of CZTS is indispensable to avoid the formation of secondary phases and to obtain semiconductor absorbers with suitable compositional ratio and therefore appropriate electronic properties.

C. Characterization and Synthesis Problems of CZTS Absorber Layers

An absorber material for photovoltaic applications should possess some general properties in order to achieve high efficiency devices. First, the polycrystalline material should be comprised of densely packed, single phase large grains, preferably spanning the entire film thickness to limit grain boundary scattering.

Second, the layer should be continuous, with a low resistance contact with the interfaces at the back and front contacts. These features have been actually achieved for the chalcogenide based solar cells (CIGS) which exhibit ~20 % efficiency[63]. Unlike CIGS materials, CZTS struggles to achieve the CIGS properties as a solar absorber layer. As a consequence, current investigations on CZTS focus on improvement of the bulk material quality and on achieving better layer interface contact at the front and back surfaces, i.e. CZTS/CdS and CZTS/Mo respectively.

Beyond the issue of growing phase pure kesterite CZTS, the identification of secondary phases and the analysis of crystallographic properties are concerning problems, because of the similar crystallographic symmetry properties of the primary phase CZTS and secondary phases (**Table 1.1**). At least two structural characterization techniques, X-ray diffraction and Raman Spectroscopy should be utilized in the assessment of the kesterite structure. Unfortunately, the information available from these methods has still some limitations; specifically, XRD alone is not enough to identify all of the secondary phases, while Raman Spectroscopy can only give information up to a depth of about few hundred nanometers. Therefore, in order to improve kesterite based devices, phase purity and crystallographic properties need to be analyzed and reported systematically.

Improvement of bulk quality of the CZTS films alone is not sufficient to achieve high efficiency devices. The instability of the layer interfaces at the front and back contacts are crucial for the efficiency of kesterite based solar cell. The standard metallic back contact for CZTS(Se) absorber layers is molybdenum[64]. However, the formation of MoS_2 at the interface between the CZTS layer and molybdenum during annealing has been reported; this degrades the performance by decreasing the quality of the electric contact [64]. A thermodynamic study also suggests the formation of other binary phases at the back contact during the formation of MoS_2 [64].The formation of these secondary phases may create a non-Ohmic back electrical contact and increase recombination. This instability at the back contact limits the available range of synthesis conditions, for example the duration and temperature of the heat treatments for CZTS layers on Mo back contact. The interface between the absorber and the buffer layers also strongly influence the cell performance. The electrical contact quality at the interface between CZTS and CdS depends on the relative energy band positions of the two layers. Since the band gap of the CZTS material is varying due to compositional changes, spatial variations of the band gap at the p-n junction could generate a potential additional barrier to prevent charge carrier flow. Therefore, device grade CZTS layers should also present phase pure surfaces with relatively smooth morphology to avoid recombination, use the widest possible Sun light spectrum, and exhibit good adhesion of the successive layers such as CdS and ZnO.

III. Formation of CZTS via Electrochemical and Sulfurization Methods

CZTS films can be grown by vacuum based processes such as thermal evaporation, electron beam evaporation and sputtering, and by non-vacuum based methods such as spin coating of precursor solutions, sol-gel deposition and chemical synthesis of nanocrystal solution[26, 65–67]. Electrodeposition is an advantageous alternative and a simple method for the synthesis of metallic precursors for CZTS. First attempts to grow CZTS from metallic precursors following chalcogenization were reported by Araki et al and Scragg et al. in late 2010[68, 69]. A significant performance improvement was achieved with 7.3% efficiency for electrodeposited kesterite devices in 2012 by Deligianni et al[70]. Further increase in efficiency was obtained with pre-annealing of sequentially deposited Cu/Sn/Zn layers for pure sulfide CZTS thin film with 8.4% efficiency and 8.2 % efficiency for metal stacks after selenization[71, 72]. The promising performance increase for electrodeposition routes reinforces the importance of this method to manufacture CZTS layers for photovoltaic devices.

In our study we used an alloy electrodeposition route for the synthesis of metallic precursors, followed by vapor phase sulfurization. This method has some advantages compared to stacking elemental layer deposition and chalcogenide co-electrodeposition. Stacking of single metal layers lacks in-depth compositional homogeneity, even after annealing. Therefore, an extra pre-annealing step is required for the intermixing of elemental layers by this method[73]. Alternatively, direct electrodeposition of the chalcogenide compound (Cu-Zn-Sn-S) requires long deposition times and the electrolyte stability is often less comparing to electrolytes for metal alloy deposition [73]. On the other hand, metal alloy deposition for Cu-Zn-Sn metallic precursors provides a better in-depth compositional homogeneity. This method is also advantageous from the industrial standpoint because it reduces the production cost as well as chemical waste. Besides, electrodeposition takes place only in one bath, avoiding intermediate cleaning or rinsing.

Most of the studies on Cu-Zn-Sn metallic precursor layers used sodium citrate or pyrophosphate based solutions [74–85]. In these studies, deposition was carried out on Mo foil or Mo coated soda lime glass (SLG) substrates. The growth mechanism of Cu-Zn-Sn from a sodium citrate based solution was studied to investigate the influence of hydrogen evolution reaction (HER) on the composition[85]. In this study, a layer consisting of CZT with columnar grains on Mo/SLG was obtained on a 0.2 cm^2 area from a tri-citrate based solution. Kondrotas et al used hydroquinone besides sodium citrate in the electrolyte to grow Cu-Zn-Sn metallic layers [86], reporting the local delamination of Mo layer and the presence of large voids at the Mo/CZTSe back contact interface[86]. Gougaud et al. achieved 5.6 % efficiency with the selenization of dendritic Cu-Zn-Sn metallic layers grown from a citrate based solution. Even though the morphology of the layer was non-uniform, with dendrites of different lengths varying between 1-10 micrometer thickness, CZTSe layer achieved one of the highest efficiency of its class[87]. Another citrate based solution study by Zhang et al reported 4.5% efficiency via the sulfurization of Cu-Zn-Sn precursors with Zn-rich and Cu-poor initial and final composition[84]. Better CZTS surface roughness and denser layers were obtained with pyrophosphate based electrolytes [78, 88]. Ennaoui et al. fabricated a dense polycrystalline CZTS layer with smooth surface which gave 3.6 % efficiency after the sulfurization of Cu-Zn-Sn metallic precursors from a pyrophosphate electrolyte along with some additives[78].

To our best knowledge, this efficiency is one of the highest CZTS efficiency obtained by using co-electrodeposition and sulfurization method. The increased efficiency is attributed to the desirable morphology of the absorber layer, which is obtained by using an alkaline electrolyte. However, the presence of ZnS and Cu_2SnS_3 in the bulk of the film and at the back contact reduced the cell efficiency.

Although there are various advantages and reports about the metal alloy deposition route, the efficiency of CZTS layers obtained by this method is still only ~3.4 %, which is ~ 5% lower than CZTS layers obtained through other electrochemical routes [78, 84, 87, 89]. The low open circuit voltage observed in these CZTS materials is attributed to the presence of secondary phases and structural inhomogeneities, which arise from non-uniform compositional distribution[26, 29, 90]. Even though there are various studies on the co-electrodeposition of Cu-Zn-Sn for CZTS absorber layers, the influence of compositional deviation of the precursor material and structural inhomogeneity of CZTS achieved with this method has not been reported so far. Developing a rigorous correlation between compositional distribution and functional properties of the absorber layer is necessary in order to identify current limitations of these materials and overcome existing performance targets. To fill this gap in the field, in this dissertation we investigate in detail the influence of compositional values and elemental distributions of the initial CZT metallic precursors on the phase purity and crystal quality of the CZTS films on Mo substrate for PV applications.

IV. Objectives of This Study

The formation of CZTS layers via gas phase sulfurization of Cu-Zn-Sn metal alloy precursors has been discussed in the literature; comparatively less attention has been devoted to understanding the influence of compositional deviation of the precursor material on the phase purity and performance of CZTS layers for PV applications. In this dissertation, we seek to understand the influence of initial compositional properties of electrodeposited Cu-Zn-Sn metallic precursors on the final properties and performance of CZTS layers. For this purpose, we focused first on developing a correlation between the compositional distribution of electroplated CZT films, the extent of phase purity of CZTS layers and the photoelectrochemical response as a proxy for the efficiency of the final solar cell. In this effort we used metallic alloys grown from both acidic and basic electrolytes to compare the compositional deviation and morphological properties of the CZT layers on CZTS films. Successively, we optimized the influence of sulfur amount, sulfurization time and processing temperature for Cu-Zn-Sn metal alloys. Composition analyses and structural characterization methods such as X-ray diffractometer and Raman Spectroscopy were used to investigate the nature and amount of secondary phases, as well as to evaluate the presence of disordered type kesterite in the material. Photoelectrochemical response of the CZTS layers was measured to understand and quantify the photoactivity under simulated solar light. Third, in an effort to further increase the performance of the layers, we investigated the influence of Bi additions into CZTS layer on phase purity and crystal quality. In this effort, we did grow a quaternary Cu-Zn-Sn-Bi alloy with small Bi fraction in order to incorporate Bi into Cu-Zn-Sn. Lastly, we assembled model CZTS-based solar cells and measured the current-voltage characteristics to quantify the solar cell performance, understand their limitations, and gathered insight on the correlation between photoelectrochemical response and solar cell performance.

Chapter 2-Experimental Details and Material Characterization

The characterization methods for the CZT precursor alloys and CZTS absorber layers are described in this chapter. Major characterization methods are X-ray diffraction (XRD), energy dispersive spectroscopy (EDS), scanning electron microscopy (SEM), Raman spectroscopy, photoelectrochemical response and solar cells current density vs. voltage characteristics.

2.1 Electrochemical Methods for Precursor Synthesis and Characterization

Electrodeposition is a versatile and simple method to synthesize metals and alloys; this section focuses on the fundamentals of electrochemical deposition (electrodeposition) of metallic ions in an aqueous solution.

A. Fundamentals of Electrochemical Deposition

Electrodeposition can be performed in aqueous solutions, organic solvents, molten salts and recently in ionic liquids[91–93]. In this work, we focus on electrodeposition from aqueous solutions using a three electrode cell to enable potential control of the deposition process. **Figure 2.1** shows a schematic figure of a three electrode set-up consisting of a cathode, an anode and a reference electrode; a potentiostat monitors and controls the voltage applied at the cathode, measured with respect to the reference electrode. During electrodeposition metal ions are reduced at the cathode-electrolyte interface and incorporated into the growing metal film.

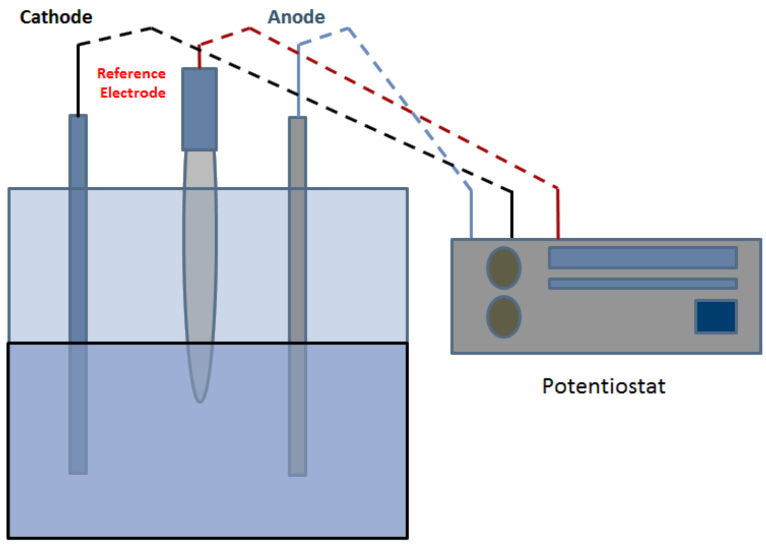

Figure 2.1 Schematics of a three electrode cell with a potentiostat

The following reaction describes the electrodeposition of a metal from a simple solution (i.e. the metal ion is bound only to water molecules) for a metal ion Me^{z+}.

$$Me^{z+} + ze^{-} \leftrightarrow Me \tag{2.1}$$

If the solution contains a complexing agent L the reaction can be expressed as follows,

$$[Me_xL_y]^{z+} + ze^{-} \leftrightarrow xMe + yL \tag{2.2}$$

Complexing agents bind to metal ions and decrease their effective concentration, enabling tailoring of the redox potential. These reactions occur at the electrode-electrolyte interface, which is the heart of the electrodeposition process. Once the cathode is immersed into the electrolyte a dynamic equilibrium between metal ions in solution and metallic atoms at the electrode will be established; this equilibrium entails a voltage drop between the electrolyte and the cathode, resulting in a separation of charges and forming a so-called double layer. Once the interface charge layers are formed under equilibrium conditions, two types of process can occur upon applying a potential.

1) *Faradaic processes*, where electrons are transferred across the electrode-electrolyte interface to enable reduction or oxidation reactions, governed by the Faraday's law.

2) *Non-faradaic processes,* whereby the structure of the double layer can change due to adsorption or desorption of ions or molecules, dependent on the applied potential.

While non-faradaic processes are important on their own, in this study we focus on Faradaic processes at constant potential. At equilibrium, the redox potential for a metal ion species is specified by the Nernst equation:

$$E_{eq} = E_o + \frac{RT}{zF} lna(M^{z+}) \tag{2.3}$$

where

E_o= the standard electrode potential

R= the gas constant

F=Faraday constant

a=activity of metal ions

z=numbers of electrons involved in the reaction

At this value of the electrode potential the equilibrium is dynamic, resulting in zero overall current. By applying a potential more negative than the Nernst potential a driving force is generated, inducing metal ion reduction.

B. Electrodeposition of Cu-Zn-Sn (CZT) Alloys from a Single Electrolyte

Electrochemical deposition of metal alloys from a single electrolyte involves the simultaneous reduction of different metal ions, each characterized by their own Nernst potential and reduction kinetics. In this work we aim to deposit Cu-Zn-Sn alloys with a suitable composition, as discussed in Chapter 1, that later will undergo desulfurization to form the CZTS compound. The rate of deposition of each element is described approximately by a Tafel relationship $j = j_0 \cdot e^{-zaFh/RT}$ that relates the current density j with the overpotential $h = E_{app} - E_0$, where E_{app} if the applied potential. Note that the Tafel relationship is valid only up to the limiting current j_L =

zFcD/δ, where D is the ion diffusion coefficient and δ is the diffusion layer thickness, corresponding to the maximum possible reduction current. These reduction reactions are reported below, together with the reduction potentials of the Cu^{2+}, Zn^{2+} and Sn^{2+};

$$Cu^{2+}+e^{2-} \rightarrow Cu^{o} \qquad +0.324-0.128ln\left(\frac{1}{[Cu^{2+}]}\right) \tag{2.4}$$

$$Sn^{2+}+e^{2-} \rightarrow Sn^{o} \qquad -0.138-0.128ln\left(\frac{1}{[Sn^{2+}]}\right) \tag{2.5}$$

$$Zn^{2+}+e^{2-} \rightarrow Zn^{o} \qquad -0.762-0.128ln\left(\frac{1}{[Zn^{2+}]}\right) \tag{2.6}$$

Note that alloy composition may be tailored by varying the metal ion concentration (shifting the redox potential) and the applied potential. The reduction potential of Cu^{2+} is the most positive, while the reduction potential of Zn^{2+} is the most negative, with ~ 1 V difference. This wide difference between reduction potentials in the Cu-Zn-Sn deposition system restricts the deposition conditions to obtain suitable compositions, Cu ~50 at %, Zn 25 at% and Sn ~25 at%. Since the reduction potential of the Zn is the most negative, electrodeposition of CZT must take place at potentials more negative than Zn itself. Usually, complexing agents or additives are used to narrow the difference between the reduction potential and increase the stability of the electrolyte; however in our experiments we do not use additives in order to avoid impurities such as carbon, N or H in the film. In our experiments, we used both acidic and basic solutions to investigate the compositional deviation of the elements in two different electrolytes. We use two different electrolytes with distinct pH to control the interfering reactions of the hydrogen evolution reaction (HER) and reduction of Zn ion ($\mathrm{E^{o}_{Zn}} \sim -0.76\ \mathrm{V_{SHE}}$).

In aqueous solutions water can be reduced to hydrogen gas at the cathode if the applied voltage is sufficient negative. The HER reactions for acidic and alkaline solutions are respectively

$$H^{+}_{(aq)}+e^{-} \rightarrow \frac{1}{2}H_2 \tag{2.7}$$

$$H_2O+e^{-} \rightarrow H_{(g)}+OH^{-}_{(aq)} \tag{2.8}$$

The reduction potential for HER according to the Nernst equation as function of pH is,

$$E_{H_2} = E_{H_2}^{o} - \frac{RT}{F} ln \frac{1}{a_{H^+}} \tag{2.9}$$

and as a function of pH it is,

$$E_{H_2} = E_{H_2}^{o} - 0.059pH \tag{2.10}$$

The HER create large amount of hydrogen bubbles at the electrode that can decrease deposition efficiency, influence the deposit morphology, thickness distribution, as well as composition, particularly compositional deviations of zinc metal across the substrate. The influence of HER on the film properties will be discussed in the following chapters.

Electrodeposition conditions must be selected to grow films with uniform in-plane compositional distribution and uniform thickness. The compositional and morphological properties of the co-deposited layers depend on the various parameters such as reduction potential of each metal, solution pH, and concentration of the metal ions.

2.2 Main Characterization Methods

A. Cyclic Voltammetry (CV)

The electrochemical behavior of electrolytes for Cu-Zn-Sn metallic precursors is characterized by CV. We used molybdenum foil as a substrate for all depositions. Before deposition, the Mo foils were sequentially cleaned in acetone, isopropanol, and ethanol (30 minutes each), then etched in 25 vol% NH_4OH solution for 3 minutes, rinsed and used immediately thereafter. After etching molybdenum substrates are immersed into the Cu-Zn-Sn electrolyte, then the potential is scanned, starting at 0.1 V more positive than the open circuit potential (OCP), going in the cathodic direction to a preset potential and then turning back to the starting potential. The current is recorded as a function of the scanning potential and from that curve the onset of deposition and hydrogen generation are obtained.

B. Compositional and Morphological Analyses

High magnification morphology investigation is possible with electron microscopy techniques. In the Scanning electron microscope (SEM), a beam of electrons are focused by a series of magnetic lenses. Secondary electrons emitted at the sample surface are picked up by a detector as the SEM rasters the beam across the sample, which a computer analyzes to create an image. If sufficiently energetic electrons interact with a solid, excited electrons go into higher energy levels and release characteristic x-rays as they return to their ground states. The information by this X-ray signal is originated from an interaction with about 1 μm deep below the surface, dependent on the acceleration voltage. Different elements can be detected with these X-ray signals as fingerprints and can be used for compositional analysis in energy dispersive spectroscopy (EDS).

C. X-ray Diffractometer for Phase Identification

Phase identification in kesterite based materials with standard laboratory techniques such as X-ray diffraction and Raman spectroscopy can identify most of the secondary phases directly. X-ray diffraction gives information on the crystal structure and the lattice constants of the phases present by analyzing the angular dependent diffraction pattern of the X-rays incident on the crystal. The specific angles of reflection where Bragg's Law is satisfied is given by;

$$2d\sin\theta = n\lambda \qquad (2.11)$$

In this equation d represents the spacing between crystal planes, θ is the angle of incidence, n is any positive integer, and λ is the wavelength of x-ray radiation. The instrument used was a Panalytical X'Pert MPD X-ray diffractometer with a Cu Kα radiation of λ = 1.54 Å. The XRD PDF Number 04-017-3032 for the kesterite phase was used in our analyses[94].

For the calculation of lattice parameters of a tetragonal structure we used the equation below:

$$\frac{1}{d^2} = \frac{(h^2+k^2)}{a^2} + \frac{l^2}{c^2} \qquad (2.12)$$

Here, a and c are lattice parameters, (h,k,l) are the Miller indices, and d, is the interplanar lattice spacing. The grain size of the CZTS films is estimated by using the Scherrer equation[95].

$$D = \frac{0.9\times\lambda}{\beta cos\theta} \qquad (2.13)$$

D is the crystallite size in nanometers, λ is the wavelength of the radiation for Cu K_α radiation and θ is the peak position. The lattice constant and spacing between planes depend on the crystal symmetry, therefore characterization of the secondary phases in Cu-Zn-Sn-S system with similar crystallographic structures can be challenging. Among them, SnS, SnS_2 and $Cu_{2-x}S$ can be discernible from CZTS directly without much difficulty[29, 54] (**Figure 2.2**).

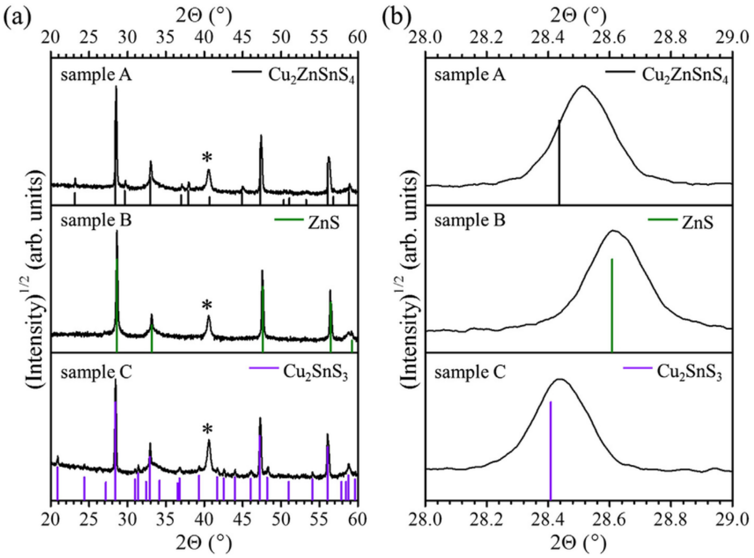

Figure 2.2 Taken from the Ref [96], a) XRD patterns of the most common secondary phases, CZTS, ZnS and Cu_2SnS_3 and b) the enlarged XRD patterns of corresponding phases with the differing peak positions of CZTS (112), ZnS (111) and Cu_2SnS_3 (131) peaks at around 28.5°

However, other most common secondary phases such as ZnS and Cu_2SnS_3 cannot be identified or can only be determined above a certain volume fraction. Berg et al. reported that XRD cannot be used to identify $< 10\%$ ZnS or $< 50\%$ Cu_2SnS_3 in a mixed Cu_2ZnSnS_4 sample [29]. Even though the full width at half maximum(FWHM) of the crystals can be measured from the X-ray diffraction patterns, the secondary phases present at around 28.5° for the most intense peaks, prevent us from using this technique to fully understand the crystal quality of the kesterite based layers. The detection limits of secondary phases with X-ray diffraction leads us to use other phase characterization techniques like Raman Spectroscopy to better understand the phase purity and the crystal quality.

D. Raman Spectroscopy for Phase Identification

Raman spectroscopy is an optical non-destructive technique where a laser at low power is used to excite atomic excitations in materials [97]. In this method, the analysis is based on the inelastically scattered electromagnetic radiation by crystals such as oxides and chalcogenides. The fundamental photon-matter interactions processes consist of transmission, reflection, refraction and absorption. However, a small fraction of the photons undergoes different interactions, resulting in the radiation of electromagnetic energy[97]. The radiation process is associated with the vibrations at the atomic scale. The vibration frequency of the scattered light can be recorded with a spectrometer by following frequency shifts in comparison with the original frequency of the excitation light. In the spectra the intensity, frequency and the band shape of the Raman bands provide information on the physical and chemical properties of the material.

We used Raman spectroscopy to investigate:

(i) the crystallinity of the CZTS layers by analyzing the most intense Raman mode and the lineshape width, i.e. the FWHM;

(ii) the secondary phases at the surface of the CZTS layers with up to ~300 nm penetration depth with different excitation wavelengths;

(iii) Ordered- type and disordered-type kesterite.

In kesterite studies using Raman spectroscopy, the most common excitation wavelength is 514 nm, which best determines the vibrational modes while estimating the degree of crystallinity of the CZTS layers. However, the analysis of multi-wavelength Raman excitation is necessary to identify the presence of potential secondary phases with different band gap and crystal structures. **Figure 2.3** shows a set of multiwavelength Raman spectra for CZTS material. The theoretical Raman vibrational modes of CZTS are at 253, 264, 274,287, 303, 316, 331,338, 347, 353, 366 and 373 cm^{-1} [98–101]. These Raman modes are related with the A, B and E modes. The A modes are related with anion vibrations; on the other hand, the B and E modes are related to anion and cation vibrations. In the B modes cations are displaced along the *c* direction, while E modes comprise cation vibrations parallel to the *a* direction. As we can see in **Figure 2.3** the intensity of the Raman modes change with the excitation wavelength. These differences in the spectra enable us to distinguish the overlapping peaks of secondary phases from the peaks of the primary CZTS phase (**Table 2.1**). For example, the main Raman modes of ZnS, 275 cm^{-1} and 352 cm^{-1}, are in the characteristic Raman spectra region, 250 cm^{-1} and 380 cm^{-1} of CZTS phases

(**Figure 2.3**). If the ZnS phase coexists in small quantities, identification of ZnS is usually inaccurate. A comparison of CZTS and ZnS phases around 700 cm^{-1} in the inset of **Figure 2.3** shows two distinguishable peaks for the corresponding phases.

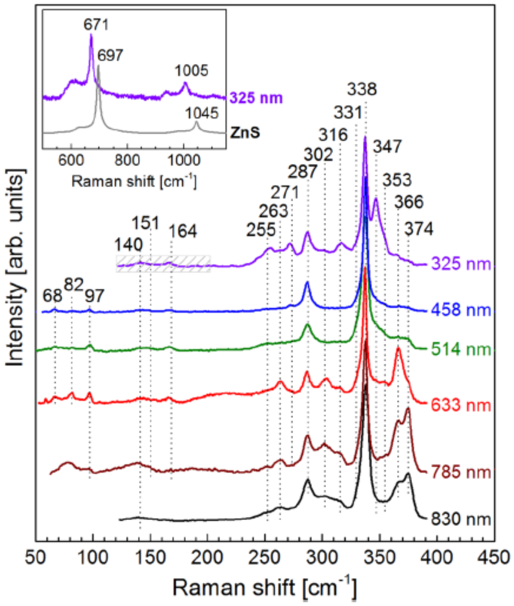

Figure 2.3 Raman spectra of polycrystalline CZTS thin film measured with different excitation wavelengths; the inset shows the spectra measured with 325 nm excitation wavelength for CZTS and ZnS phases taken from Ref [101]

In our experiments, the measured spectra are analyzed by using Lorentzian lineshapes with Magic Plot Student 2.3 to fit the experimental peaks and to calculate the full width and half maximum (FWHM) of selected peaks. The 514 nm wavelength was used for the identification of CZTS, CTS and CuxSy phases; for the identification of ZnS instead we used 405 nm.

Table 2.1 The main Raman peaks of Cu-Zn-Sn-S system [98]

Phase Name	**Raman Peak (cm^{-1})**
CZTS	**289, 339**
ZnS	**275, 352**
Tetragonal CTS	**297, 337, 352**
Cubic CTS	**267, 303, 356**
Orthorhombic CTS	**318**
Orthorhombic SnS	**160, 190, 219**
Hexagonal SnS_2	**314**
Hexagonal $Cu_{2-x}S$	**475**

The semi-quantitative characterization of the amount of disordered and ordered type kesterite in the CZTS material can be achieved by analyzing some of the peaks in the Raman spectra with 514 nm and 785 nm excitation wavelength[28, 99, 102–104]. The chemical disorder in kesterite originates from the Cu and Zn atoms at the planes at z¼ and ¾ due to the facile atomic exchange between these planes, while the other sublattices are both undisturbed [102, 103]. **Figure 2.4** shows the relevant lattice sites and planes in the kesterite structure and illustrates the ordered type kesterite (left) and disordered type kesterite (right) cases.

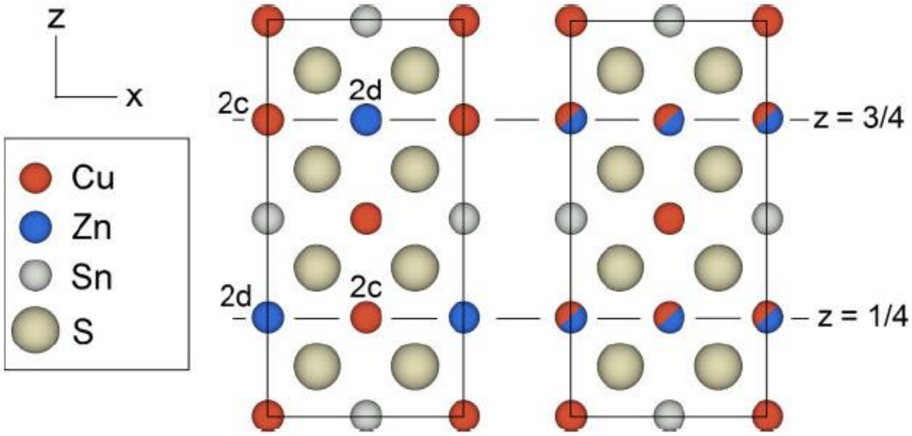

Figure 2.4 Projection of the conventional kesterite unit cells along the y-axis of CZTS material for ordered type kesterite (in the middle) and the disordered type kesterite (at the left) with random Cu and Zn distribution in the 1/4 and 3/4 at z- axis. Taken from Ref [105].

In the literature, the structural inhomogeneity of a CZTS material is determined by investigating the relative intensity of the Raman modes which has been related to the ordered-type and disordered –type kesterite[103, 104, 106]**.** In this dissertation, we also used the same methods for the analyses of CZTS material**.** Three parameters; Q, Q', Q" are defined in **(Table 2.2)** and quantify the chemical disorder; a fourth parameter is the FWHM of the main Raman line of CZTS, which estimates the extent of material crystallinity. The investigation of Cu-Zn disorder with 785 nm excitation wavelength is based on the intensity ratio of the peak around 288 cm^{-1} with respect to the peak at 306 cm^{-1} (**Equation 2.14**) and on the intensity ratio of the peak at 338 cm^{-1} with respect to the sum of the peaks at 366 cm^{-1} and 375 cm^{-1}(**Equation 2.15**) [102, 103, 105]. The Raman mode at 288 cm^{-1} is related to the ordered type kesterite, and the mode at 306 cm^{-1} is assigned to the disordered type kesterite. CZTS materials with higher chemical disorder have low Q values. The Q' value is calculated from the Raman modes at 338 cm^{-1}, 366 cm^{-1} and 375 cm^{-1}. If the disorder of the material increases the intensity of the modes at 366 cm^{-1} and 375 cm^{-1} increase also, and the Q' value decreases. It has been reported that slower cooling rates and post annealing around 200 °C increase the order of the Cu-Zn atoms in the lattice, hence Q and Q’ increase[102, 103, 105].

Table 2.2 Analyses table for Raman spectra of CZTS materials

Name	Description	Equation	Literature	Wavelength (nm)	Reference
Q	$I_{(288)}/I_{(306)}$	(2.14)	0.6-1.2(quenched) 2.4-8.2 (slow cooling)	785	[28, 102, 103]
Q’	$I_{(338)}/I_{(366)+(375)}$	(2.15)	0.9-1.0 (quenched) 2.0-3.6 (slow cooling)	785	[28, 102, 103]
Q’’	$I_{(338)}/I_{(331)}$	(2.16)	4.78-16.6	514	[104]
FWHM (cm^{-1})	FWHM of Raman mode at 338 cm^{-1}		7.8-12.2	514	[104]

We can also use the 514 nm excitation wavelength to investigate the ordered and disordered kesterite by using peaks at 331 cm^{-1} (related with disordered type kesterite) and at 338 cm^{-1} (related with ordered type kesterite). For this purpose we used **Equation 2.16** and named this parameter as Q’’. The Q’’ and FWHM parameters in **Table 2.2** are extracted from a study by Caballero et al. [104], where they reported the dependence of disorder on thermal treatment and composition. In the literature, the identification of chemical disorder with 514 nm excitation wavelength is less common in comparison with the 785 nm excitation wavelength [104]. For the sake of more precise identification of chemical disorder of a complicated material like CZTS, we will report values of Q, Q’ and Q’’ as shown in **Table 2.2**, which we believe will give a better understanding on the crystallographic properties of CZTS grown under different conditions.

2.3 Photoelectrochemical and Electrical Characterization

A. Photoelectrochemical Characterization of CZTS Layers

Photoelectrochemical (PEC) characterization is a practical way to quantify the photoactivity and determine the majority carrier type for a semiconductor in a suitable electrolyte[107, 108]. The essential steps for the PEC characterization of a p-type semiconductor and a redox electrolyte, Eu^{3+} /Eu^{2+}, is shown in **Figure 2.5**. In the beginning before immersion, the Fermi level of the semiconductor and the redox species in the electrolyte are decoupled (**Figure 2.5.a**). After contact, the valence and conduction bands of the p-type semiconductor bend and the Fermi level is equilibrated (**Figure 2.5.b**). A space charge region forms when the p-type material is in contact with a redox system with a different Fermi energy. If a light source shines on the solution, the semiconductor absorbs photons with energy larger than its band gap $(h\nu > E_{gap})$ and electrons are excited from the valence band to the conduction band (**Figure 2.5.c**). The electrons reduce the electrolyte species at the interface, generating a photocurrent. If an external potential is applied to the system the space charge region becomes wider and more charges reduce the electrolyte species leading to increasing photocurrent.

In our experiments we used a custom made cell for photoelectrochemical characterization of CZTS layers. A BioLogic SP-150 potentiostat was used to control PEC measurements and simulated sunlight source was provided by an Oriel Sol 1A solar simulator calibrated to output Air Mass 1.5 (standard simulated sunlight). A three electrode set up was used; a Hg/Hg_2SO_4 (MSE) reference electrode (E_{MSE} = 0.650 V_{SHE}) and a Pt gauze counter electrode were also immersed in the solution. The potential was scanned within the desired window with a scan rate of 10mV/s and the light was turned on and off at ~3s intervals by manually opening and closing the light source's shutter.

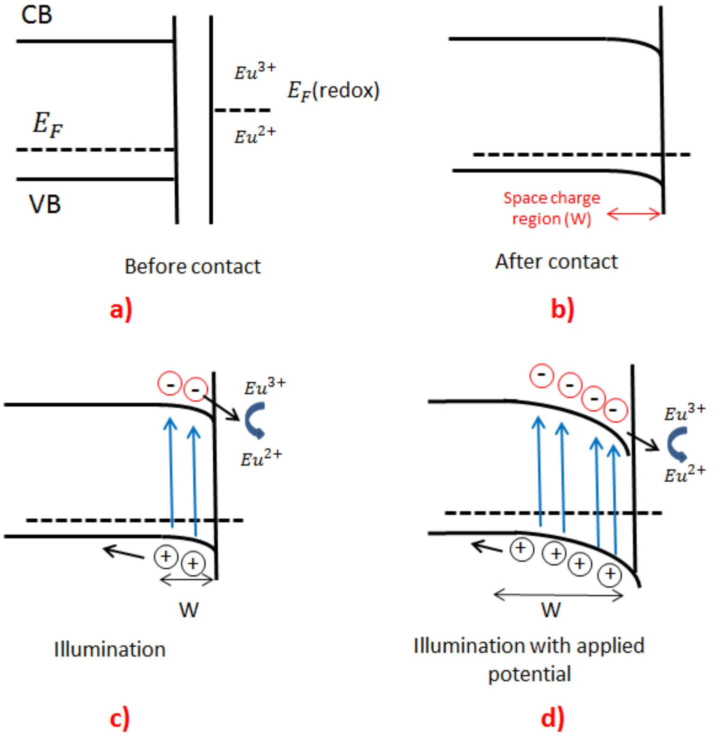

Figure 2.5 Semiconductor and europium electrolyte interface a) before contact, b) after contact, c) with illumination and with illumination and applied potential

The electrolyte in the PEC experiments should be conductive and contain redox species capable of collecting quickly photogenerated minority carriers to avoid photocorrosion. Europium nitrate with its suitable electronic position has been reported as a suitable redox mediator for CZTS layers, but it has a relatively slow electron transfer kinetics[109]. In our studies, we used 0.5M $Eu(NO_3)_3$ solution and scanned the potential starting from 0.05 V more positive potential than open circuit voltage and stopped at -1.0 V (MSE), before the reduction of Eu^{+3} to Eu^{+2} (~ -1.03 V vs. MSE)[110]. The photoresponse of the layers was found by calculating the difference between the current density under illumination (J_{light}) and the dark current (J_{dark}) at the potential of -0.90 V (vs. MSE).

In the photoelectrochemical experiments it is possible to observe a nonzero current even under dark conditions. This current is called dark current (J_{dark}) and is not the result of photogenerated carriers, but rather due to shunt contact, for example between solution and substrate or also to the presence of more conductive phases on the surface. Therefore, PEC experiments are also a practical means to investigate the density of pinholes in the films.

It is important to note that the PEC technique is sensitive only to the surface characteristics of the material under study, and would not provide any information on the bulk region of the material.

B. Mott-Schottky Technique

The Mott−Schottky technique is used to determine the doping level of CZTS films by measuring its flat band potential in a suitable electrolyte. Once the semiconductor is immersed into an electrolyte with a reversible redox couple, a charge depletion at the semiconductor surface occurs causing band bending. By varying the applied potential, the charge at the interface is changed, achieving eventually the flat band potential V_{FB}, i.e. the potential at which the Fermi energy of the electrons is equal ot the redox potential of the electrolyte. Knowing V_{FB} it is possible to determine also the band edges of the semiconductor. **Equation 2.17** relates the interface capacitance vs applied potential to the doping concentration and the flat-band potential under depletion conditions[111, 112]. In the capacitive region, the capacitance C can be estimated from Im(Z), the imaginary component of the measured impedance, and f (frequency) relation.

$$\frac{1}{C^2} = \frac{2}{q\varepsilon\varepsilon_o N_D}\left(E - E_{FB} + \frac{kT}{q}\right) \tag{2.17}$$

$$\mathrm{lm}(Z) = \frac{1}{2\pi f C} \tag{2.18}$$

N_D =the doping density (1/cm^3)

q=electron charge (1.60219X10^{-19} C)

ε_o=permittivity of free space (8.85X10^{-14} F/cm)

ε=dielectric constant of the material

E=applied potential (V)

E_{FB}= flat band potential (V)

The Mott-Schottky studies were performed in a 0.5M Na_2SO_4 solution (pH =~ 7) in a three-electrode configuration with an MSE reference electrode and a Pt gauze counter electrode with fixed frequency of 1 kHz in the potential range between 0.3 and -1.3 V_{MSE}, within the capacitive potential region.

C. Hall Measurements

Carrier density and flat band potentials of the CZTS layers in the solid state were measured using an Ecopia HMS-3000 Hall measurement system in a Van der Pauw four point configuration under a magnetic induction field of 0.55 T. The Hall measurements have been performed in Mool C. Gupta Group in the Department of Electrical and Computer Engineering at the University of Virginia.

2.4. Fabrication and Characterization of Solar Cells

A. Fabrication of Solar Cells

Electrodeposited CZTS films on Mo foil act as an absorber layer for solar cells with the following architecture: Al:Ni/ITO/ZnO/CdS/CZTS/Mo. Fabrication of a solar cells starts with CZT electrodeposition and sulfurization to form CZTS, followed by chemical bath deposition of the n-type semiconductor CdS onto the CZTS layer. The chemical bath deposition recipe is adopted from reported studies[113, 114] (**Table 2.3**) to obtain 50 nm thickness of the CdS layer.

Table 2.3 Chemical solution recipe for chemical bath deposition of CdS

Chemical Name	**Formula**	**Concentration**	**Amount (ml)**
Purified Water	H_2O	100 vol%	150
Cadmium Sulfate	$CdSO_4.8/3\ H_2O$	0.015 M	22
Ammonium Hydroxide	NH_4OH	28-30 vol%	28
Thiourea	CH_4N_2S	0.75 M	22

The surface of the kesterite films tends to form oxide layers in a short time: therefore, it is important to deposit the CdS layer right after the sulfurization process. The deposition steps of the CdS are as follows;

1) The temperature of the chemical bath is set to 65°C with a jacketed beaker.
2) Cadmium source is added to the 150 ml purified water
3) Ammonium hydroxide source is then added to the cadmium solution
4) CZTS layers are immersed into the solution for one minute
5) Thiourea is added to the Cadmium and ammonium hydroxide solution
6) CZTS layers soaked in the solution for 11 more minutes.
7) Layers are immersed in purified water/purged with Nitrogen gas
8) Lastly, layers are baked in air at 120 °C for minutes.

The p-n heterojunction thus formed shows an offset in the conduction and valence bands between the two materials, due also to the different band gaps. **Figure 2.6** shows an example for a typical band alignment for a p-type CZTS and an n-type CdS heterojunction solar cells[115], determined by the work function and the electron affinity of the two semiconductors. In this case, the conduction band offset enhances electron transport to the n-type side under the effective field.

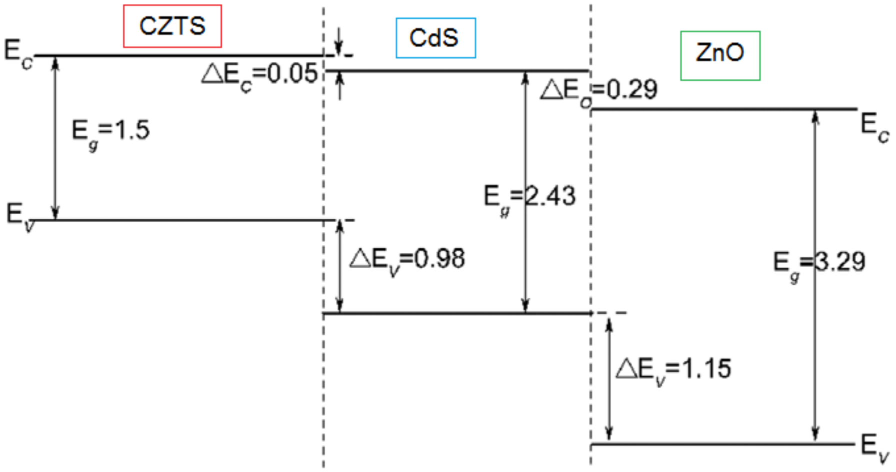

Figure 2.6 The band alignment of n-type CdS and a p-type CZTS. Taken from Ref [115]

The ZnO layer (80nm) and ITO layer (220nm) are grown by RF sputtering and the Ni-Al grids are formed by thermal e-beam evaporation. The ZnO window layer has a wide band gap and a suitable band offset for an efficient electron transport via the CdS layer[116]. The ITO layer on the other hand has a suitable barrier with the ZnO interface for the collection of carrier at the front part of the solar cell[117]. The fabrication of the solar cells and their characterization, including current density-voltage (J-V) curve measurements, time resolved photoluminescence TRPL, external quantum efficiency EQE and capacitance-voltage (C-V) measurements have been performed at the Agrawal Laboratories in Purdue University.

B. Current Density- Voltage Measurements

Electrical properties of CZTS solar cells were measured using an Oriel Sol3A solar simulator (Newport Corporation, Irvine, CA, USA) with temperature control stage, kept at 25°C. The solar cell tests were performed under AM 1.5 filtering, calibrated to 100 mW/cm^2 with a silicon reference cell.

The current-voltage curve of a solar cell is the superposition of the curve of a solar cell diode in the dark with the light-generated current. Current density-voltage measurements are the most basic solar cell characterization technique, helping to understand the loss mechanisms by analyzing four major cell parameters. These parameters are the open circuit voltage V_{oc}, the short circuit current density J_{sc} (J_{sc} is also described as I_{sc} in the following part), the fill factor FF and the power conversion efficiency PCE; this last parameter can be calculated from V_{oc}, J_{sc} and FF [118–122].

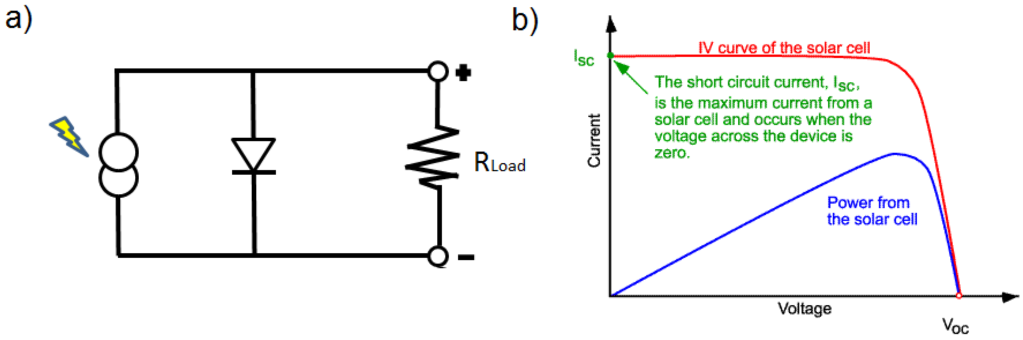

Figure 2.7a) Electrical model of an ideal solar cell circuit and b) close to ideal current –voltage curve (red) and power from the same solar cell(blue) Figure 2.7.b is taken from Ref [123]

Figure 2.7.a shows an equivalent circuit of an ideal solar cell, consisting of a current generator in parallel with a diode. The current flow depends on the illumination intensity and the load resistance. The open-circuit voltage, V_{OC}, is the maximum voltage available from a solar cell at zero current. The open-circuit voltage corresponds to the amount of forward bias in the cell owing to the bias of the solar cell junction due to the light-generated current. **Figure 2.7.b** shows the V_{oc} on the IV curve; the equation for V_{oc} can be found by setting the net current equal to zero in the solar cell.

$$V_{OC} = \frac{nkT}{q} \ln(\frac{I_L}{I_o} + 1) \tag{2.19}$$

The open-circuit voltage can also provide an estimate of the amount of recombination in the device; it depends on the saturation current (I_o) and the light-generated current $I(_L)$. Here, T is the temperature (K), k is Boltzmann constant, n is the ideality factor of the junction and q is the electron charge. The current I in the I-V curve can be expressed as below;

$$I = I_o \left[\exp\left(\frac{qV}{nkT}\right) - 1\right] - I_L \tag{2.20}$$

The second important parameter is the short circuit current J_{sc} which represents the current flowing through the solar cell when the voltage across the solar cell is zero. The short-circuit current is the largest current which may be drawn from the solar cell. The factors that affect the solar cell performance include extrinsic and intrinsic parameters, as follows;

1) Extrinsic parameters are the power of the incident light source and the spectrum of the incident light (AM 1.5 spectrum is the most common one for solar cell characterization).

2) Intrinsic parameters comprise the optical properties (absorption, reflection) and the charge carrier properties, such as mean free path, and collection efficiency. The collection probability depends mostly on the surface passivation and the minority carrier lifetime of the solar cell materials.

The efficiency of the solar cell strongly depends on the fill factor, FF, i.e. the ratio of the maximum power from the solar cell to the product of V_{oc} and I_{sc}. In the I-V curve, the FF is a measure of the squareness and is also the area of the largest rectangle which will fit in the curve. The FF can be defined as follows;

$$FF = \frac{V_{MP}I_{MP}}{V_{OC}I_{SC}} \tag{2.21}$$

Here, V_{mp} stands for the maximum voltage and I_{MP} is the maximum current corresponding to the load where power is maximum. The FF together with V_{oc} and J_sc can be used to find the maximum, power, P_{max} , of the I-V curve. The maximum power is equal to:

$$P_{max} = V_{OC}I_{SC}FF \tag{2.22}$$

and the efficiency of a solar cell is determined as the fraction of incident power which is converted to electricity and is defined as:

$$\eta = \frac{V_{OC}\, I_{SC} FF}{P_{in}} \tag{2.23}$$

In non-ideal conditions, solar cells present parasitic resistances, which change the current flow in the circuit. The additional element into the circuit also changes the Jsc and Voc and FF of the J-V curve. An example J-V curve for a non-ideal solar cell is shown in **Figure 2.8** and an equivalent circuit of a non-ideal solar cell is shown in the inset. In this circuit parasitic resistances are the series resistance R_S and shunt resistance $R_{SH.}$ The former introduces resistance to the flow of the current, which can be due to resistance contacts in and between the layers of the solar cells. The shunt resistance on the other hand, creates a leakage current in the cell, due to short resistance paths. A high efficiency solar cell needs to have low Rs and high R_{SH} to prevent low currents. The cell output current I with the series resistance and the shunt resistance is given in **Equation 2.24**. Here V is the voltage across the cell terminals.

$$I = I_L - I_o \exp[\frac{q(V+IR_s)}{nkT}] - \frac{V+IR_s}{R_{SH}} \tag{2.24}$$

The series resistance Rs (**Equation 2.25**) and shunt resistance Rsh (**Equation 2.26**) can be defined by the slopes of the I-V curves at I=0 and at V=0, respectively[124] .

$$r_s = -\left(\frac{dV}{dI}\right) \; at\, I = 0 \tag{2.25}$$

and

$$r_{sh} = -\left(\frac{dV}{dI}\right) \; at\, V = 0 \tag{2.26}$$

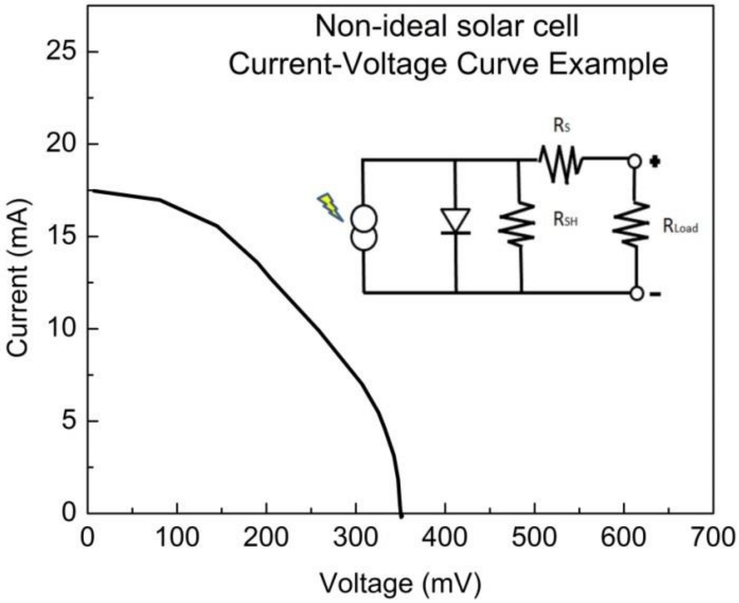

Figure 2.8 Example of a current-voltage curve of a non-ideal solar cell example and the equivalent circuit

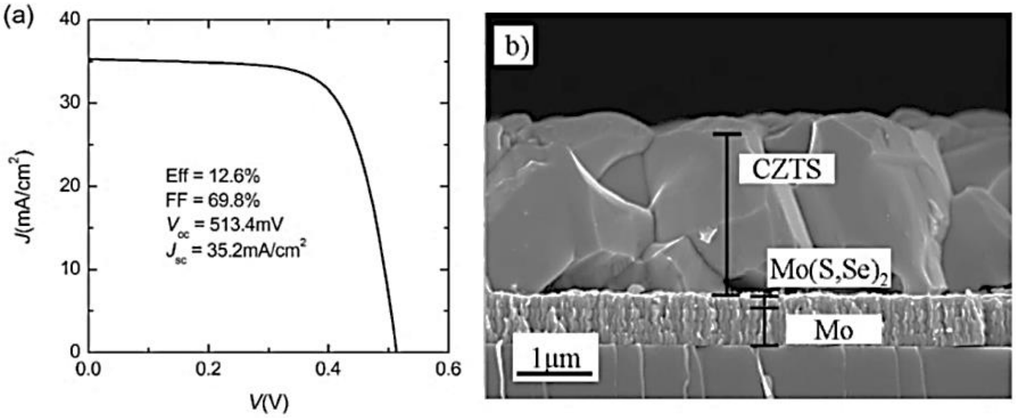

Figure 2.9 An example for a high efficiency CZTSSe a) current density-voltage curve and b) cross-sectional view SEM image [125]

An example of a J-V curve and the cross sectional image for a high efficiency solar cell, 12.6 %, for a CZTS absorber layer based cell with Cu-poor and Zn-rich CZTSSe material is shown in Figure 2.9. Even though the open circuit voltage and the short circuit current are improved with the CZTS film in **Figure 2.9.b** in comparison to other CZTS cells in the literature, possible interfacial recombination centers may be the reason for the Voc deficit.

C. External Quantum Efficiency (EQE)

The ratio of the number of charge carriers collected by the solar cell to the number of photons of a given energy shining on the solar cell from outside (incident photons) is called external quantum efficiency.

$$EQE = \frac{electron/sec}{photons/sec} = \frac{current/(charge\ of\ an\ electron)}{(total\ power\ of\ photons)/(energy\ of\ an\ electron)} \tag{2.27}$$

The EQE depends on two main parameters; absorption of light and the collection of charges. The absorbed photon generates an electron-hole pair. The charges (electron and hole) must be separated and collected at the junction without charge recombination for a high efficiency solar cell. Therefore, EQE is a fundamental parameter to understand the charge recombination in solar cells[118]. The band gap of the semiconductors can be found from the relationship between the incident photon energy (hv) and the optical absorption coefficient (α) by using the general Tauc equation [126].

$$\alpha hv = A(hv - E_g)^{1/2} \tag{2.28}$$

In the above equation A is a constant and Eg is the band gap of the semiconductor. The band gap can be calculated by plotting $hvln(1 - EQE)^2$ against hv. The linear portion of this plot extrapolated at the intersection with the x –axis gives the band gap Eg= hv of the material.

D. Time Resolved Photoluminescence (TRPL)

The charge carrier lifetime of a semiconductor is one of the key parameters that helps to rationalize the efficiency of a solar cell absorber; this parameter can be found with TRPL measurements. TRPL is measured by exciting photoluminescence using a diode laser source (640nm pulsed width of 100pm, 1Mhz) and later following the decay in photoluminescence with an InGaAs photomultiplier tube (Hamamatsu H10330-75). The TRPL experiments are performed at CdS/CZTS bilayers to avoid the degradation of the absorber layer in air. The TRPL decay in our study can be described using a bi-exponential decay model in the below equation:

$$I(t) = C_1 e^{-t/\tau_1} + C_2 e^{-t/\tau_2} \tag{2.29}$$

$$\tau_{Stat} = \frac{(C_1\tau_1 + C_2\tau_2)}{(C_1 + C_2)} \tag{2.30}$$

The time constants (τ_1 and τ_2) and the related pre-exponential coefficients (C_1 and C_2) are used for the statistical average of the lifetimes according to **Equation 2.30** to allow the quantitative analysis of carrier lifetimes.

E. Capacitance-Voltage Measurements

A Capacitance-Voltage (C-V) measurement provides some important device properties such as doping density and built-in potential[66, 127]. The C-V measurements are collected in the dark, with V_{rms}=20mV (rms=*root mean square)*, V_{dc} (dc=direct current) range of -1 V to +1 V, and at 10^5 Hz AC signal frequency at room temperature with LCR meter, HP model 4284a. The doping density can be found by plotting the $1/C^2$ vs. V.

$$\frac{1}{C^2} = \frac{2}{qN_a\varepsilon\varepsilon_o A^2}(V_{bi} - V) \tag{2.31}$$

Here, Na is the doping density ($1/cm^3$), q is electron charge ($1.60219*10^{-19}$ C) , $\varepsilon_o$is permittivity of free space ($8.85*10^{-14}$ F/cm), ε dielectric constant of the material, A is the area of the cell . C is the measured capacitance and V is the applied potential.

The doping density can be expressed as follows;

$$N_a = \frac{2}{\varepsilon\varepsilon_o A^2[\frac{d}{dV}\left(\frac{1}{C^2}\right)]} \tag{2.32}$$

Once we plot the $1/C^2$ vs applied potential we can obtain the doping density from the slope and the built-in potential from the intercept, similarly to the Mott-Schottky method.

Chapter 3-Optimization of Electrodepositon Conditions of Cu-Zn-Sn(CZT) Metallic Precursors: Electrodeposition from an Acidic Solution

I. Introduction

It is well understood that the composition of the CZTS material, particularly the Cu/(Zn+Sn) and Zn/Sn ratio have a critical influence on the performance of the solar cells[27, 128]. Less attention has been paid to the overall compositional distribution of the Cu-Zn-Sn (CZT) precursors for the growth of CZTS[44, 85]. In this study, we have varied the deposition potential in order to grow CZT metallic precursor layers with close to stoichiometric Cu fraction (50 at%) while varying the Zn/Sn ratio within the ideal composition range to synthesize suitable precursors for CZTS. In our effort to make targeted metallic precursors, first we investigated the deposition potential range necessary to deposit suitable CZT metallic precursors. Compositional analyses suggest that by varying the applied potential it is possible to control the Cu/(Zn+Sn) ratio and Zn/Sn ratio of the CZT layers in the range of 0.92-0.85 and 1.16 to 0.93, respectively. These layers were grown using a citrate based acidic solution. The crystal structure analyses of the CZT precursors were determined by XRD and the morphological features were assessed by SEM and EDS compositional mapping.

II. Cyclic Voltammetry of Cu-Zn-Sn Solution

Electrodeposition of Cu-Zn-Sn (CZT) alloy films was performed at room temperature in a three-electrode cell with vertical electrodes, the cathode and counter electrode facing each other. A Pt mesh was used as the counter electrode, and a saturated mercurous sulfate as the reference (MSE, $E^{o}_{MSE} = 0.650V_{SHE}$); in the following, all the potential will be referred to MSE. The experiments were performed using an EG&G-PAR potentiostat-galvanostat Model 263A. The CZT films were grown from an acidic solution (pH 2.3) combining 0.2 M $C_6H_8O_7$, 0.2 M Na_2SO_4 30 mM $SnSO_4$, 30 mM $ZnSO_4$ and 40 mM $CuSO_4$, using ultra-pure Milli-Q water (resistivity18.2 MΩ·cm) produced in house; pH was adjusted with diluted NaOH. The solution was filtered after the addition of $SnSO_4$ and before pH adjustment. The working electrode substrate was a Mo sheet with 0.1 mm thickness and 99.95% purity (Alfa Aesar).

The cyclic voltammetry (CV) for the Cu-Zn-Sn deposition solution is shown in **Figure 3.1.** The voltammograms were run at a scan rate of 10 mV/s. The calculated redox potential of copper, tin and zinc are -0.39, -0.87 and -1.5 V, respectively. In comparison, the Cu reduction peak occurs around -0.7 V and the reduction of Sn starts at a potential of ~ -1.0 V, showing significant overvoltages. The reduction of Zn cannot be identified via CV since it occurs at potentials more negative than the hydrogen evolution reaction (HER).

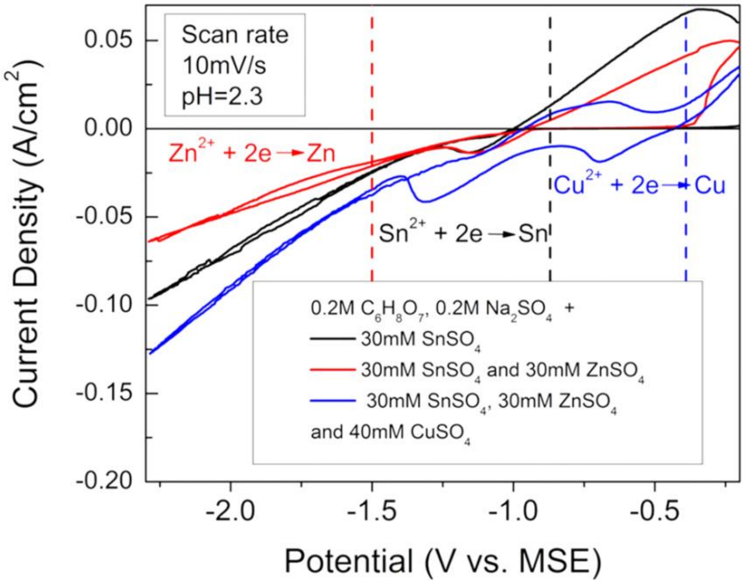

Figure 3.1 Cyclic voltammetry of Cu-Zn-Sn precursors with 10 mV/s scan rate

A cyclic voltammetry for the supporting electrolyte and zinc metal ion containing electrolyte are shown in **Figure 3.2**. The current increase for the supporting electrolyte only (black curve) starts at more negative potentials than -1.0 V and the current density data becomes more noisy at more negative potentials than -1.5 V due to the increasing HER. Zinc-containing electrolyte (red curve) displays a similar current increase to the black curve at the cathodic scan. In contrast, the anodic scan is different, an oxidation peak is seen, which is attributed to the zinc dissolution, is observed.

The current increase in the anodic region starts at -1.4 V, reaches its maximum at -1.1 V and current density becomes zero at around -0.94 V.

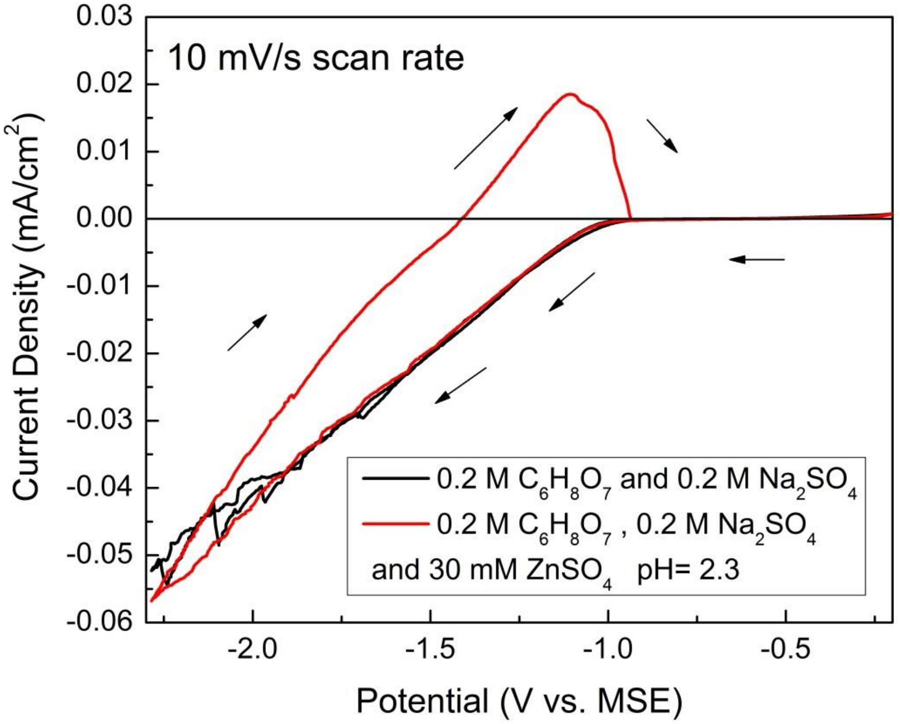

Figure 3.2 Cyclic voltammetry of supporting electrolyte and Zn containing electrolyte with 10 mV/s scan rate

III. Electrodeposition and Compositional Analyses of CZT Metallic Precursor

The alloy compositional trend is shown as a function of potential in **Figure 3.3**. The fraction of Cu and Sn in the alloy decreases with higher overvoltages. Zn was detected by EDS only at potentials more negative than -1.7 V, and its fraction increased at more negative potentials. The standard deviation (obtained over 3 data sets) was less than 2.7 at % for all elements and is not visible in the graph for less than 1 at%. Slightly larger compositional deviations were measured at deposition potentials more negative than -1.8 V.

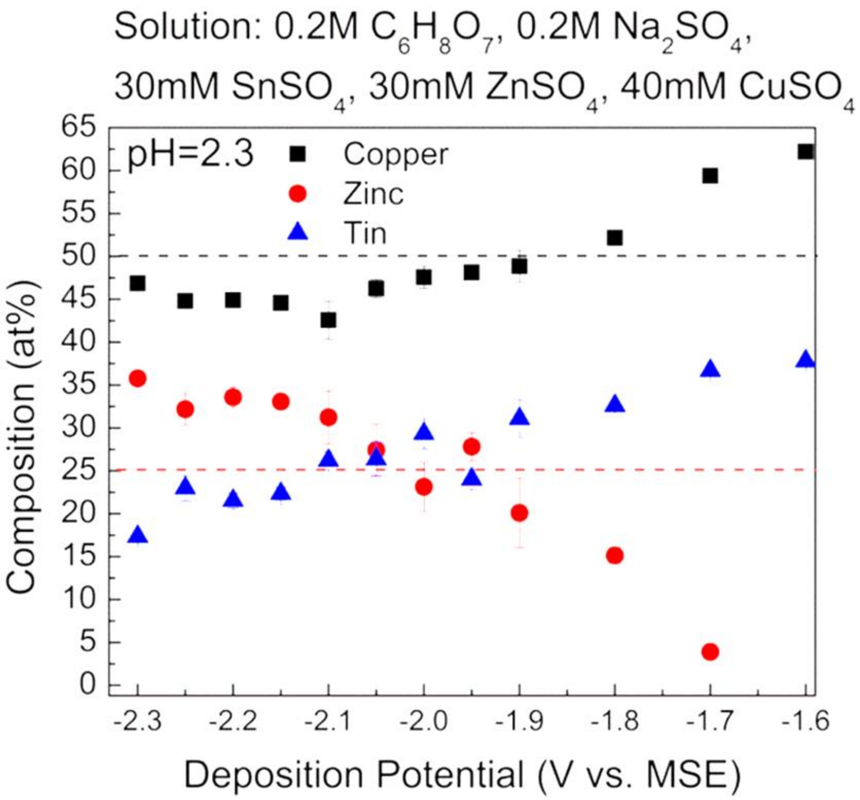

Figure 3.3 Composition vs. potential curves of Cu-Zn-Sn precursors

After investigating the compositional trend of the ternary deposition system, we focused on achieving the targeted compositional ratios for CZT precursors, Cu/(Zn+Sn) and Zn/Sn. As we described in Chapter 1, the stoichiometric ratio for the formation of CZTS films is Cu: Zn: Sn = 2:1:1, i.e. Cu/(Zn+Sn) =1 and Zn/Sn =1. However, record efficiencies for CZTS absorbers are consistently reported for Cu-poor and Zn-rich layers[21, 24]. Therefore our studies focused on manufacturing Cu-poor metallic layers with varying Zn/Sn ratios.

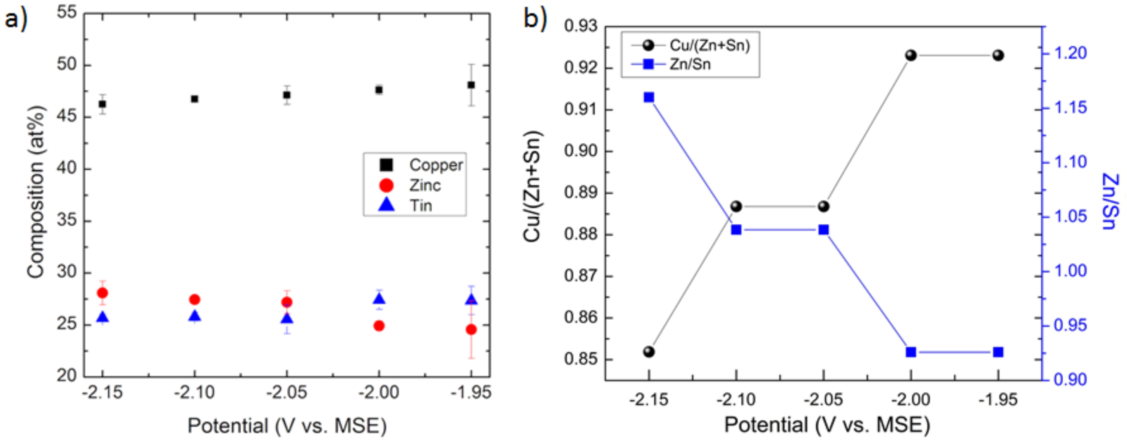

Figure 3.4 Cu-Zn-Sn precursor a) composition and b) compositional ratios vs. deposition potential

Figure 3.4.a shows the composition of CZT precursors in the narrow potential range that is suitable for CZTS formation; note that the Cu fraction is similar for films with different Zn/Sn ratio. The Cu/(Zn+Sn) ratio decreased and the Zn/Sn ratio increased with more negative potentials (**Figure 3.4.b**). The electrodeposition set up for the growth of Cu-Zn-Sn metallic precursors is vertical. Even though electrodeposition of three elements provided relatively uniform elemental distribution through the thickness of the layer, the lateral distribution of elements may generate inhomogeneity. To investigate the lateral distribution of elements over the whole substrate, we measured the composition at 9 points over a 0.5 cm^2 size Cu-Zn-Sn sample(**Figure 3.5**). Since this is a vertical deposition set up, we name the regions for composition analyses as top (y=0.2 cm), middle (y=0.5 cm) and bottom (y= 0.8 cm) region. The amount of tin in the film did change slightly as a function of position. However, the composition of zinc and copper changed ~4 at% over the film. The standard deviation of the CZT precursors with targeted off-stoichiometric value is 1.7 for copper and zinc and 0.2 for tin.

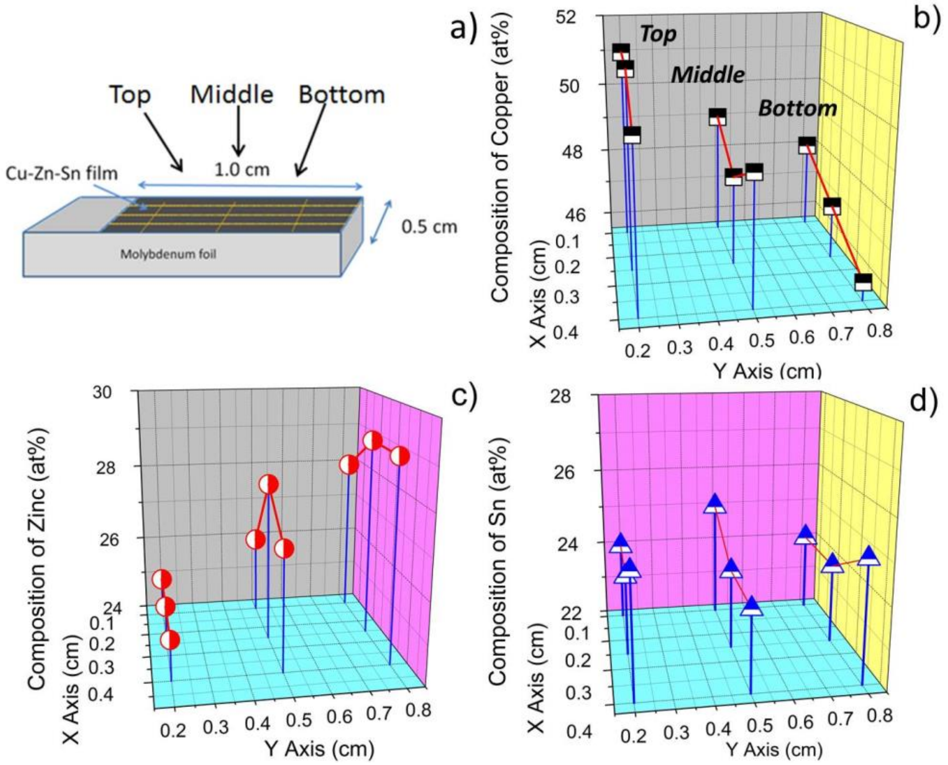

Figure 3.5 a) Schematic description of samples used for lateral EDS analysis and the elemental distribution for b) copper, c) zinc and d) tin, film deposited at -2.05 V

IV. Structural Characterization of CZT Metallic Precursors

X-ray diffraction patterns of the CZT metallic precursors with different composition ratio are shown in **Figure 3.7**. Intermetallic compounds, Cu_6Sn_5 and Cu_5Zn_8, were detected, together with a small amount of elemental Sn. The XRD peaks for metallic Cu and Zn superpose with the intermetallic compounds reflections (2θ~ 42-44°), making it difficult to detect and distinguish the relative amount of the various phases.

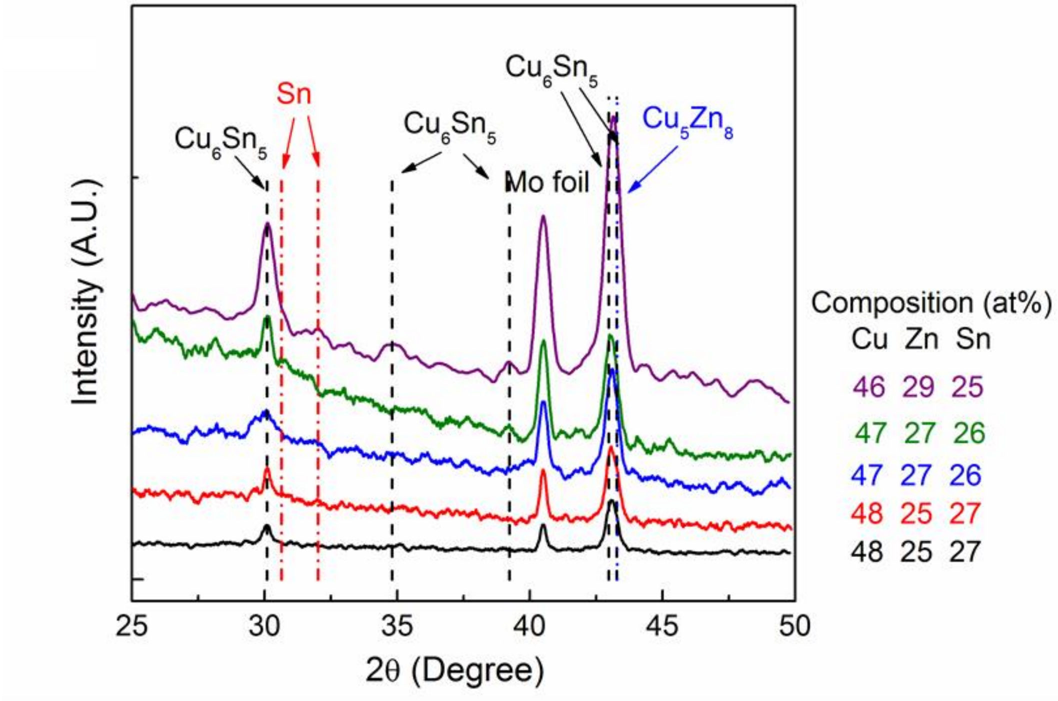

Figure 3.6 X-ray diffraction patterns of CZT metallic precursors

To investigate the relative fraction of intermetallic compounds with different composition we compare the XRD patterns of Cu-Zn-Sn precursor layers electrodeposited at -1.95V and -2.15 V (**Figure 3.7**). The intermetallic compounds Cu_6Sn_5 and Cu_5Zn_8 are observed in both layers. The main reflection for the Cu-Zn-Sn layer electrodeposited at -2.15V is slightly shifted with respect to that deposited at -1.95V. The Cu-Zn-Sn layer, electrodeposited at -2.15 V is at a slightly more positive angle comparing to Cu-Zn-Sn layer, electrodeposited at -1.95 V. The Sn fraction of the layers is only slightly different for Sn-rich and Zn-rich Cu-Zn-Sn precursor layer.

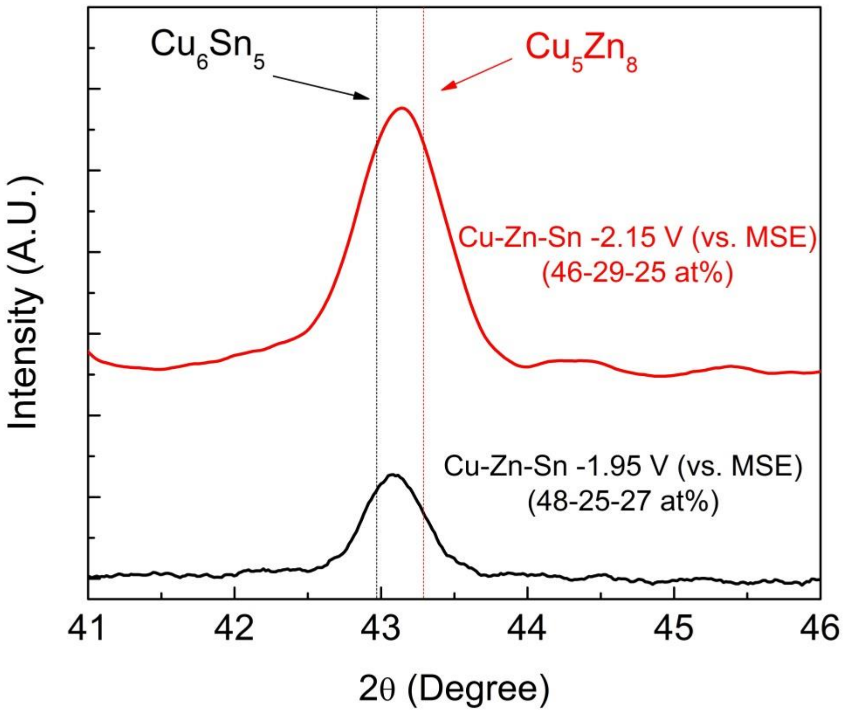

Figure 3.7 X-ray diffraction patterns of Cu-Zn-Sn precursor layers electrodeposited at -1.95V and -2.15 V (vs. MSE)

The isothermal section of the Cu-Sn-Zn phase equilibria at 230°C is shown in **Figure 3.8**[129]. According to this ternary phase diagram no ternary compound is stable[129]. The intermetallic compounds from Cu-Sn and Cu-Zn system is reported. Room temperature experiments with different CZT synthesis methods also strongly suggest the formation of the intermetallic compounds[85, 130–132]. The formation of Cu_6Sn_5 intermetallic compound during electrodeposition at room temperature has also been reported by others [85, 133]. Moreover, this intermetallic compound is known to be stable without decomposing at room temperature[130]. Intermetallic compound Cu_5Zn_8 was also reported earlier for the single bath electrodeposition of Cu-Zn-Sn together with the Cu_6Sn_5 phase [131]. However, this intermetallic compound has not been reported for the sequentially deposited Cu/Zn/Sn metallic layers while it is stable in the Cu-Zn- phase diagram[132]. The presence of intermetallic compounds in the metal alloy deposition method suggests that the electrochemical overpotential during electrodeposition from single bath solution is sufficient to form non-equilibrium phases such as Cu_5Zn_8 intermetallic compounds at room temperature.

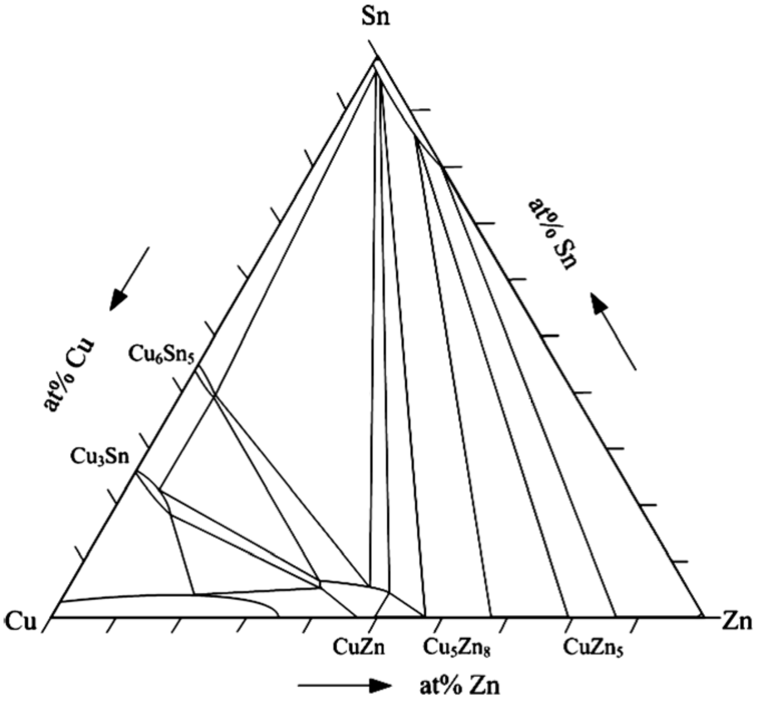

Figure 3.8 Isothermal section of the Cu-Sn-Zn ternary system at 230 °C, taken from Ref [129]

We performed a set of structural investigations as function of aging time to investigate the formation of the intermetallic compounds. The time dependent X-ray diffraction patterns of Cu-Zn-Sn precursor electrodeposited at -2.05 V (vs. MSE) are shown in **Figure 3.9**. The first pattern is measured right after electrochemical deposition and the last pattern is observed 7 days after electrodeposition. Intermetallic compounds Cu_6Sn_5 and Cu_5Zn_8 are observed in all of the patterns. Peak shift are not observed during 7 days, which suggests the stability of these intermetallic compounds at room temperature in atmospheric conditions. Room temperature formation of intermetallic compounds has been demonstrated by electrochemical deposition [134], and is explained in terms of accelerated atom mobility during growth due in part to the presence of internal stresses.

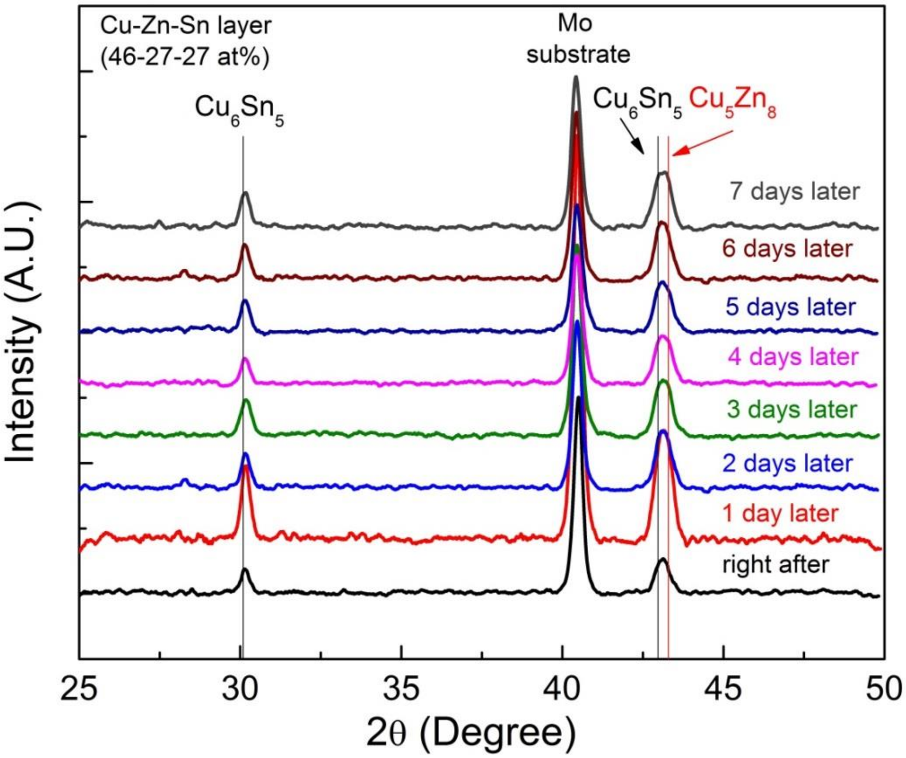

Figure 3.9 X-ray diffraction patterns of Cu-Zn-Sn precursor layer electrodeposited at -2.05 V (vs. MSE) during 7 days

V. Morphology of Electrodeposited CZT Layers

The top down image and cross sectional SEM images for the Cu-Zn-Sn precursor electrodeposited at -2.05 V are shown in **Figure 3.10**. The film (700 nm thick) is continuous at the substrate side, however it is less dense at its surface due to the dendritic growth after the first ~200 nm of the deposit.

The EDS compositional mapping of the CZT precursors is shown in Figure 3.11. A uniform signal distribution for each element is observed at this magnification. However we must note that the resolution of such compositional maps is limited at high magnification, due to the spread of the electron probe below the surface. Despite the use of software to calculate the penetration depth, it is difficult to use the recommended acceleration voltage as this value may not provide an optimal determination of the composition.

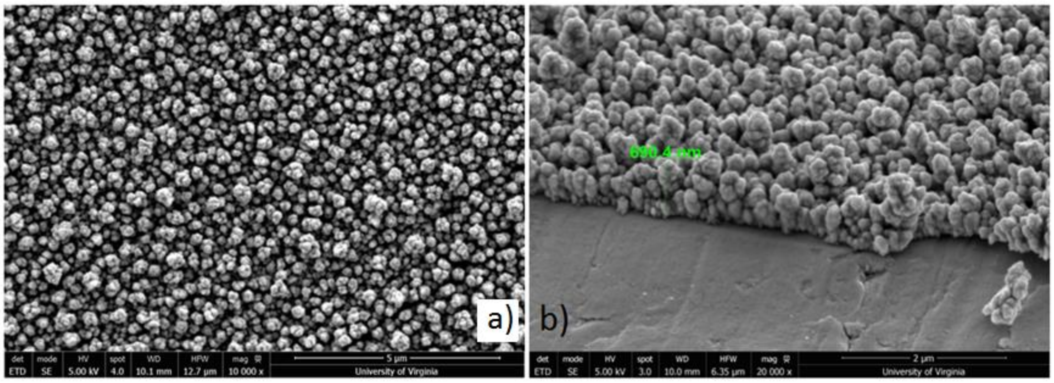

Figure 3.10 a) Top-down SEM image and b) oblique view showing the cross section, of Cu-Zn-Sn precursors electrodeposited at -2.05V

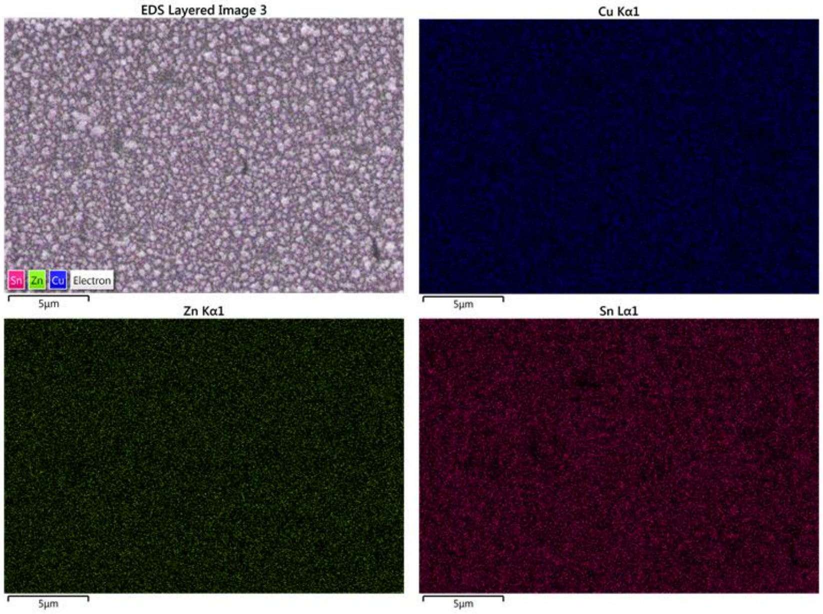

Figure 3.11 EDS mapping for a top down image of a CZT metallic precursor deposited at -2.05 V, color code; blue: copper, green: zinc and pink: tin.

Conclusion

Electrodeposition of CZT metallic precursors with the targeted off-stoichiometric ratio has been achieved by using a simple citrate based solution. The standard deviation of the elements is around 1.7 for copper and zinc and only 0.2 for tin in a 0.5 cm^2 area. The formation of intermetallic compounds takes place during the deposition and time dependent structural studies suggest the stability of the intermetallic compounds within 7 days time. The metallic precursors have a good coverage over the substrate, but only for thin films; however the deposit over time becomes slightly rough and powdery due to a tendency for dendrite formation. In the following chapter, Chapter 4, the sulfurization and characterization of CZT metallic precursors will be presented. In Chapter 8, the solar cell performance of the CZTS layers formed via sulfurization of CZT precursors deposited from citrate based solution will be discussed.

Chapter 4-Influence of Composition and Sulfurization Temperature on the Phase Purity and PEC Performance on CZTS Layers

I. Introduction

In this chapter, we investigate the influence of sulfurization parameters and composition of the initial metallic precursors on the phase purity of CZTS materials. Firstly, we study the influence of Zn/Sn ratio on the phase purity and crystal quality of CZTS films. Secondly, we compare the crystal quality of CZTS layers with similar composition, after sulfurization at 500 and 550 °C. We found that the phase purity and crystallinity are enhanced with increasing Zn/Sn ratio. The photoelectrochemical (pec) response of the CZTS layers increased with the increasing Zn/Sn ratio of the CZTS film. The best pec response was 0.99 mA/cm^2 for CZTS layer with Zn/Sn=0.98 after sulfurization at 550 °C; this pec response was twice more than the highest pec response we observed for the CZTS layer after sulfurization at 500 °C.Raman spectroscopy and X-ray diffraction studies strongly suggest that the enhanced response is correlated to decrease of the fraction of disordered type kesterite in the CZTS material.

II. Influence of Initial Composition on the Phase Purity of CZTS

Despite the large amount of work available on the compositional control of ternary alloys for CZTS layers, an assessment of the compositional deviation from stoichiometry due to the loss of elements and to the formation of secondary phases in CZTS layers for electrodeposited alloys is still missing. In this section, we investigate the influence of the initial precursor composition on the final CZTS material. For this task, we used metallic precursors electrodeposited from a citrate based solution, as discussed in Chapter 3. The sulfurization took place for one hour in Ar atmosphere with 25 mg sulfur for each CZT metallic layer. We decided to use 25 mg of sulfur according to our experiments on the influence of sulfur amount on the phase purity and the pec performance of the CZTS layers. The details of this study are presented in Appendix 1.

The composition of CZTS layers after sulfurization as a function of applied potential is shown in **Figure 4.1**. The fraction of sulfur in the films is ~ 55 at %; note also that the initial Zn/Sn ratio changes after sulfurization (**Figure 4.2.a**). The fraction of copper in the layers is around 20 at%, whereas Zn and Sn ratio varied. Specifically, after sulfurization Sn loss was observed for most of the samples, and Zn loss in one instance only. The relative loss of Sn increases for more negative deposition potentials (**Figure 4.2.b**). Interestingly, we observed different elemental losses for metallic precursors characterized by the same Zn/Sn ratios, 0.93 or 1.04, which suggests the occurrence of a microstructure and phase constitution of the alloy dependent on applied potential.

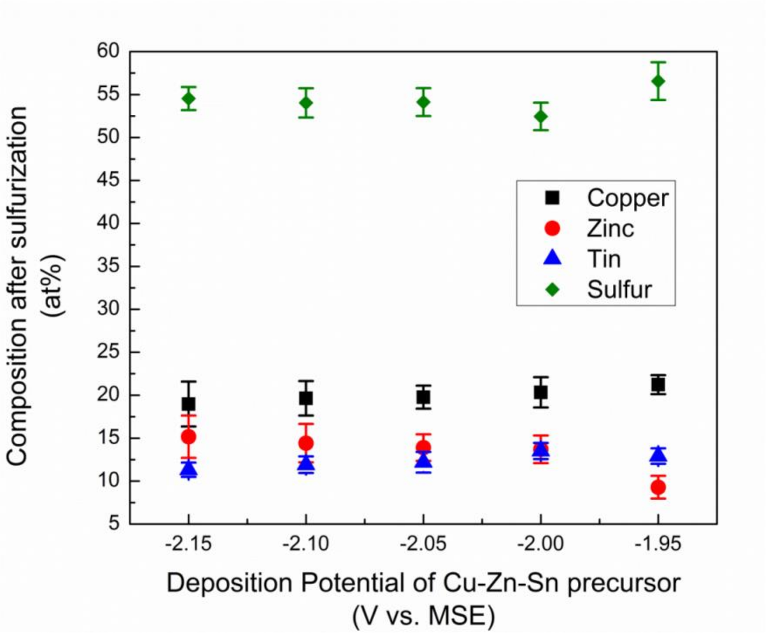

Figure 4.1 Composition of the layers after sulfurization

In the literature, compositional changes upon sulfurization are attributed to the loss of secondary phases [46, 48, 65]. Initially binary sulfides (Cu_xS_y, ZnS and SnS_2) are formed below 300°C and later, above 350°C, these compounds react to form Cu-Sn-S phases. Finally, the CZTS phase is formed by the reaction of Cu_2SnS_3 with ZnS. During the formation of binary sulfides, solid tin monosulfide is forming by the desorption of sulfur-rich tin sulfides. The evaporation of $SnS_{(s)}$ takes place between 350-450 °C [46, 48, 79], leading to a decrease in Sn concentration [46, 79].

The loss of Zn from CZTS layers has also been reported before and is attributed to the evaporation of elemental Zn before the formation of ZnS [135, 136].

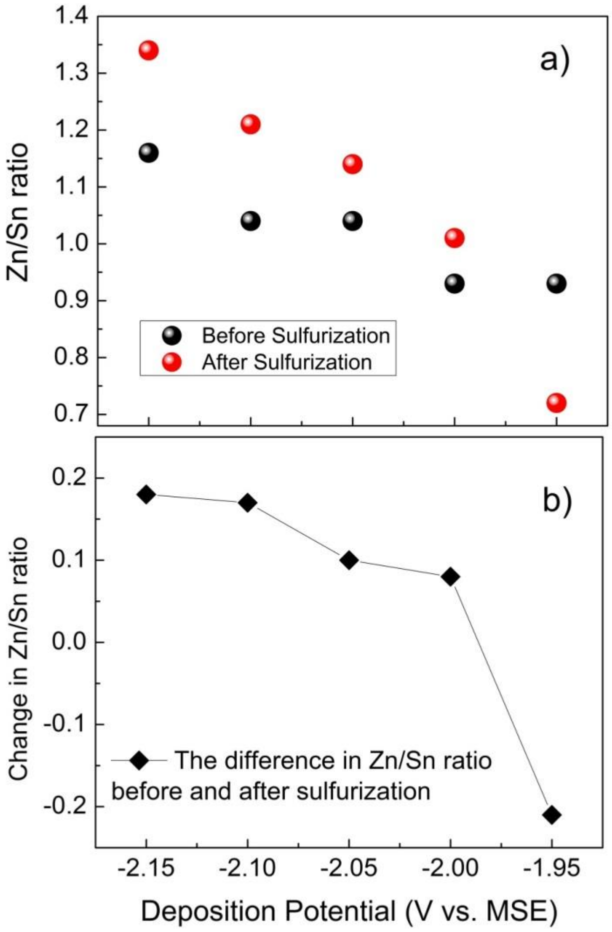

Figure 4.2 a) Zn/Sn ratio and b) change in Zn/Sn ratio as a function of the deposition potential used to grow the precursor, before and after sulfurization at 500 °C.

Figure 4.3 shows the compositional distribution of the four elements at nine different positions on the CZTS layer after sulfurization of CZT metallic precursors (deposited at -2.05 V). The fraction of the elements in the layers is Cu; 19.7 ±0.6, Zn: 11.0 ±0.5, Sn: 11.3±0.3 and S: 57.9±1.1. The standard deviation of the elements decreased more than twice for copper and zinc (precursors value Cu:48.8±1.7 and Zn: 26.9±1.7) and slightly increased for tin (precursor value Sn:24.3±0.3)

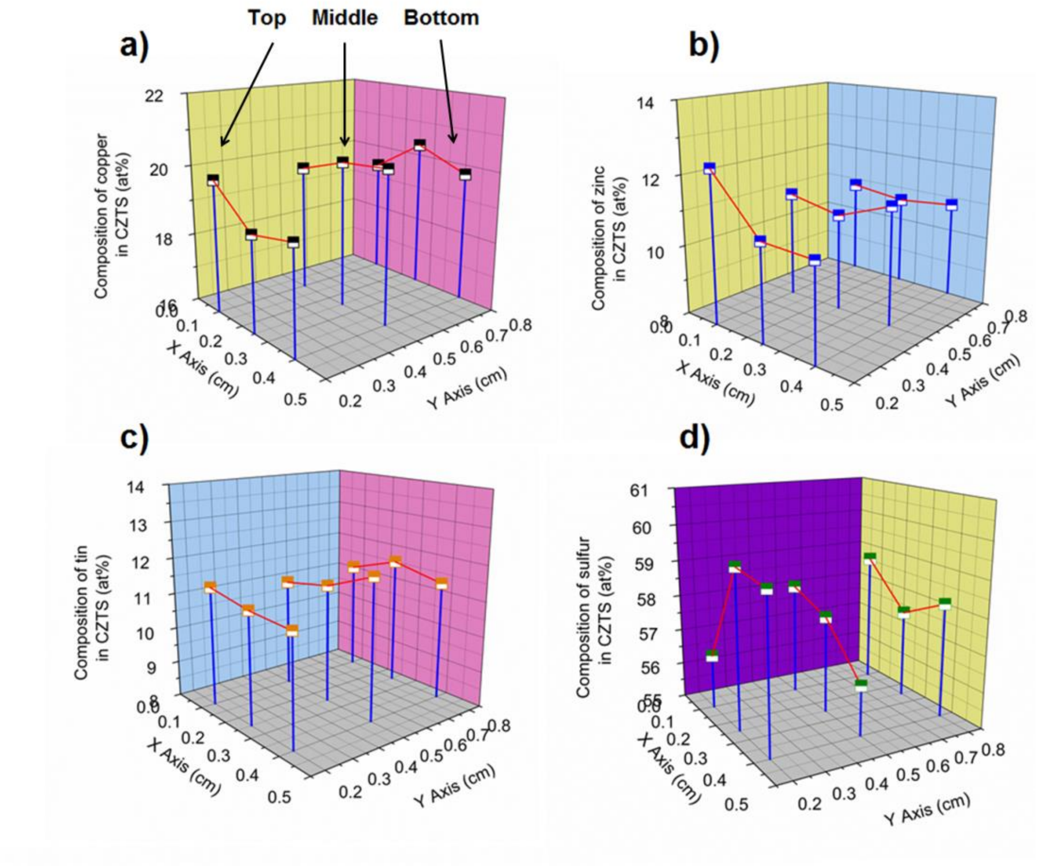

Figure 4.3 Composition of CZTS layers after sulfurization for a) copper, b) zinc, c) tin and d) sulfur (CZT precursor deposited at -2.05 V)

The X-ray diffraction patterns of CZTS films are shown in **Figure. 4.4**. The reflections from the CZTS kesterite phase are indicated by the respective Miller indices; the strongest Bragg peak (112) is observed for all films and is located around 2θ = 28.5 and peaks around 2θ = 33, 47 and 56 degrees exhibit two sets of Miller indices due to the tetragonal peak splitting. It must be noted however that this peak overlaps with the strong intensity peaks of most common secondary phases ZnS and Cu_2SnS_3. Cu_xS_y phases were observed in most films; however, such peaks either disappeared or the intensity faded as the Zn/Sn ratio increased. In the literature, the presence of secondary phases for close to stoichiometric layers is often reported [64, 136], and is mostly due to the decomposition of CZTS at the surface [26]. Besides these secondary phases, SnS_2 was also observed around 2θ ~ 50° for Zn/Sn ratios of 0.72 or 1.01.The XRD patterns of CZTS layers with relatively high Zn/Sn ratios (Zn/Sn=1.14 -1.34) show superstructure peaks around 2θ ~ 16°-18° degrees, suggesting improved order. These two peaks do not overlap with any of the secondary phases, further supporting the higher phase purity of CZTS.

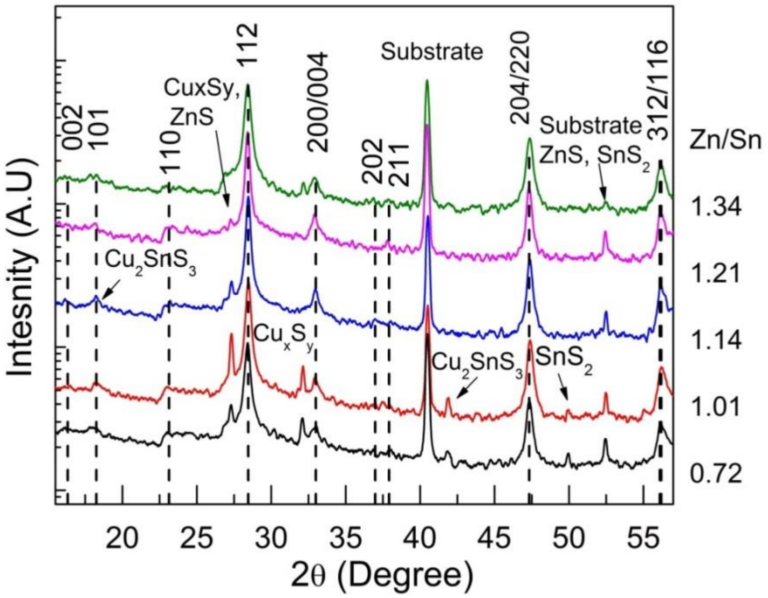

Figure 4.4 X-ray patterns for CZTS films after sulfurization of Cu-Zn-Sn layers at 500°C as a function of Zn/Sn ratio

Raman spectra of CZTS samples sulfurized at 500 °C and with different Zn/Sn ratios (0.72, 1.01, 1.34) were acquired with a 514 nm excitation wavelength and are shown in **Figure 4.5** together with the theoretical Raman peak positions for kesterite CZTS (black lines) and some secondary phases, as shown [27, 47, 98, 100, 128]. In **Figure 4.5.a** the most intense peak is labeled as P1 and the peak for secondary main A symmetry mode is labeled as P2. Significant shifts however were observed for P1 and for P2, probably due to the presence of secondary phases and/or minor changes in lattice parameters [29, 98, 100].

The various lineshapes for the most intense Raman peak between 325 cm^{-1} and 340 cm^{-1} are shown with blue and red traces around 331 cm^{-1} and 337 cm^{-1}, attributed to the disordered and the ordered type kesterite, respectively (**Figure 4.5.b-5.d**). The FWHM of the CZTS layers decreased and the value of Q'' increased with the increasing Zn/Sn ratio. This suggests that the increasing amount of Zn is not only increasing the crystallinity of the layers, but also raising the relative amount of ordered type kesterite in the CZTS layers.

The second most intense peak is located around 290 cm^{-1} (**Figure 4.5.b-d)**. This peak is relatively wide in the Sn-rich CZTS layers (**Figure 4.5.b**).This wide peak is attributed to the possible presence of secondary Sn-rich phases, such as SnS_2 and Cu_2SnS_3, exhibiting Raman modes around 290 cm^{-1}, 314 cm^{-1} and 352 cm^{-1}. Since some of these peaks are either overlapping or very close to those of other phases, it is important to analyze X-ray diffractogram and Raman spectra in parallel. XRD patterns for the CZTS layer with Zn/Sn=0.72 also show peaks from SnS_2 and Cu_2SnS_3 phases (**Figure 4.4**). According to the fitting of Raman spectra, an additional feature besides the CZTS Raman modes around 320 cm^{-1} should be considered; this peak may be due to a minor ternary phase such as Cu_3SnS_4 .

The second most intense Raman mode of the CZTS with Zn/Sn=1.01 in **Figure 4.5.c** is centered at 288 cm^{-1}; in contrast with the Zn/Sn = 0.72 sample, no peak could be found around 290 cm^{-1}, which suggests a significant decrease of the Cu_2SnS_3 phase fraction. The second most intense Raman peak of the CZTS layer with Zn/Sn: 1.34, (**Figure 4.5.d**) matches well with the entire theoretical Raman active mode for CZTS and contain the least amount of Cu_2SnS_3 phase. These findings suggest that the increasing Zn/Sn ratio of CZTS layers forms less amount of Sn based secondary phases, which is in agreement with the XRD analyses.

A small intensity is observed for peaks at 408 cm^{-1} and 475 cm^{-1}, attributed to the MoS_2 and Cu_xS_y phases. Even without performing an etching process on the CZTS layers, only a small intensity was observed for Cu_xS_y related phases. As a whole, these data suggest improved purity of the kesterite phase at high Zn/Sn ratio.

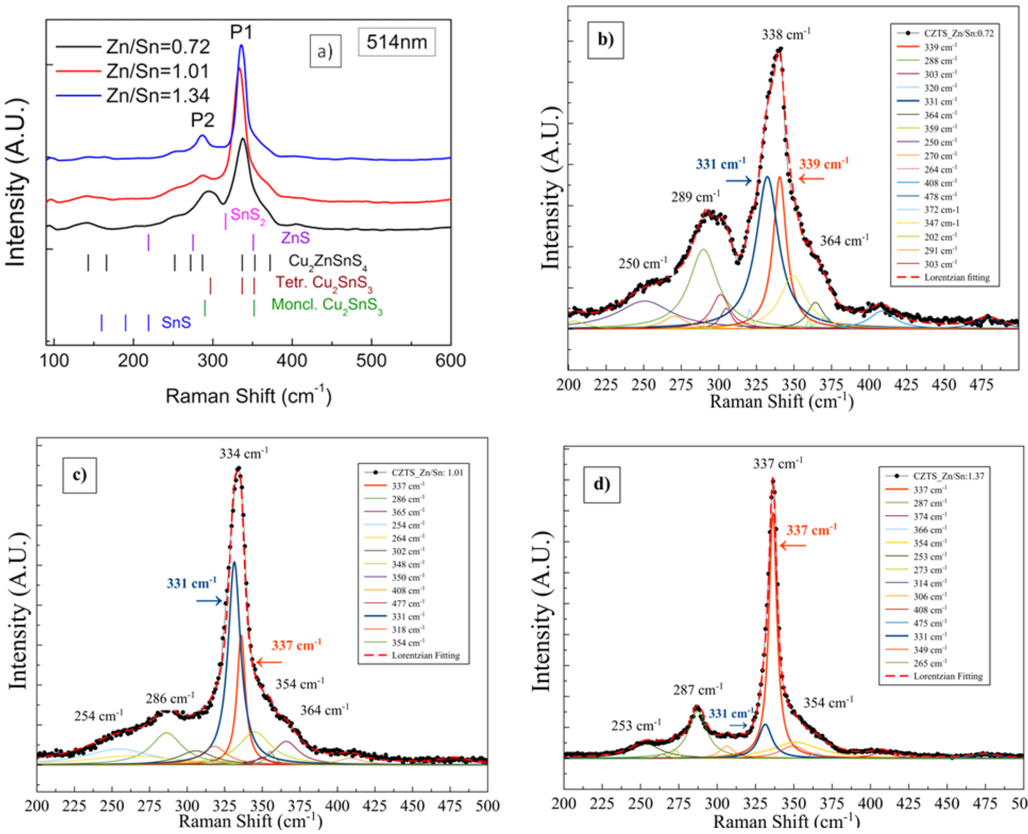

Figure 4.5 a) Raman Spectra for CZTS films and corresponding Lorentzian curve fittings for samples with b) Zn/Sn ratio 0.72, c) 1.01 and d) 1.34

Further investigations on the homogeneity of Zn-rich CZTS layer were performed by the local analyses of the film at the top, middle and bottom region of the layer (**Figure 4.6.a**). Three of the traces show similar Raman modes with slightly different intensity for the Cu_xS_y phase at around 475 cm^{-1}. The FWHM of the spectra is between 6.8 cm^{-1} and 8.8 cm^{-1}, which is reasonable close to each other and similar to the what is observed in the literature[104]. We also used 405 nm excitation wavelength to identify the ZnS phase in the CZTS material (**Figure 4.6.b**). The spectrum still shows the CZTS based Raman shifts with the addition of a small peak at around 694 cm^{-1}, which is attributed to the ZnS phase. Additional evidence for the presence of ZnS is obtained by decomposition of the spectrum in Lorentzian lineshapes, evidencing a further ZnS phase at around 346 cm^{-1}. We can thus conclude that there is a small amount of ZnS phase in the CZTS film.

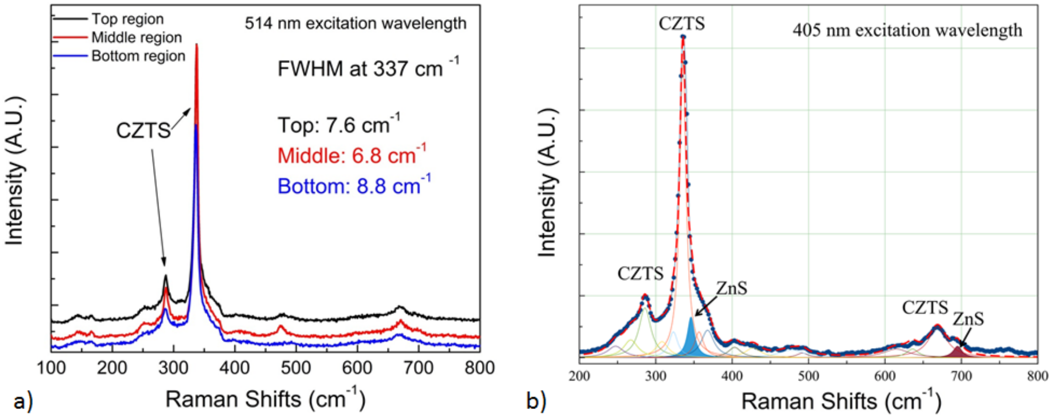

Figure 4.6 Raman spectra of CZTS a) at the top, middle and bottom region and b) spectra with 405 nm excitation wavelength

Planar and cross sectional SEM images of the CZTS film with Zn/Sn ratio 1.34 are presented in **Figure 4.7**. These images show a continuous layer with apparent grain size ranging from 100 nm to 650 nm and thickness of ~ 1100 nm. The bottom region of the film in **Figure 4.7.b** shows smaller and more uniform grain size.

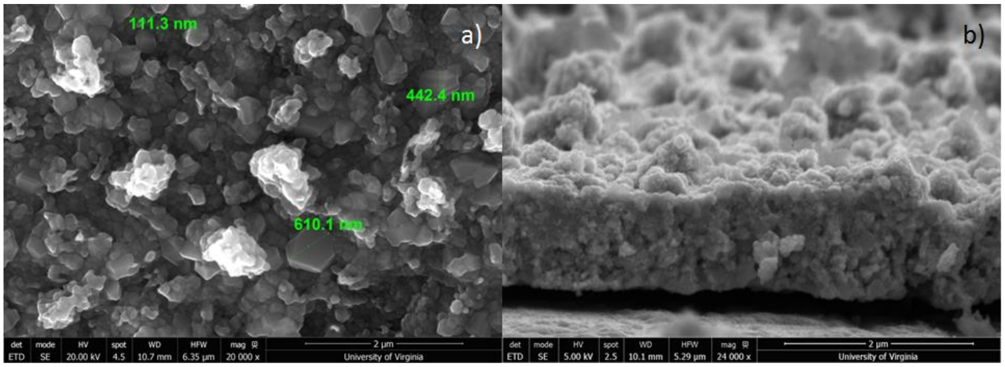

Figure4.7 a) Top-down SEM image and b) cross section of CZTS film with Zn/Sn ratio 1.34

In order to perform further investigation on the CZTS phases, we used EDS compositional mapping on the sample with Zn/Sn; 1.28 (**Figure 4.8**). **Figure 4.8.a** shows the SEM morphology of the films, while **Figure 4.8.b** shows the EDS mapping for the combination of the signals from all four elements. The EDS signal for the individual elements are presented in the rest of the images (**Figure 4.8.c-f**) with the following color codes: yellow for sulfur, red for copper, blue for zinc and pink for tin. The EDS mapping images suggest a homogenous distribution of the elements at this scale; however, we should stress that the signal is collected from a depth of about 1 micron, and this can be affected by the morphological features shown in the image.

In **Figure 4.9** a low magnification EDS compositional mapping is presented, showing a secondary phase in the CZTS material. The CZTS part of the material shows homogenous distribution for all four elements; however the hexagonal secondary phase shows stronger intensity for copper and sulfur elements, strongly suggesting the presence of a Cu_xS_y secondary phase.

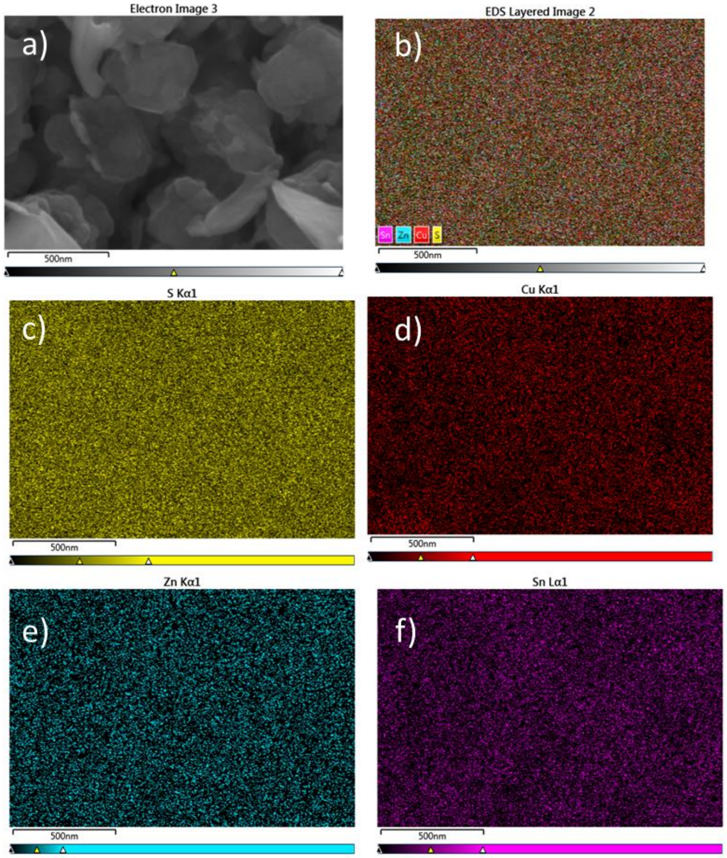

Figure 4.8 EDS mapping of CZTS layer with Zn/Sn=1.28. a) SEM image, b) EDS composition mapping of 4 elements, c) sulfur (yellow), d) copper (red), zinc (blue) and d) tin (magenta), scale bar: 500 nm.

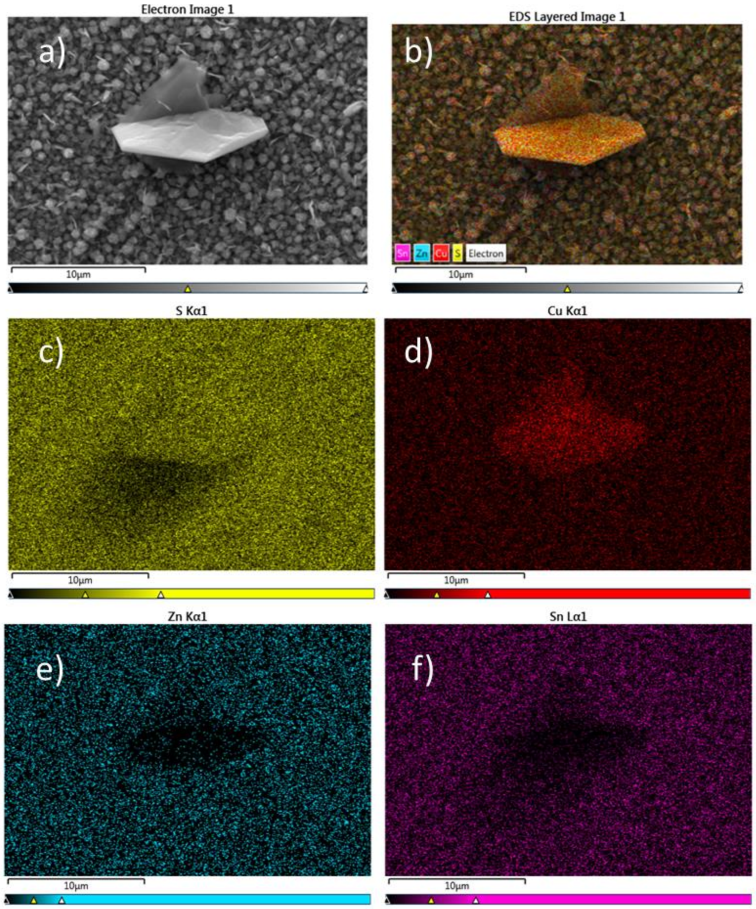

Figure 4.9 a) SEM image and b) corresponding EDS mapping of CZTS layer with Zn/Sn=1.12. c) sulfur (yellow), d) copper (red), e) zinc (blue) and f) tin (magenta), Scale bar: 10 μm.

Figure 4.10.a shows the PEC response of CZTS layers sulfurized at 500 °C. The cathodic photocurrent of all CZTS layers gradually increased with decreasing applied potential, confirming the p-type conductivity of the films. The photoresponse of the films was greater with larger Zn/Sn ratio in the whole potential range. The PEC response of the CZTS layers at – 0.95 V was between 0.23 and 0.51 mA/cm^2. These values are similar to those measured at CZTS electrodes under similar experimental conditions reported in the literature [99, 137]. It should be noted however that, even though the Eu$^{3+/}$Eu^{2+} redox couple is thermodynamically suitable to observe a photocurrent at CZTS interfaces, its kinetic properties are poor, leading to artificially low photocurrent values, as highlighted in a recent study performed on CIGS absorber layers [138].

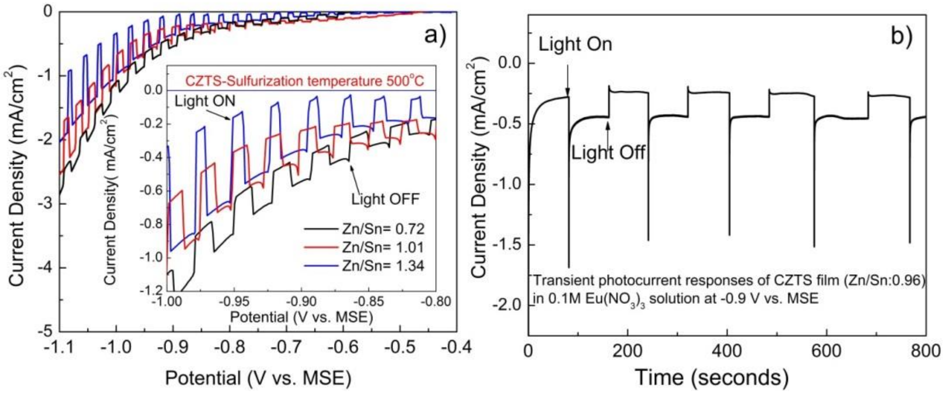

Figure 4.10 a) Photocurrent response vs. applied potential for CZTS films after sulfurization at 500°C. The inset shows details in a window at negative voltages; and b) transient photocurrent response of CZTS film at -0.9 V vs. MSE.

All the current-voltage curves show a significant dark current starting at about -0.85 V. This has been sometimes attributed to pinholes in the sample[139], but in this work we find that the dark current was larger in samples with higher fraction of secondary phases. The increase in dark current at more negative potentials may be attributed to electron-hole recombination and/or charge carrier injection at the donor/acceptor interface [138, 140].We used the measured photocurrent values after subtraction of the dark current to calculate the integral IPCE by using the maximum theoretical photocurrent density for a semiconductor with a 1.5 eV band gap under AM 1.5G illumination. The calculated values are between 0.82% and 1.82%. We examine also the photocurrent transient curve for CZTS layer with Zn/Sn ratio 0.96 after sulfurization at 500°C (**Figure 4.10.b**). The fast current response upon illumination at -0.9 V suggests a low density of trap states, but the steep decrease afterwards evidences significant recombination. The on and off cycles in addition show a stable behavior for more than 800 seconds, suggesting that the Eu(NO$_3$)$_3$ solution is not damaging the CZTS layer within the time scale investigated.

IV. Influence of Sulfurization Temperature on the PEC Performance

Here we focus on the influence on sulfurization temperature on the properties of CZTS materials. The most common annealing or sulfurization temperature range is between 500 and 600 °C for CZTS based devices, where large, uniform crystal grains are obtained [125, 141–143].

Temperature increase is reported to change the grain morphology and enhance the crystallinity of CZTS[141–143]. Emrani et al. reported on the influence of sulfurization temperature for sputtered Sn/Zn/Cu precursors using structure analyses and solar cell efficiency [142]. The grain size of CZTS is reported to be the largest and smoothest at 515 °C, however the highest efficiency is reported for the 550 °C sample[142]. Another high efficiency (8%) CZTS material, obtained from electrodeposited metallic precursor, shows best performance after sulfurization at 590 °C [125]. On the other hand, the highest efficiency of CZTSSe based solar cell (12.6%) is obtained after annealing at 500 °C, a much lower temperature than those used in other high efficiency cells. These findings suggest that there may be different influences of temperature for different synthesis techniques.

The influence of sulfurization temperature on the formation of CZTS films otherwise obtained under identical conditions is discussed next. To this end, Cu-Zn-Sn precursor layers were sulfurized at 550 °C and the elemental losses were measured for samples with three different Zn/Sn ratio values, as shown in **Figure 4.11.a.** We observed Zn loss after sulfurization at 550 °C . **Figure.4.11.b** shows the SEM image for CZTS layer sulfurized at 550 °C with Zn/Sn ratio 0.96; the average grain size is similar to that of CZTS films sulfurized at 500 °C (**Figure 4.7.a**).

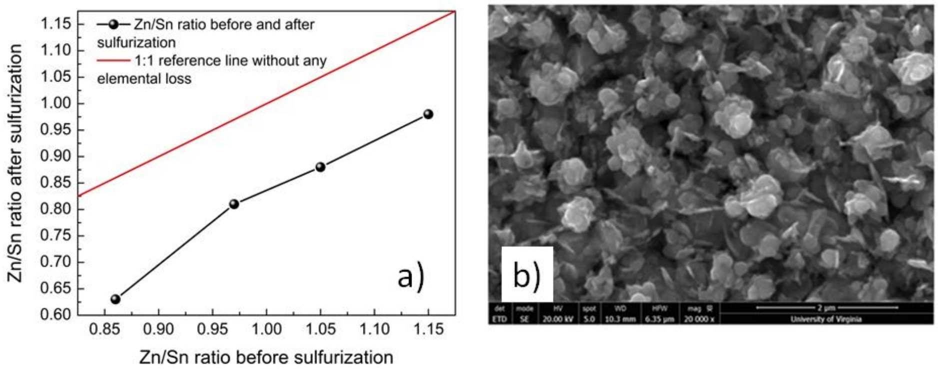

Figure 4.11 a) Zn/Sn ratio before and after sulfurization at 550 °C and b) top down SEM image of CZTS with Zn/Sn=0.96

X-ray diffraction patterns of CZTS layers sulfurized at 500 °C and 550 °C are compared in **Figure.4.12.** The strongest Bragg peak for both of the CZTS layers is again the (112); the intensity of the reflections however is much larger for the sample sulfurized at the higher temperature. No peaks from Cu_xS_y or ZnS were detected for CZTS films with similar Zn/Sn ratio, after sulfurization at 550 °C. We also observed the superstructure reflections around 2θ ~ 16-18 degrees for the CZTS layer with Zn/Sn=0.98 after sulfurizing at 550 °C (**Figure 4.12** red line), which were not detected previously for the CZTS layer with similar composition, Zn/Sn=1.01, after sulfurization at 500 °C (**Figure 4.12** black line).

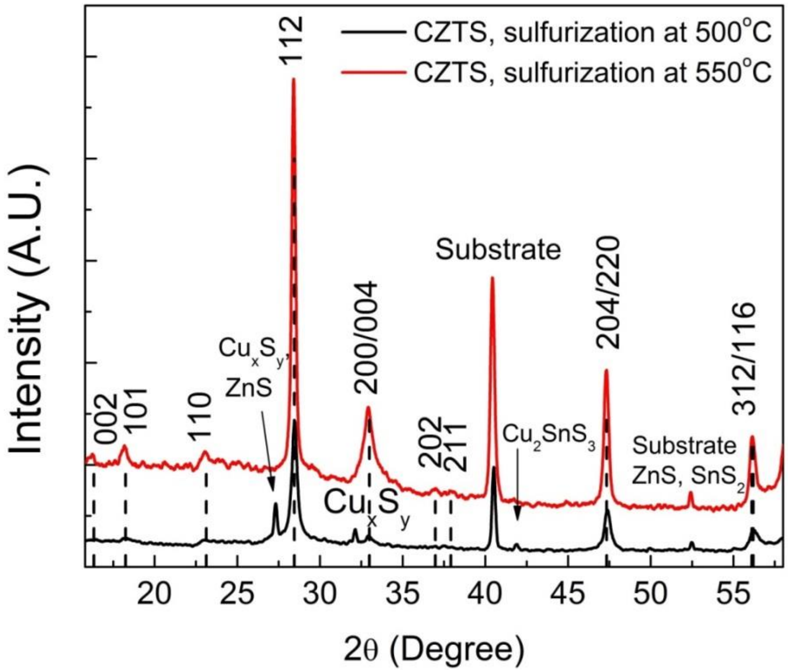

Figure 4.12 X-ray patterns of CZTS films sulfurized at 500 °C (Zn/Sn=1.01) and 550 °C (Zn/Sn=0.98)

The Raman spectrum acquired with 514 nm excitation wavelength on the CZTS layer sulfurized at 550°C (Zn/Sn=0.98) is shown in **Figure 4.13.a**. The Q'' values are 7.22 and 15.80 for CZTS layers formed at 500 °C and 550 °C, respectively, evidencing an improved order after sulfurization at the higher temperature(**Table 4.1**). This suggests that optimization of precursor composition and sulfurization temperature not only improve the phase purity, but also decreased the fraction of disordered type kesterite in the CZTS layer. Interestingly, the FWHM of the CZTS film after sulfurization increased slightly, suggesting some decrease in crystallinity of the CZTS layer(**Table 4.1**).

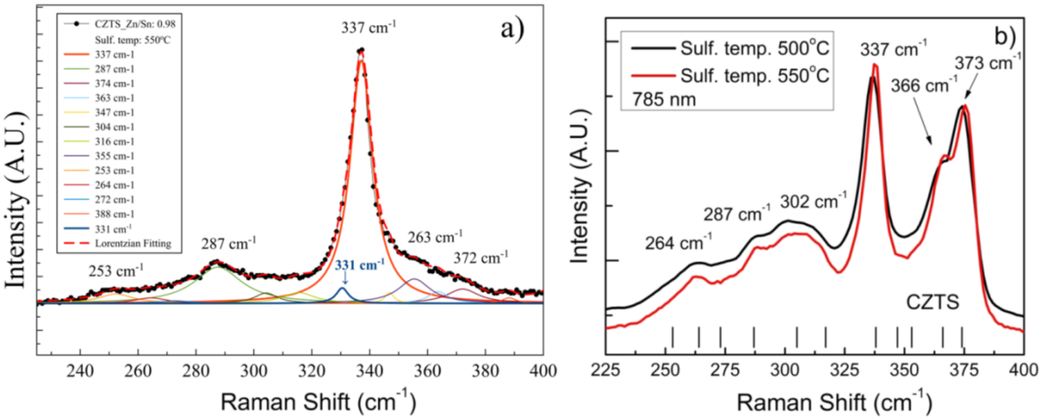

Figure 4.13 Raman Spectroscopy with a) 514 nm excitation wavelength and b) 785 nm for CZTS films sulfurized at 500 °C (Zn/Sn=1.01) and 550 °C (Zn/Sn=0.98)

The position of the Lorentzian lineshapes shifted for the peaks assigned to disordered type kesterite; these peaks are found around 300 cm^{-1} and at 306 cm^{-1} for CZTS layers sulfurized at 500°C and 550°C, respectively. Unlike the increase observed in the value of Q'', the values of Q and Q' are close (**Table 4.1**). We can conclude that the Q and Q' values are mostly dependent on the cooling rates, i.e. natural cooling in our conditions, rather than sulfurization temperature. The Q'' value, on the hand, depends mostly on the thermal treatment conditions of the CZTS materials, which is in aggrement with the reported results[104].

Table 4.1 Raman spectra comparison of relatively pure CZTS layers after sulfurization at 500 °C and 550 °C

Raman S. Excitation Wavelength (nm)	785	785	514	514
CZTS Sulfurization Temperature (°C)	Q	Q'	Q''	$FWHM_{337}$ (cm^{-1})
500	0.48	0.82	7.22	6.2
550	0.49	0.79	15.80	9.4

In summary, XRD patterns and Raman Spectrosopy of the CZTS layers give a similar picture of the CZTS films and provide a more detailed description of the material obtained. XRD patterns show relatively pure CZTS layers for the sample sulfurized at 500°C with Zn/Sn ratio 1.34 and for that sulfurized at 550°C with Zn/Sn ratio 0.98 (**Figure 4.4** and **Figure 4.12**).These CZTS films showed not only a low fraction of secondary phases, but also a low intensity of XRD reflections around 2θ = 16, 18, 37 and 38 degrees, which suggested the formation of a well crystallized and pure phase material (**Figure 4.4** and **Figure 4.12**).

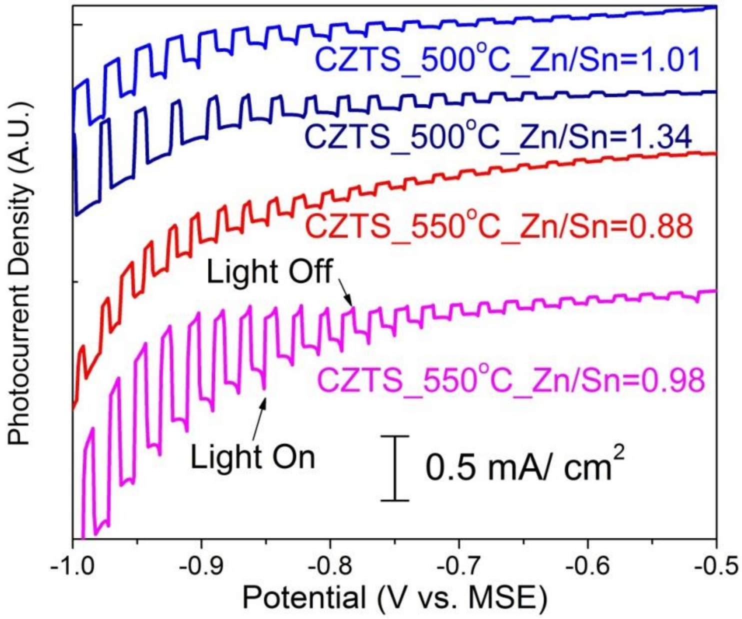

Figure 4.14 Photocurrent-potential curves for CZTS films sulfurized at 500 °C and 550 °C with different Zn/Sn ratio

Figure 4.14 compares the photocurrent-potential curves for CZTS films sulfurized at 500 °C and 550 °C. The PEC response increased with higher Zn/Sn ratio irrespective of sulfurization temperature. Close to stoichiometric CZTS layers after sulfurization at 550 °C show the highest PEC response of 0.99 mA/cm^2 and the highest integral IPCE of 3.54%. In the literature, the presence of secondary phases is one of the major causes for the low open circuit voltage, which limits the solar cell performance [144]. We observed an increase in PEC response for both sulfurization temperatures by increasing Zn/Sn ratio. XRD and Raman Spectroscopy results suggest that increasing Zn/Sn ratio and sulfurization temperature at 550 °C reduced the secondary phases and improved the relative order of the CZTS compared to 500 °C. Therefore, we attribute the increase in PEC response to the improvement of phase purity and the presence of a more ordered kesterite phase.

V. Conclusion

The sulfurization conditions for the CZT metallic precursors deposited from citrate based solution are studied. We found that sulfur amount (i.e., the partial pressure of sulfur) in the encapsulation tube influences the elemental losses during the sulfurization and affects the phase purity of the CZTS layers, hence the photoelectrochemical response of the films. We also found that the initial composition and sulfurization temperature are influencing the extent of elemental losses, facilitating the formation of secondary phases in the CZTS layers. The use of Raman spectroscopy and XRD provided insight into the phase purity and the degree of Cu-Zn cation disorder in CZTS layers with different Zn/Sn ratio and sulfurization temperature. The photoelectrochemical response of CZTS layers was improved by increasing Zn/Sn ratio for both sulfurization temperature, 500 °C and 550 °C, due to the formation of a lower fraction of secondary phases and improved crystal quality. We observed the highest photoelectrochemical response, 0.99 mA/cm^2, for a CZTS layer with Zn/Sn ratio 0.98, after sulfurization at 550 °C. Qualitative Raman spectra investigation of kesterite thin films with minor secondary phases suggested that the enhanced photoresponse is mainly the result of improved order of the Cu-Zn cation pairs and of sulfurization at higher temperature.

Chapter 5-Influence of Compositional Homogeneity of CZT Alloys on Phase Purity of CZTS Layers: Electrodeposition from an Alkaline Solution

I. Introduction

A suitable Cu-Zn-Sn (CZT) alloy precursor should exhibit a homogeneous composition, uniform thickness and a smooth surface; in addition, the grain size should be sufficiently large to enable formation of CZTS grains spanning the entire film thickness. In this context, electrodeposition of CZT from alkaline potassium pyrophosphate electrolytes has been shown to result in the formation of CZTS films with large grains [80, 145, 146], potentially minimizing grain boundary scattering. In addition, small amounts of potassium in the electrolyte could be acting as a fluxing agent during growth, altering surface kinetic processes and possibly growing larger CZTS grains[147, 148]. Although various studies have been undertaken on the electrodeposition of Cu-Zn-Sn alloys from potassium pyrophosphate solutions suitable for the synthesis of CZTS absorber films, a detailed compositional, morphological and crystal structure analysis of CZTS layer via X-ray diffraction and Raman Spectroscopy has not yet been available in the literature.

In this chapter, we aim to optimize the deposition conditions of Cu-Zn-Sn alloy films in order to achieve a suitable composition with a low standard deviation across the whole film area, with the target to manufacture CZTS absorber layers with high phase purity. For this purpose, we used different deposition geometries and analyzed the compositional uniformity of the resulting alloy precursors; a horizontal electrode set-up led to a lower compositional standard deviation than a vertical one. We then sulfurized these films and investigated the phase purity and crystal quality of the resulting CZTS layers, using SEM, EDS mapping, X-ray diffraction, Raman Spectroscopy and photoelectrochemical measurements. We found that the compositional distribution and phase purity of CZTS films was improved by using the horizontal electrode geometry. The CZTS layers exhibit p-type conductivity and the photoresponse correlates with the degree of homogeneity, phase purity and order parameter. Further improvements in crystallinity and higher order parameters are reached via low temperature (175°C) annealing.

II. Current Distribution and Spontaneous Convection in Electrochemical Cells

Electrodeposition occurs via metal ion reduction at the electrode/electrolyte interface; as such, the process exhibits a space- and time-dependence of the metal ion concentrations; this concentration field is affected by a number of forces, including gravity and the electrostatic interaction among ions, which are very difficult to calculate and predict [149]. In particular, it has been shown that for an electrolyte viscosity ~ 1.5 times that of water, electrically driven convection is more important, suggesting that in aqueous solutions with limited ion concentration the buoyancy convection should be dominated by gravity forces [150].

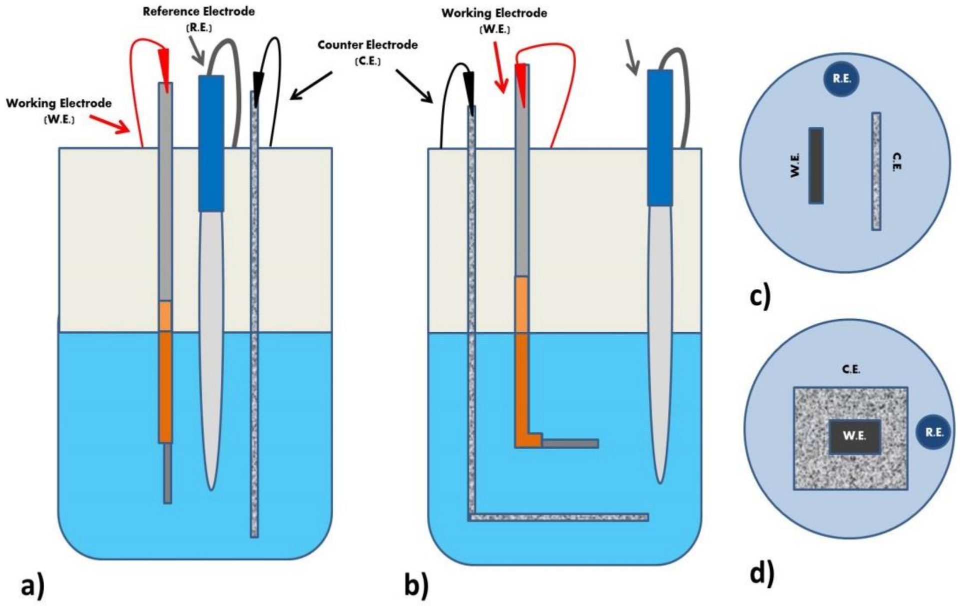

Figure 5.1 Schematics of the electrochemical cell configurations: a) vertical facing electrodes and b) horizontally placed electrode, cathode on top and facing down. Top down views of the c) vertical and d) horizontal deposition set-ups further clarify the geometry.

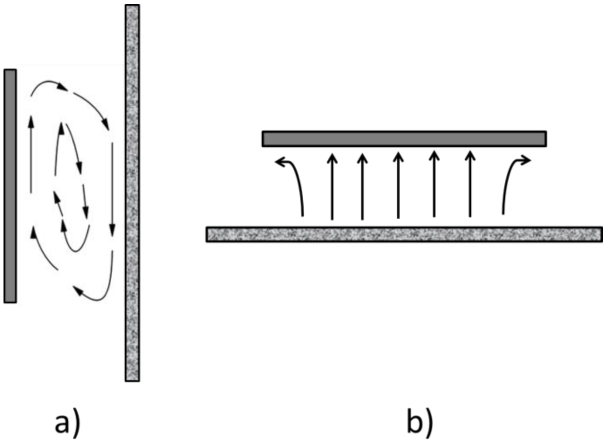

Figure 5.2 Schematic representation of current flow for a) a vertical deposition and b) a horizontal deposition set up.

In this section we used different deposition configurations to exploit the influence of current distribution on the quality and homogeneity of the initial and final layers. The vertical configuration (**Figure 5.1.a and c**) at the cathode shows buoyancy-induced convection, possibly leading to turbulence and flow instability, resulting in an inhomogeneous current distribution; in contrast a horizontal design (**Figure 5.1.b and d**) with the cathode on top minimizes convection, avoiding turbulent flow and favoring a uniform current distribution [151]. Schematic flow patterns for the two experimental set-ups discussed in this work are presented in **Figure 5.2**.

III. Compositional Analysis of Metallic Precursor Layers and CZTS Films after Sulfurization

The Cu-Zn-Sn alloy precursors were grown from an alkaline solution (pH 9.5) combining 0.5 M $K_2P_4O_7$, 5-8 mM $SnSO_4$, 30-60 mM $ZnSO_4$ and 8-10 mM $CuSO_4$, using ultra-pure Milli-Q water (resistivity18.2 MΩ·cm) produced in house. The cyclic voltammetry curves of the Cu-Zn-Sn layers for vertical and horizontal deposition were carried out at a scan rate of 10 mV/s and are shown in **Figure 5.3 and 5.4**, respectively. The redox potentials calculated for copper, tin and zinc are -0.81, -1.28 and -1.92 V, respectively. These values are shown with dashed lines in **Figure 5.3 and 5.4**. In the vertical configuration, the current onset in the cathodic scan occurs around -0.7 V and the first cathodic peak appeared around -0.92 V, which we attribute to the reduction of copper ions [**Figure 5.3**]. In the horizontal configuration on the other hand the current onset is seen around -0.75 V and the reduction peak shifts to -0.95 V [**Figure 5.4**]. In both cases, copper reduction occurs at slightly more negative potential than the calculated value, suggesting a limited complexation effect by pyrophosphate. The second peak, assigned to Sn reduction, appears at -1.27 V in the vertical configuration and at -1.25V for the horizontal one. A precise experimental determination of the reduction potential of zinc is difficult via CV since its reduction occurs at more negative potentials than the hydrogen evolution reaction (HER). During electrodeposition experiments however we observed Zn incorporation starting at -1.7 V, suggesting that this value may be a good estimate for its redox potential.

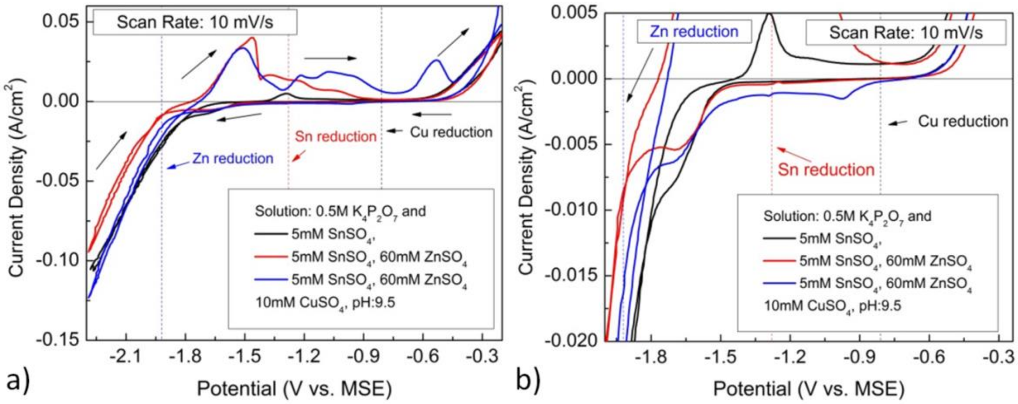

Figure 5.3 Cyclic voltammetry for various electrolytes as shown in the labels, in a vertical configuration at a Mo foil; scan rate was 10mV/s; a magnified version is shown at the right.

Zn deposition occurs at more positive potential than the calculated value. This may be due to the underpotential co-deposition of Zn with Cu [134], an advantageous feature for this ternary electrodeposition system as it limits the rate of HER, which is one of the main reasons for the occurrence of in-plane and lateral compositional as well as morphological inhomogeneity.

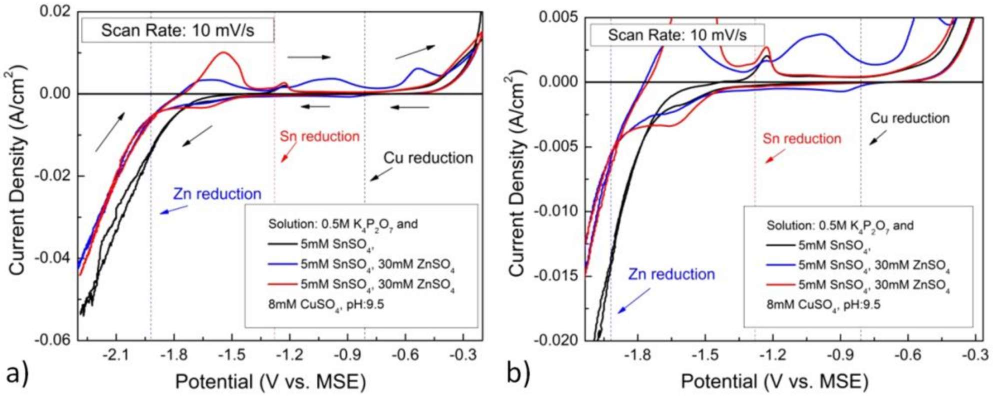

Figure 5.4 Cyclic voltammetry for various electrolytes as shown in the labels, in a horizontal configuration; scan rate was 10mV/s; a magnified version is at the right.

After various electrodeposition tests, we selected for both configurations a deposition potential of -1.8V to obtain the desired composition and a smooth morphology while avoiding excessive HER rate. The ideal composition for CZTS solar cells should be close to the stoichiometric value Cu:Zn:Sn:S=2:1:1:4; however, various reports find that Cu-poor and Zn-rich CZTS films show better performance than the stoichiometric ones [125]. The composition of the metallic precursors layers therefore was targeted to obtain Cu-poor and Zn-rich layers after sulfurization. However, the potential loss of tin during sulfurization should also be taken into account [135]; this aspect was studied by growing metallic precursors close to the stoichiometric value, but with a slightly tin rich fraction.

The copper fraction in the metallic layers is around 50 at% for both configurations, with a slightly Sn rich composition. The most notable difference between the two deposition set-ups is the standard deviation of the elemental fractions. The vertical set-up yields a non-uniform composition distribution at the cathode surface, which is significant even on a relatively small electrode (~ 1cm^2). On the other hand, when using the horizontal cathode, the standard deviation of the three elements was improved dramatically, as expected, due to improvement of the current distribution. These data are tabulated in **Table 5.1**.

Table 5.1 Composition ratio and standard deviation of the Cu, Zn and Sn elements before and after sulfurization for the vertical and horizontal deposition set-ups. EDS measurements are collected at 9 different points from an identical pattern for each sample.

Metallic Precursor			Ratio	After Sulfurization			Ratio
Vertical	**Fraction (at%)**	**Deviation (at%)**	**Cu/(Zn+Sn)**	**Vertical**	**Fraction (at%)**	**Deviation (at%)**	**Cu/(Zn+Sn)**
Cu	50.6	3.5	1.02	Cu	26.5	2.1	1.18
Zn	23.7	4.5	Zn/Sn	Zn	12.0	2.8	Zn/Sn
Sn	25.7	2.3	0.92	Sn	10.5	0.7	1.14
				S	51.0	0.5	
Horizontal	**Fraction (at%)**	**Deviation (at%)**	**Cu/(Zn+Sn)**	**Horizontal**	**Fraction (at%)**	**Deviation (at%)**	**Cu/(Zn+Sn)**
Cu	49.3	0.6	0.97	Cu	23.1	0.2	0.92
Zn	23.7	0.7	Zn/Sn	Zn	14.0	0.9	Zn/Sn
Sn	27.0	0.5	0.88	Sn	11.0	0.2	1.27
				S	50.9	0.2	

We found that sulfurization at 500 °C during 1 hour resulted in better phase purity and higher photoelectrochemical response as well as more uniform and continuous contact with the Mo back contact (refer to Appendix-2 for experimental results). Therefore in this chapter we sulfurized all metallic precursors at 500 °C for 1 hour. CZTS layers contain ~51 at% sulfur, and the initially tin rich films became Zn rich after sulfurization, due to Sn evaporation during the sulfurization process [135]. The standard deviation of the elements decreased or remained constant after sulfurization for both deposition set-ups. The standard deviation of both tin and sulfur were lower than 1 at% regardless of the geometric configuration used. This could be related to both elements being bound by strong interactions upon formation of stoichiometric phases during sulfurization. Both sulfur and tin have low melting point and could easily evaporate during sulfurization [48]. Even though the standard deviation of Cu and Zn was lowered, the spread was still around 2.1 and 2.8 %, respectively, after the sulfurization of vertically deposited precursors. On the other hand, the standard deviation of Cu and Zn in the horizontal configuration was less than 1 at% for the CZTS layers. The improvement in compositional uniformity for all four elements suggests that the initial compositional homogeneity has a strong influence on the final product CZTS.

IV. Morphological Analysis of Metallic Precursors and CZTS Films

The SEM images of the metallic precursors electrodeposited by vertical and horizontal deposition are shown in **Figure 5.5**. The vertically deposited films are continuous, while the horizontally deposited samples present small gaps < 100nm in size (**Figure 5.5.b**), marked by red circles, which appear to be pinholes. The presence of small gaps may be due to hydrogen bubbles sticking to the cathode surface due to the down facing configuration. The overall morphology for the two samples is similar, showing only a slight difference in size for the horizontal deposition metallic precursors. The cross sectional image for the horizontally deposited metallic precursor is shown in **Figure 5.6**. The thickness of the layer is around ~550 nm.

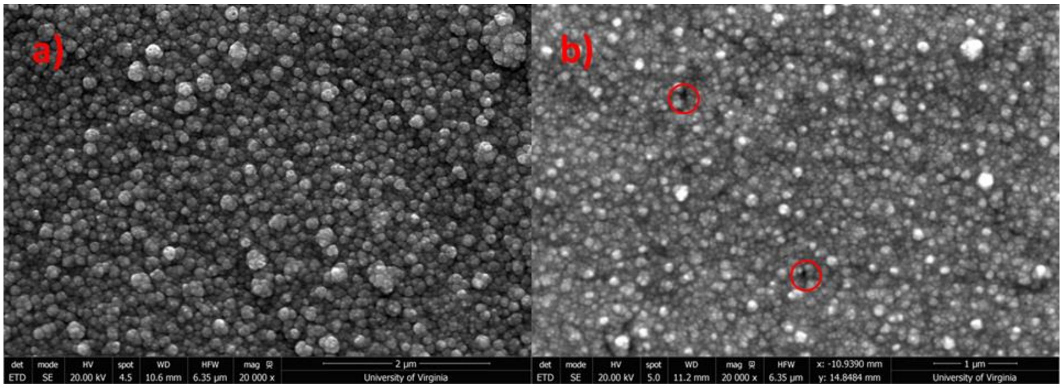

Figure 5.5 Top down SEM images of Cu-Zn-Sn films electrodeposited from a (a) vertical and (b) horizontal set up.

CZTS layers after sulfurization exhibit larger grain size (~ 0.5 um) and significant sintering. The vertically deposited layers exhibit less pinhole than the horizontal sample. The presence of pinholes in CZTS is probably owed to pre-existing pinholes in the metallic precursors.

High magnification SEM images mostly show a uniform, but uneven morphology (**Figure 5.7**); however, an absorber layer should be uniform across the entire sample for use in photovoltaic applications. The overall morphology could be improved by the use of surfactants and other additives that could limit 3-dimensional nucleation and inhibit growth of large grains.

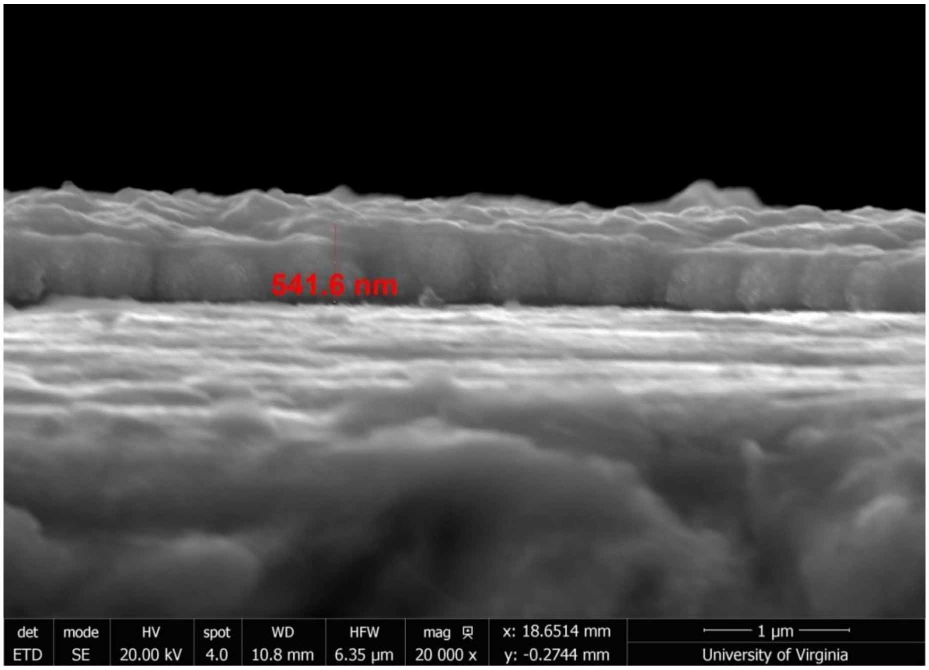

Figure 5.6 Cross section image of the Cu-Zn-Sn metallic precursor electrodeposited from a horizontal deposition set up

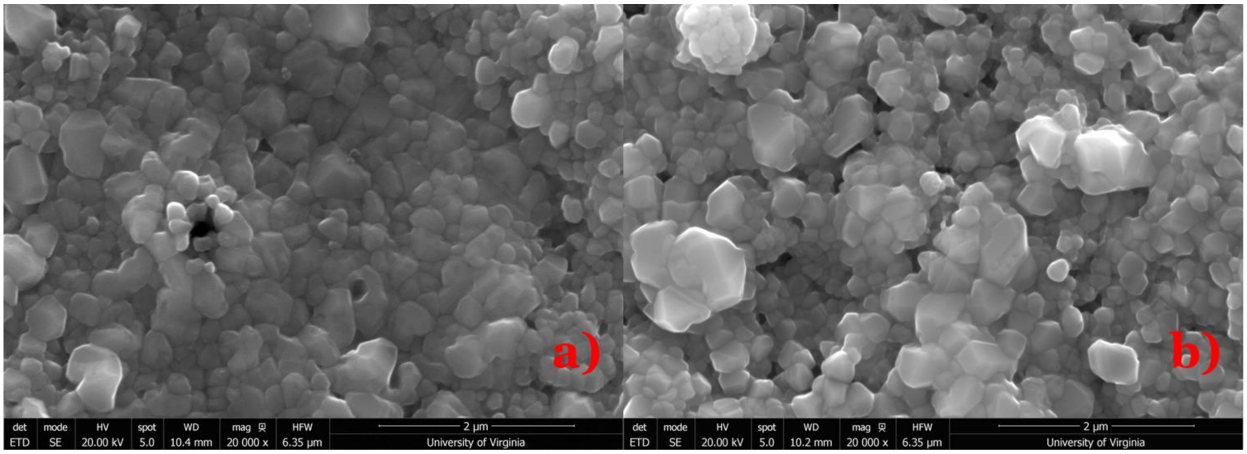

Figure 5.7 Top down SEM images of CZTS films formed via sulfurization of Cu-Zn-Sn metallic precursors electrodeposited from: a) vertical and b) horizontal set-up.

Different morphological features were indeed observed over larger areas, and shown in **Figure 5.8**, with hexagonal platelets that suggest the presence of secondary phases**.** In order to clarify the nature of these features, we collected EDS maps on the region shown in **Figure 5.8.a,** from a CZTS layer grown in a vertical configuration and sulfurized. The EDS map in **Figure 5.8.b** is constructed by superposing various elemental intensity distributions; reddish regions indicate a copper- and tin-rich area, while the green region is rich in zinc and sulfur; it is possible that some of the green grains are ZnS. The large hexagons on the other hand show more intense signals for copper and sulfur, suggesting that these features can be related to Cu_xS_y phases; this is supported indeed by the platelet morphology, which suggests a CuS-type hexagonal phase. Another example of non-uniform morphology is shown **Figure 5.9** where large, Cu-rich grains are formed**.**

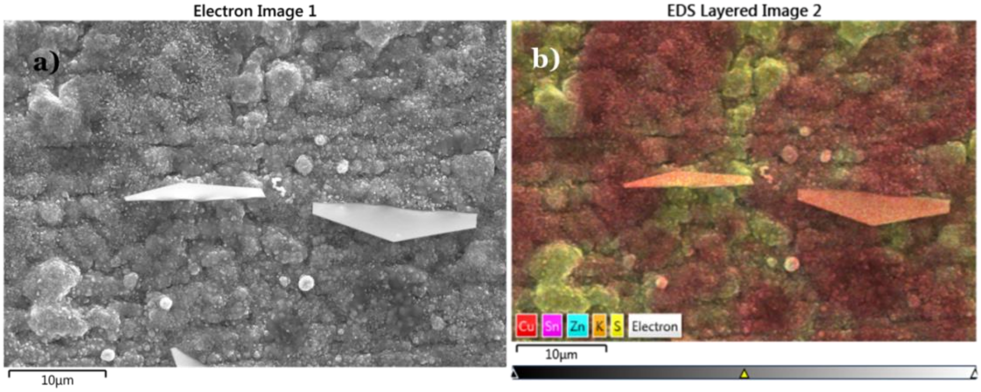

Figure 5.8 a) Top down SEM image of CZTS films formed via sulfurization of Cu-Zn-Sn alloys electrodeposited in a vertical set up and b) EDS mapping of the same region.

The SEM image for the CZTS layer grown in a horizontal configuration and the corresponding compositional mapping are shown in **Figure 5.10.a** and **b**. This film shows a more uniform morphology and smaller grain size, somewhat lacking sharp polyhedral features such as the hexagons in **Figure 5.8**. The EDS map also shows a more uniform composition as suggested by the small color gradient, which is probably mostly due to morphological features. These findings suggest a significant improvement in the homogeneity of the CZT alloy and the final CZTS film.

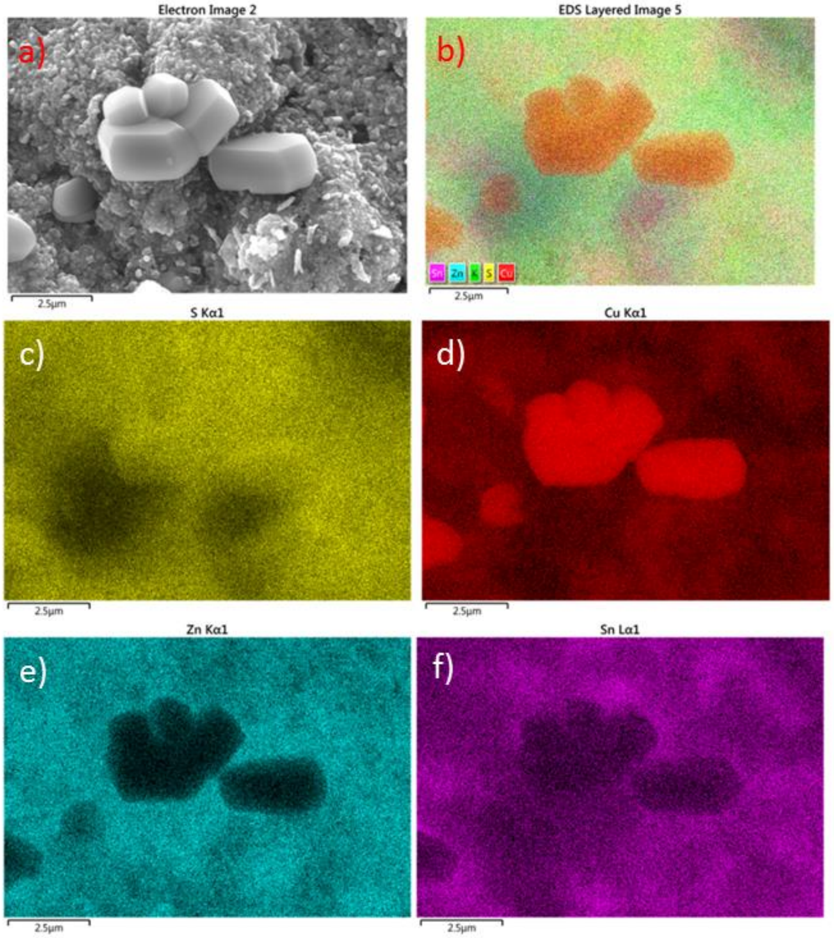

Figure 5.9 Compositional mapping of the CZTS layer formed via sulfurization of vertically deposited metallic precursor with Cu-rich secondary phases a) SEM image, b) EDS compositional mapping, c) sulfur (yellow), d) copper (red), e) zinc (blue) and f) tin (magenta)

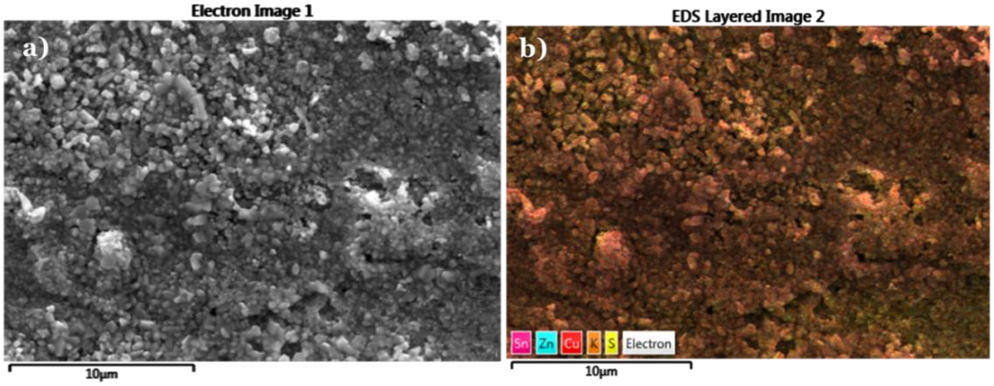

Figure 5.10 a) Top down SEM images of CZTS films formed via sulfurization of Cu-Zn-Sn metallic precursors electrodeposited from a horizontal set-up and b) EDS mapping of the same area.

V. Structural and Photoelectrochemical Characterization of CZTS Layers

A. Structural Analyses of CZT Metallic Precursors and CZTS Films

XRD patterns for the CZT precursor layers grown using either configuration (vertical or horizontal) are shown in **Figure 5.11.a.** Both films consist of a small amount of metallic tin and a significant volume fraction of the intermetallic compounds Cu_6Sn_5 and Cu_5Zn_8. The reflections for metallic Cu and Zn superpose with those of the intermetallic compounds within the 2θ angle 42° to 44°, making it difficult to estimate the relative amount of these phases. XRD patterns for the corresponding CZTS layers are shown in **Figure 5.11.b**. The reference diffraction pattern of the kesterite phase is superposed to the graph as blue dashed lines; the strongest reflection is observed around $2\theta = 28.5°$, which corresponds to the CZTS (112) planes. The other two most intense reflections are observed around $2\theta \sim 47°$ and 56°. It must be noted that these three reflections overlap with strong reflections for the most common secondary phases, ZnS and Cu_2SnS_3, therefore it is possible that some of these reflections may be due in part to the above secondary phases; additional reflections from Cu_xS_y and Cu_xSnS_y phases are observed in both films. The presence of secondary phases may be linked to a non-stoichiometric composition at various locations across the layer. The starting composition of the CZT films are slightly Sn-rich, however the standard deviation of the elemental fractions, 2.3 to 4.5 at%, change significantly the local composition, inducing the formation of secondary phases upon sulfurization.

The decomposition of CZTS could also be induced by the presence of secondary phases, particularly at the surface region [47, 135, 152]. Various models and observations suggest that such decomposition may occur above 500°C [47]; since in this work CZT films were sulfurized at 500°C, the annealing itself may be possibly causing decomposition. A thermodynamic study on the instability of CZTS films during annealing proposes that the instability of multivalent Sn is the main driving force for decomposition under low sulfur pressure [47]. According to their study, the decomposition mechanism may consist of two stages; in the first step Sn(IV) is converted to Sn(II) at low sulfur pressure, leading to loss of gaseous S_2 and separation of solid binary phases, and the second step is the reversible desorption of SnS [47]:

$$Cu_2ZnSn^{IV}S_4(s) \rightleftharpoons Cu_2S(s) + ZnS(s) + \ Sn^{II}S(s) + \frac{1}{2}S_2\ (\mathrm{g})$$

$$SnS(s) \rightleftharpoons \mathrm{Sn}S(\mathrm{g})$$

In **Figure 5.11.b**, XRD patterns of the CZTS layer show indeed the CuxSy phase, but not the SnS phase, suggesting that decomposition in this case is arrested, probably owed to the relatively low sulfurization temperature in comparison with CZTS system that undergo full decomposition [153]. Feng et al. also reported lack of decomposition at a sulfurization temperature of 510°C [153]. Overall, we hypothesize that the main reason for the formation of secondary phases is the non-uniform distribution of elements in the metallic precursors. However, a more detailed study is required to confirm the negligible effect of the decomposition process on the phase purity of our CZTS layers.

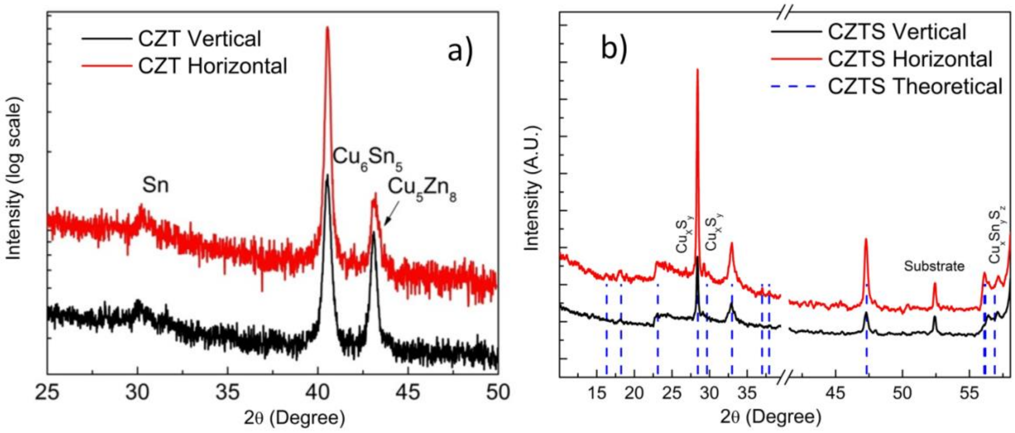

Figure 5.11 XRD patterns of a) electrodeposited CZT layers and b) CZTS layers after sulfurization

Raman spectra of CZTS samples were acquired with a 514 nm excitation wavelength and are shown in **Figure 5.12.a** and **b**. The fit of the experimental spectrum suggests also the contribution of a small intensity peak at 331 cm^{-1} for both vertically and horizontally deposited films. The FWHM of the main A-symmetry mode is 6.8 and 6.0 cm^{-1} and the Q'' values are 8.4 and 10.3 for CZTS films formed from vertically and horizontally deposited metallic precursors, respectively. More homogenous CZTS layer (grown from a horizontally deposited CTS precursor) resulted in more crystalline films with relatively less disordered type kesterite according to 514 nm excitation wavelength characterizations.

The second most intense peak is located around 287 cm^{-1} and have a similar position and shape in both of these layers. Besides that, small intensity peaks are observed at 408 cm^{-1} and are attributed to the MoS_2 phase. No secondary Cu_xS_y phases are observed with the Raman excitation of 514 nm; however, SEM and EDS strongly suggest that there exist compositional and morphological differences at the surface of CZTS layers grown by vertical deposition. The large hexagonal features may have been present only at few locations, hindering detection of Cu_xS_y by Raman spectroscopy.

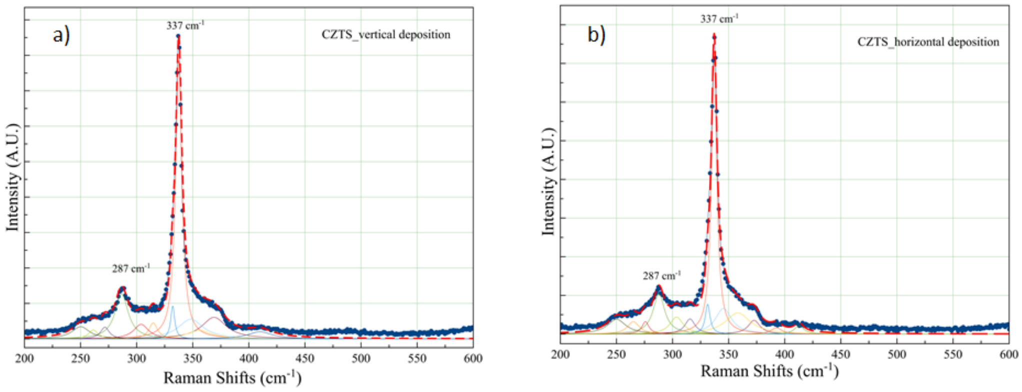

Figure 5.12 Raman spectra of CZTS layers formed via sulfurization of electrodeposited CZT films using a) vertical electrode or b) horizontal electrode.

In order to detect the ZnS phase we used a 405 nm excitation wavelength and analyzed the Raman spectra with Lorentzian lineshapes. By using the 405 nm wavelength, there is only a small contribution from the ZnS phase in the CZTS spectra (**Figure 5.13**), but this evidence is insufficient to conclude that such phase is indeed present.

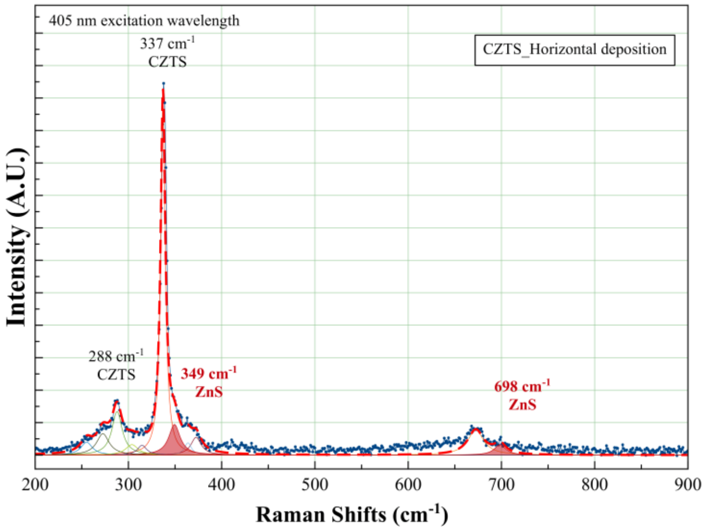

Figure 5.13 Raman spectra of CZTS (horizontally deposited) with 405 nm Raman excitation wavelength

B. Low Temperature Annealing of CZTS Layers

Figure 5.14.a shows the Lorentzian fitting of the Raman spectrum for the CZTS layer annealed at 175°C for 5 hours. The Q parameter increased after annealing at 175 °C comparing to naturally cooled down film and the Q’ value did not change after annealing at different temperatures (**Table 5.2**).

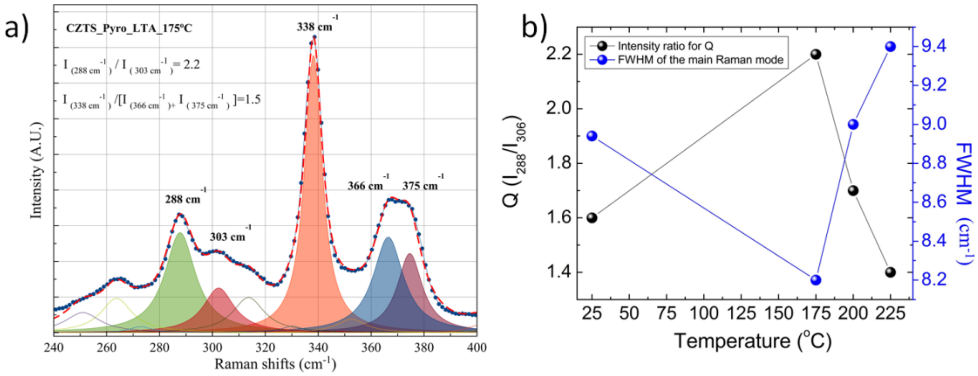

Figure 5.14 a) Raman spectra of CZTS layers annealed at 175°C for 5 hours and b) order parameter Q and FWHM as a function of annealing temperature. The Raman spectra are measured with 785nm excitation wavelength.

The Q and FWHM values for the naturally cooled CZTS and the CZTS samples annealed at 175-225 °C and cooled down naturally to room temperature (~0.3 °C/min) are given in **Figure 5.14.b**. The Q values increased and reached a maximum after annealing at 175°C, corresponding to the lowest FWHM. This suggests a much improved crystallinity comparing to naturally cooled CZTS and CZTS layers after low temperature annealing at 200°C and 225°C (**Figure 5.14.b**).

Table 5.2 Comparison of CZTS layer and CZTS layer after annealing at 175 °C

Raman S. Excitation Wavelength (nm)	785	785	514	514
CZTS Low Temperature Annealing	Q	Q’	Q’’	$FWHM_{337}$ (cm^{-1})
Non	1.6	1.5	10.3	6.0
175 °C	2.2	1.5	-	-

In the literature, Q values for CZTS layers annealed at 175°C for 24 hours in inert atmosphere are around 2.3 [103, 106]. In our study, the Q value for CZTS annealed at 175°C for 5 hours in air is 2.2, very close to published reports [103, 106].

C. Photoelectrochemical Response of CZTS Layers

The photoelectrochemical (pec) response of the CZTS layers obtained from different deposition set-ups are shown in **Figure 13**. Both samples show a cathodic photoresponse, which indicates p-type conductivity, holes being the majority charge carriers. The pec current response of the layers is measured at -0.95 V, before the HER onset; these values are 0.18 mA/cm^2 and 0.40 mA/cm^2 for CZTS layers formed from vertically and horizontally deposited metallic precursors, respectively.

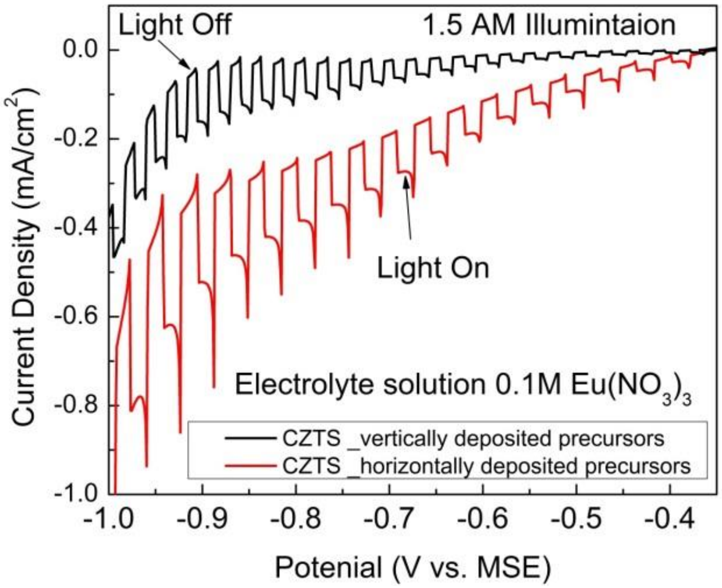

Figure 5.15 Photoelectrochemical response of CZTS layers formed via sulfurization of vertically and horizontally deposited metallic precursors.

It should be noted that the dark current is much higher in the film obtained by horizontal alloy deposition. In the previous chapter, we showed that the pec response of CZTS layers increases with Zn/Sn ratio, as well as crystal quality of the CZTS material. Here, we compare CZTS layers with Zn/Sn ratio 1.14 and 1.27, obtained from vertically and horizontally deposited precursors, respectively. Even though the latter film is slightly more Zn-rich we observed a doubling in pec current, which cannot be ascribed only to the slight difference in Zn/Sn ratio. We hypothesize therefore that this improvement in pec performance should mostly be ascribed to the tighter initial compositional deviation of the metallic precursor, which in turn leads to better crystallinity and improved kesterite phase purity. A significant dark current is observed mostly in the horizontally deposited samples; this dark current is probably due to a contact between solution and substrate in the presence of pinholes or cracks, forming an electrical shunt. Furthermore, the surface of CZTS layers oxidizes quickly upon annealing, hindering an evaluation of the pec response after low temperature annealing.

VI. Conclusion

CZTS films have been obtained by electrodeposition of Cu-Zn-Sn alloys followed by gas-phase sulfurization. The electrodeposition set-up has been found to have a critical influence on the compositional homogeneity of Cu-Zn-Sn films. The horizontal deposition set-up decreased the compositional standard deviation for each element in comparison with a vertical deposition configuration, particularly for zinc and copper. After sulfurization, the larger spread in composition upon electrodeposition at a vertical electrode leads to the formation of secondary phases. In contrast, growth at a horizontal electrode followed by sulfurization avoids growth of secondary phases, but the adhesion of hydrogen bubbles at the electrode leads to pinhole formation and limits somewhat the morphological homogeneity of the metallic precursor. CZTS films grown by vertical deposition show prominent Cu_xS_y phases and regions exhibiting relatively high copper and zinc deviation. X-ray diffraction showed the formation of Cu_xS_y and $Cu_xSn_yS_z$ secondary phases, which were not detected by Raman spectroscopy. This suggests that the bulk volume of the films may contain more secondary phases than those at the surface. The photoelectrochemical response from the horizontally grown films is higher and correlates with the improvement of phase purity and crystal quality. The optimum annealing temperature to minimize anti-site defects is observed at 175°C for the CZTS layers formed via sulfurization of horizontally deposited metallic precursors; these films also show high crystallinity.

Chapter 6-Incorporation of Bismuth into Cu-Zn-Sn Precursors by Electrodeposition for Bi Containing CZTS Layers

I. Introduction

It is well understood that the crystallographic properties of polycrystalline absorber layers, such as CZTS and CIGS, are important for the solar cell efficiency[154–157]. One way to improve the crystallinity of semiconductor layers is to use a suitable element to enhance the grain growth of the CZTS layers[155, 156, 158]. **Table 6.1** shows some of the common elements, which has been shown to act as fluxing/surfactant as growth modifier; some of these elements in addition are also acting as dopants for CZTS and CIGS polycrystalline films if they are incorporated in the growing films. Therefore, judicious addition of an element to the quaternary CZTS semiconductor may improve the morphology as well as the electronic properties of the bulk material.

Table 6.1 Some of the doping elements for CZTS and CIGS materials

Element	Influence on morphology, and crystallography	Solar Cell Performance	References
Sodium (CZTS and CIGS)	Enhance grain growth and (112) orientation	Optimum amount Increases the efficiency (Voc and FF increase)	[154, 157, 159]
Potassium (CZTS and CIGS)	Enhance grain growth and (112) orientation	Optimum amount increases the efficiency	[43, 155, 159]
Cesium (CZTS and CIGS)	Enhance grain growth and preferred orientation	Increases efficiency	[158, 160]
Antimony (CZTS and CIGS)	Enhance grain growth	Voc and Jsc increase	[156, 161]
Bismuth (CZTS and CIGS)	Enhance grain growth	Optimum amount increases the efficiency or photo-sensivity	[162–164]
Rubidium (CZTS and CIGS)	Enhance grain growth and (112) orientation	Increase in solar cell efficiency	[154, 158, 160]

Bismuth has been shown to work as a fluxing element, although it has been studied only to a limited extent for CZTS or CIGS materials[162–164]. These studies are in agreement on the occurrence of a growth modifier role of Bi with regard to CZTS and CIGS crystal growth; however the influence of bismuth on the preferred orientation of the crystals, its role as a dopant element or the reasons behind the improvement of the efficiency are not clear. More studies are required to understand the influence of the promising fluxing and/or doping element Bi on the polycrystalline CZTS material.

To the best of our knowledge, the electrodeposition of Cu-Zn-Sn-Bi (CZTB) metallic precursors to form Bi containing CZTS (CZTS-Bi) absorber layers has not yet been studied. In this set of experiments, our first aim is to electrodeposit suitable CZTB metallic precursors from a single deposition bath to synthesize CZTS-Bi via sulfurization. Second, we would like to investigate the crystallographic features of the resulting CZTS-Bi layers to inspect the doping role of Bi. Lastly, we seek to understand the correlation between pec performance and crystallographic properties of CZTS-Bi layers. To this end, we first incorporated small amounts of bismuth into CZT by electrodeposition. Successively, we sulfurized CZTB metallic precursors at 500 °C in Ar atmosphere for 1 hour. Composition was determined by EDS and structural properties were analyzed with XRD and Raman Spectroscopy. Finally, we compared the pec response of CZTS layers with and without Bi.

II. Electrodeposition of Bismuth-Containing Cu-Zn-Sn Alloy (CZTB)

Electrodeposition of CZTB was carried out using a similar recipe to the CZT electrolyte reported in Chapter 3 to obtain Cu-poor and Zn-rich precursors **Figure 6.1** shows the cyclic voltammetry of the bismuth electrolyte, the CZT electrolyte, and the CZTB electrolyte. The cyclic voltammetry was run at 10mV/s starting 50 mV anodic of the open circuit potential (~ -0.2 V), first in the cathodic direction down to -2.25 V and then anodic. The bismuth electrolyte (black curve) exhibits a cathodic peak at around -0.63 V for the reduction of bismuth and a sharp current increase at potentials more negative than -0.94 V due to HER. The CZT electrolyte (red curve) shows the first cathodic peak at around -0.5 V for the reduction of copper and the second peak at around - 1.04 V for the reduction of tin; the HER starts at -1.17 V, slightly more negative than the bismuth only electrolyte. The CZTB electrolyte (blue) in the cathodic region shows a behavior similar to the CZT solution. The current begins to increase at -0.45 V where copper reduction starts and reduction of Bi was seen around -0.69 V. The second cathodic peak is observed at -1.31 V and HER at potentials more negative than -1.39 V. The reduction peaks in the CZTB electrolyte take place at more negative potentials than the CZT electrolyte. The cyclic voltammetry studies show that the addition of bismuth slows the rate of the HER in comparison to the CZT electrolyte. This difference is particularly important in the potential range between -1.9 V and -2.2 V, where the precursor is formed.

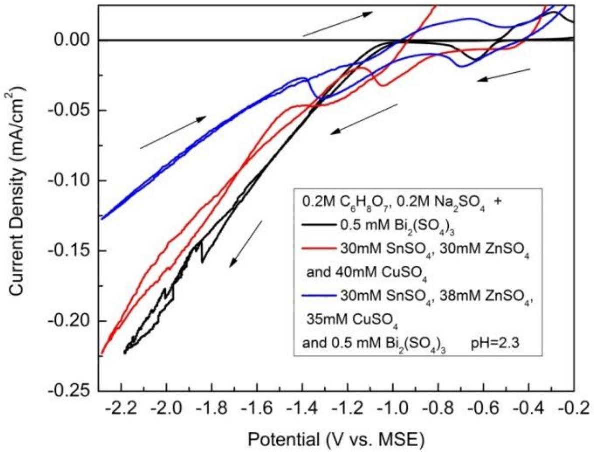

Figure 6.1 Cyclic voltammetry of Bismuth, Cu-Zn-Sn(CZT) and Cu-Zn-Sn-Bi (CZTB) electrolytes with 10mV/s scan rate.

Figure 6.2 shows the elemental fraction of CZTB deposited from an electrolyte containing 30 mM $SnS0_4$, 30 mM $ZnSO_4$, 37 mM $CuSO_4$ and 2 mM $Bi_2(SO_4)_3$ at pH 2.3. The fraction of copper decreased and zinc increased with more negative potentials, whereas bismuth stayed around 4 at % within this potential range. The amount of tin decreased between -1.7 V and -2.1 V and slightly increased between -2.1 V and -2.3 V. The targeted off-stoichiometric composition, Zn-rich and Cu-poor, was obtained at -2.2 V and -2.3V. We modified the electrolyte recipe slightly for the CZTB solutions with 0.5 mM and 1 mM $Bi_2(SO_4)_3$ to obtain similar composition between -2.1 V and -2.3 V.

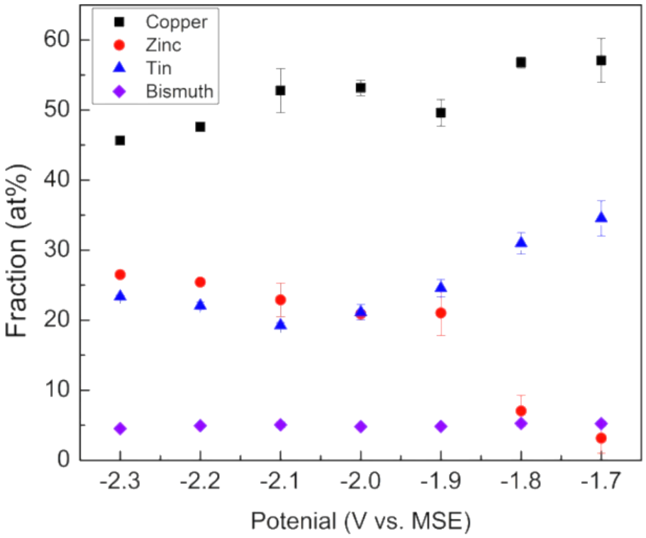

Figure 6.2 Compositional trends of Cu-Zn-Sn-Bi metallic precursors

The Cu-poor metallic CZTB precursors with ~ 1 at% Bi have also been grown with different Zn/Sn ratios. **Table 6.2** shows representative compositions for CZTB metallic precursors layers electrodeposited from an electrolyte containing 30 mM $SnS0_4$, 38 mM $ZnSO_4$, 35 mM $CuSO_4$ and 0.5 mM $Bi_2(SO_4)_3$.

Table 6.2 Fraction of CZTB metallic precursors deposited from a CZTB electrolyte with 0.5mM $Bi_2(SO_4)_3$

Potential (V)	Cu (at%)	Zn (at%)	Sn (at%)	Bi (at%)	Zn/Sn
-2.2	48.4±2.0	24.1 ±2.8	26.7±1.0	0.8±0.2	0.9
-2.3	45.5±1.7	27.2±0.9	26.2±1.8	1.1±0.2	1.04

The corresponding SEM images for these selected CZTB precursors are shown in **Figure 6.3**. Limited dendrite like formations is observed for both layers. The films are continuous with some cracks at the surface.

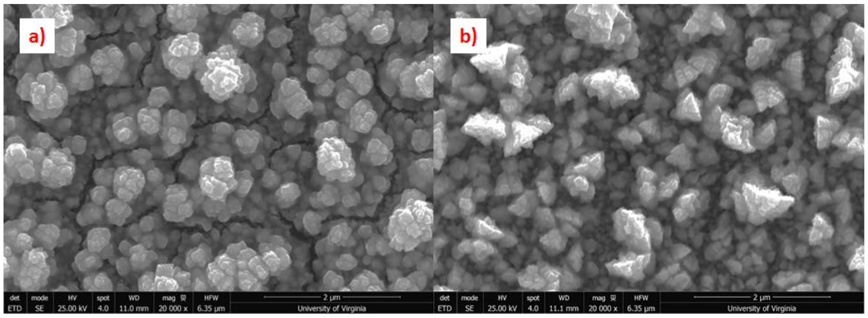

Figure 6.3 SEM images of as-deposited CZTB metallic precursors a) Zn/Sn= 0.90 and b) Zn/Sn= 1.04

III. Structural Characterization of Bismuth Containing CZTS Films

Structural properties of CZTS-Bi films are first inspected with XRD after sulfurization. The compositional values for these layers are shown in **Table 6.3**. The fraction of copper and bismuth for the two samples are close; however, the sulfur amount is slightly different for these layers. The Sn-rich precursors lost some Zn while the Zn-rich precursors showed Sn loss after sulfurization.

Table 6.3 Elemental Fraction of CZTS-Bi layers after sulfurization

Potential (V)	Cu (at%)	Zn (at%)	Sn (at%)	Bi (at%)	S (at%)	Zn/Sn
-2.2	20.1±0.5	9.0±0.6	11.1±0.4	0.4±0.1	59.2±0.8	0.81
-2.3	21.2±0.4	13.9±0.5	12.2±0.5	0.4±0.1	52.4±0.6	1.14

Figure 6.4 shows the XRD patterns for Zn-rich and Sn-rich CZTS-Bi layers. CZTS phase is observed for both of these layers, with small superstructure peaks at around 18, 36 and 38 degrees. However, Sn-rich layers present CTS ternary compound as well as SnS_2 binary phase. Besides that, we detected another peak at around 27 degrees either for Cu_xS_y or ZnS secondary phases.

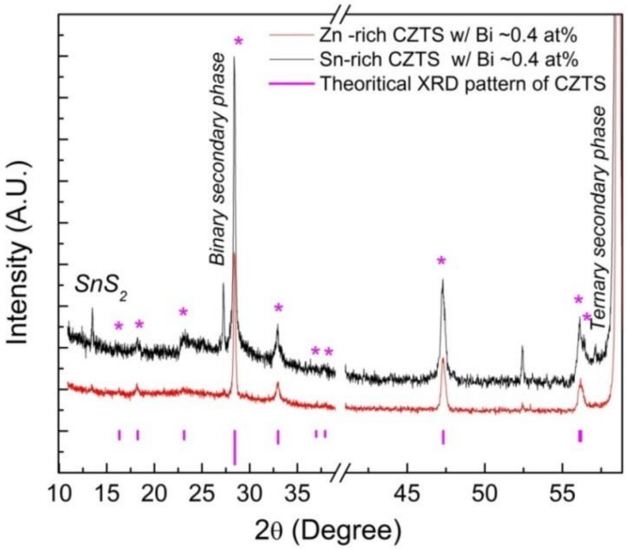

Figure 6.4X-ray diffraction patterns of Zn-rich and Sn-rich CZTS-Bi layers

To investigate Bi doping into CZTS we analyzed the XRD patterns of relatively pure Zn-rich CZTS with and without bismuth. The FWHM of the CZTS-Bi layers is decreased with the addition of bismuth, which suggests an improvement of crystallinity. We also observed an increase of the relative intensity of the preferred (112) plane for the CZTS-Bi layers comparing to CZTS films without doping. These results are similar to the studies of Chen et al for Bi containing CIGS and with the study of Rawat et al. for the Bi containing CZTS layers[164, 165].

Table 6.4 Crystal and lattice parameters from X-ray diffraction patterns for Zn-rich CZTS layers with and without Bi

Material	FWHM $_{(112)}$ (°)	FWHM $_{(220)}$ (°)	$I_{(112)}/I_{(220)}$	a (Å)	c (Å)	D (nm)
CZTS w/o Bi	0.46	0.52	1.99	5.39	10.70	31.13
CZTS w/ Bi	0.20	0.25	2.73	5.42	10.85	71.59

Table 6.4 shows the parameters we calculated from XRD patterns for Zn-rich CZTS layers with and without bismuth. The addition of Bi increased the lattice parameters, hence increased the lattice volume due to the introduction of relatively big size atom bismuth. The atomic size of the Bi is closest to Sn atoms in comparison with Cu and Zn [166]. It is possible that Bi may take the place of Sn atoms; however a more detailed study is required to understand the substitution of Bi into CZTS lattice. The size of the crystalline grains increased almost twice with the addition of a small amount of Bi (0.4 at%).

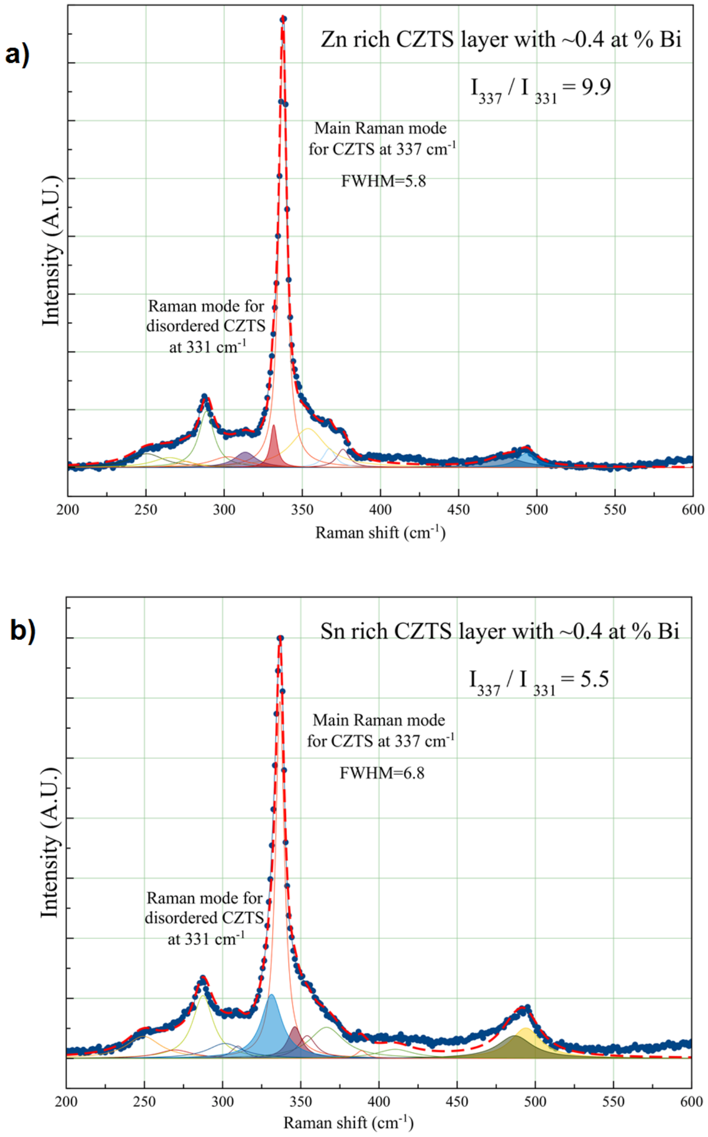

Figure 6.5 Raman Spectra of Sn-rich and Zn-rich CZTS-Bi layer with 514 nm excitation wavelength

Next we compare the Raman Spectra of the Zn-rich and Sn-rich CZTS layers using λ = 514 nm (**Figure 6.5**). According to the investigations of the main Raman mode for the kesterite phase, the Zn-rich CZTS-Bi has better crystallinity comparing to the Sn-rich CZTS-Bi layer. The FWHM of the films are 5.8 cm^{-1} for Zn-rich layer and 6.8 cm^{-1} for Sn-rich layers, suggesting the better crystallinity of the Zn-rich one. The Lorentzian fitting also shows that the intensity of disordered type kesterite is higher for the Sn-rich layer than the Zn-rich one. Even though we did not observe a SnS_2 phase by XRD, we observed this phase for the Zn-rich CZTS-Bi at around 314 cm^{-1} with Raman Spectroscopy. This suggested that the SnS_2 phase for the Zn-rich CZTS-Bi is only present at the surface of the film, but not in the bulk region of the material. In addition, we detected some peaks for Cu_xS_y phases between 470 cm^{-1} and 495 cm^{-1}. Analysis of the overall spectra also suggests that the phase purity of the Zn-rich layer is better than the Sn-rich layer.

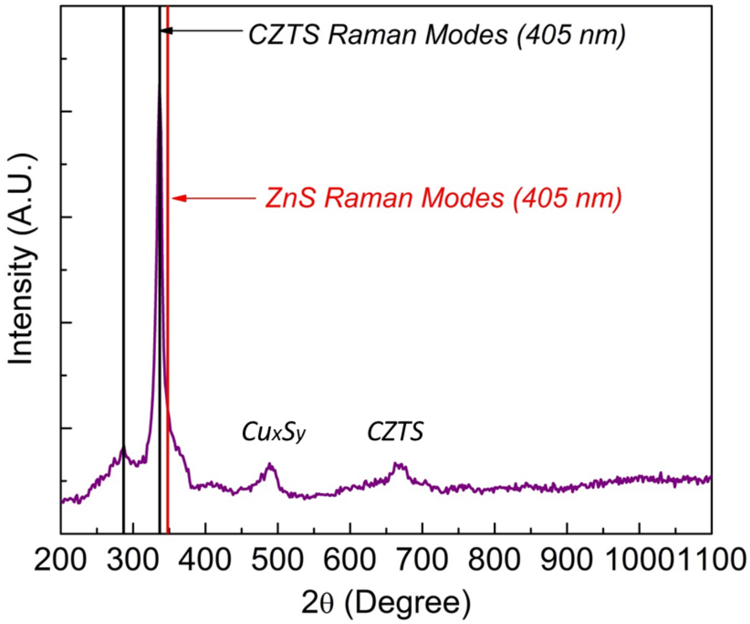

Figure 6.6 Raman spectra of CZTS-Bi with 0.5 at% Bi , 405 nm excitation wavelength

Figure 6.6 shows the Raman spectra of Zn-rich CZTS-Bi layers with the 405 nm excitation wavelength for the detection of ZnS phase. The investigation of ZnS phase is based on the second order Raman scattering mode of the ZnS Raman mode at around 694 cm^{-1}. According to our analysis we did not detect this peak. This suggests that the Zn-rich CZTS-Bi layer contains negligible amount of ZnS phase at the surface of the film. CZTS-Bi layer contains less ZnS than the CZTS layers with similar compositional values. Tong et al. also reported the inhibition of the ZnS formation after the addition of bismuth, which is in consistent with our findings[163].

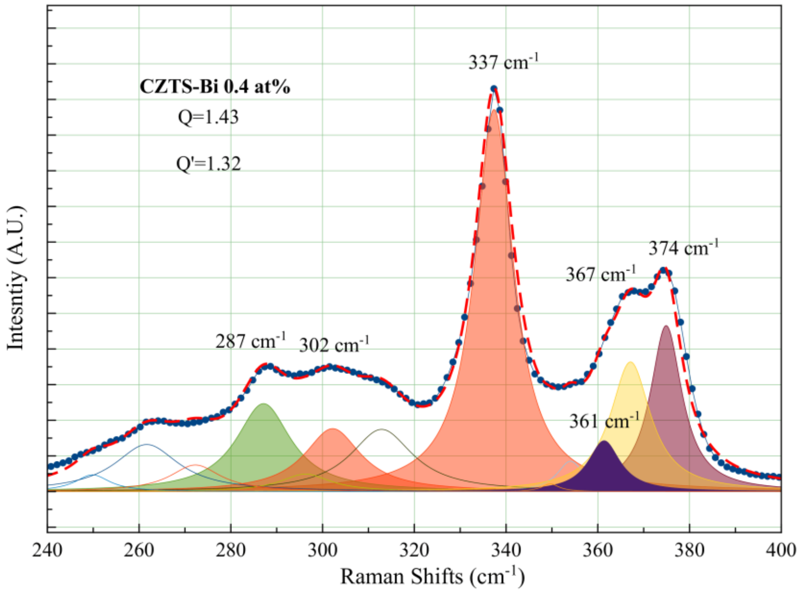

Figure 6.7 Raman Spectra of Zn-rich CZTS-Bi layer with 785 nm excitation wavelength

For further investigation of the crystallographic properties of CZTS-Bi layer, we analyzed the Raman modes with 785 nm excitation wavelength (**Figure 6.7**) and compared the Raman spectra data with CZTS without Bi addition (**Table 6.5**). We compared two layers with relatively close ZN/Sn ratios; the Zn/Sn ratio of CZTS-Bi layer was 1.17 and that of the CZTS layer was 1.01. The Q value for CZTS-Bi is almost threefold higher than that of the CZTS only, suggesting better chemical order of Cu-Zn atoms for CZTS-Bi layers. We also detected a mode around 361 cm^{-1}, which is attributed to one of the CZTS modes[167–169]; however we did not observed this peak for our previous experiments with CZTS only layer.

Table 6.5 Comparison of Zn-rich CZTS layers with and without Bismuth

Raman S. Excitation Wavelength (nm)	785	785	514	514
CZTS Film	Q	Q'	Q''	$FWHM_{337}$ (cm^{-1})
Without Bismuth	0.48	0.82	7.22	6.2
With Bismuth	1.43	1.32	9.9	5.8

Furthermore, we observed more than 50% increase in the Q' value; such a significant change has not been detected yet for other comparative studies in this dissertation. The changes in the Q' values are related to the possible band gap modification due to the changes in the cation order[102, 170]. The Q' equation depends on the Raman modes at 337 cm^{-1} (A mode), 366 cm^{-1} (E mode) and 374 cm^{-1} (B mode). Since changes in the E mode and B mode are related to the displacements along a and c, respectively[100, 101, 171], the distinctive change of Q' may be attributed to the incorporation of Bi atom in the CZTS lattice. Raman investigations with $\lambda = 514$ nm also show the presence of a higher fraction of ordered type kesterite in CZTS-Bi film, according to the Q' values and the narrower FWHM values, suggesting higher crystallinity.

VI. Morphological Investigation of the CZTS-Bi Layers

SEM images of Bi-containing CZTS layers are shown in **Figure 6.8**. Sn-rich and Zn-rich CZTS-Bi layers have similar morphology and grain features. Note however that XRD shows a doubling in grain size, suggesting that the SEM provides only an apparent gran size. Sn-rich CZTS-Bi contains hexagonal features over the CZTS layers. The EDS compositional mapping for the Sn-rich CZTS-Bi layers is shown in **Figure 6.9**. The elemental mapping for copper shows high intensity signals in correspondence of these hexagonal features, which suggest the presence of a Cu-rich secondary phase in Sn-rich CZTS-Bi layers. Even though we also observed in the Raman spectra Cu-rich secondary phases in the Zn-rich CZTS-Bi, we did not observe these hexagonal features in the latter films.

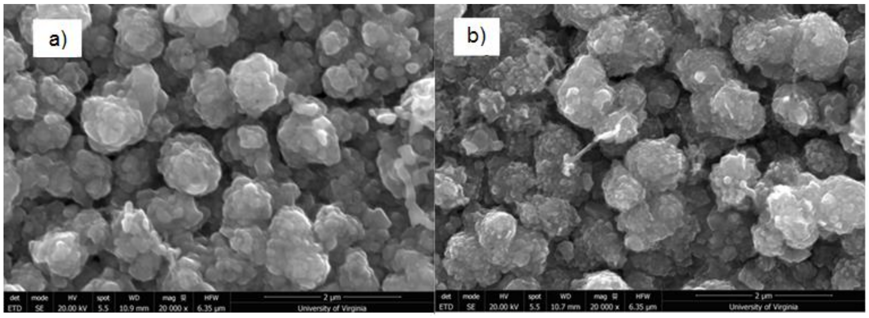

Figure 6.8 Top down SEM images of a) CZTS-Bi with Zn/Sn 0.80 and b) CZTS-Bi with Zn/Sn 1.17

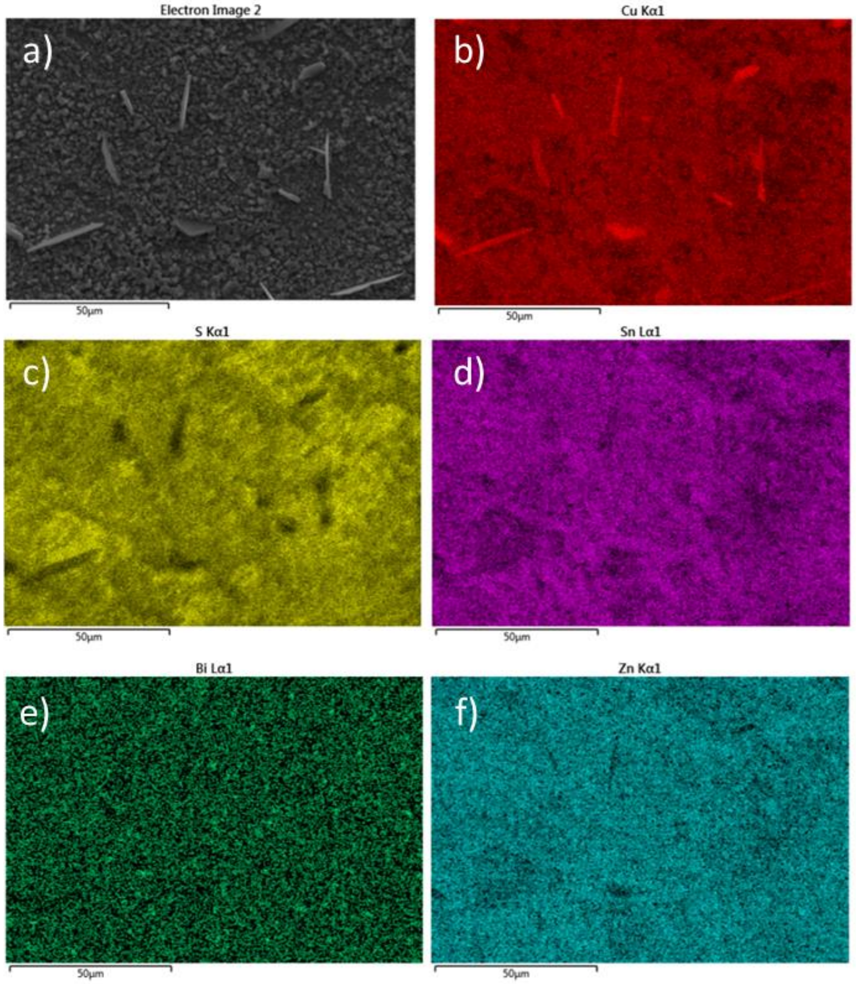

Figure 6.9 EDS compositional mapping of Sn-rich layer CZTS-Bi with Zn/Sn 0.8, color code; red for copper, yellow for sulfur, pink for tin, green for bismuth and blue for zinc.

In other experiments, we also synthesized CZTS layers with 1 at% and 2 at % of bismuth. The EDS compositional mapping suggests Bi-rich secondary phases (**Figure 6.10**). These features are probably Bi_2S_3 phases coexisting with the CZTS phase. Since excess bismuth species did not incorporate into the CZTS phase, we only focused on CZTS films with about 0.5 at% Bi or less for the Bi doping studies.

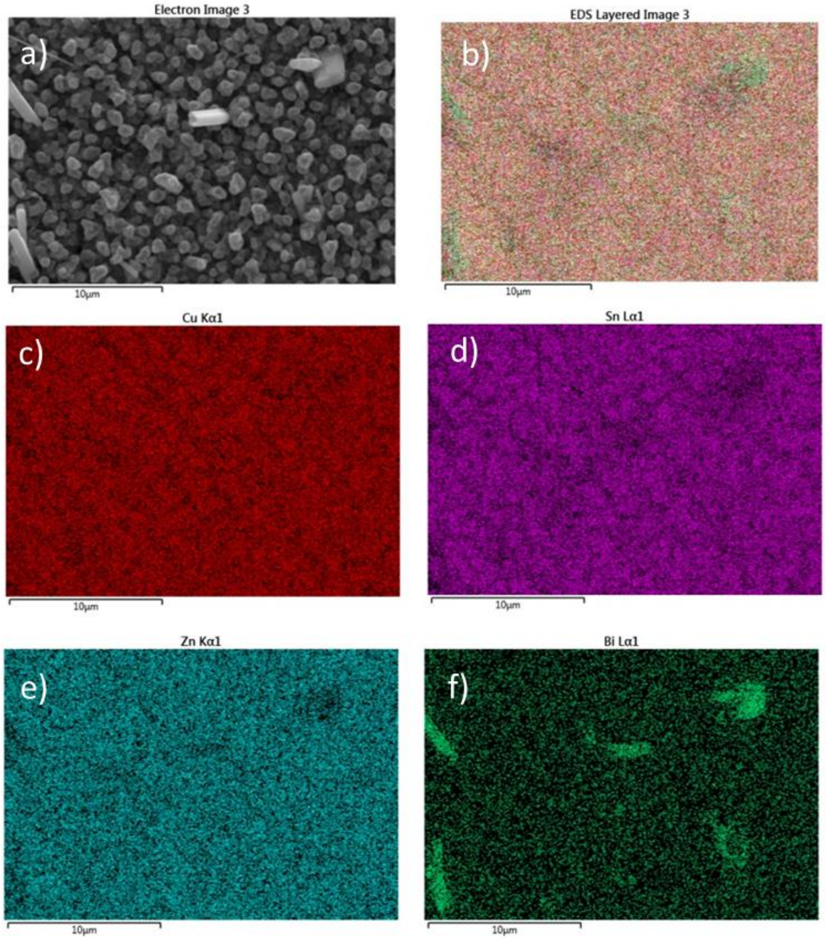

Figure 6.10 EDS mapping of CZTS-Bi layer (2 at% Bi) with Bi-rich secondary phases color code; red for copper, pink for tin, green for bismuth and blue for zinc.

V. PEC Performance of CZTS-Bi Layers

The PEC performance of the Bi-containing CZTS absorber layers is shown in **Figure 6.11**. All the films in this set of CZTS-Bi samples contain ~0.4 at% of bismuth, but with different Zn/Sn ratios, i.e. 0.8, 0.92 and 1.17. CZTS-Bi samples with 1 at% and 2 at% Bi present a negligible level of PEC response; therefore we did not present data for layers with more than 0.7 at% Bi. All layers containing about 0.4 at% Bi show increased photocurrent in the cathodic region suggesting p-type conductivity. In addition, the photoresponse of the CZTS-Bi layers increased with the increasing amount of Zn/Sn ratio, similar to the behavior of CZTS samples, as shown in Chapter 4.

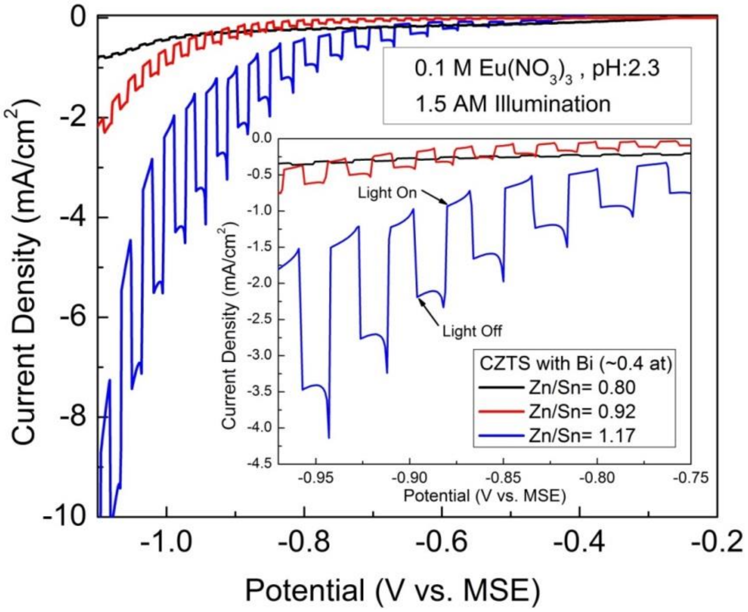

Figure 6.11 Pec responses of CZTS-Bi layers with Zn/Sn ratio 0.80, 0.92 and 1.17

The highest PEC response, 2.65 mA/cm^2, is observed for CZTS-Bi with Zn/Sn ratio 1.17 at around potential -0.95 V. The significant level of dark current is probably due to crack formation in the films. The Sn-rich layers in contrast show a relatively low PEC response than the Zn-rich layer. On the other hand, the dark current is close to zero even with a significant presence of conductive surface secondary phases such as Cu_xS_y[55]. While these conductive phases may not form a continuous path inside the material, this finding may suggest that the dark current could mostly be due to pinholes and gaps in the layer, besides surface phases coexisting with the primary phase CZTS-Bi.

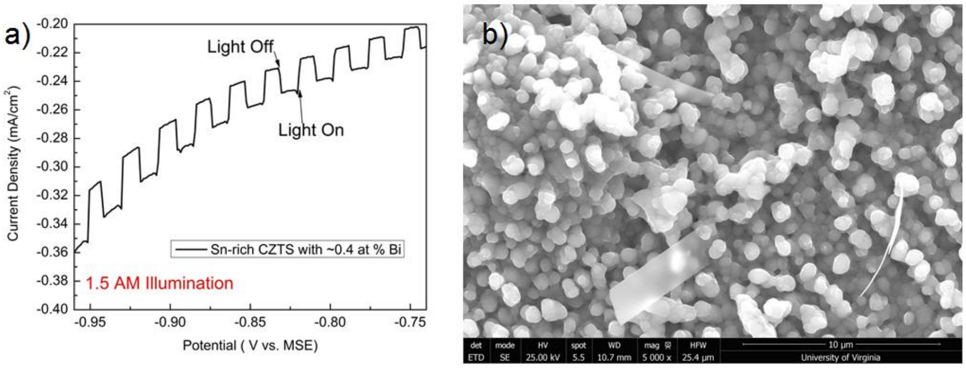

Figure 6.12 a) Pec response of Sn-rich CZTS-Bi layer with Zn/Sn 0.80 and b) top down SEM image of this layer

The lowest PEC response is observed with the CZTS-Bi containing the highest Sn fraction. The PEC curve for this sample alone is shown in **Figure 6.12.a** and the corresponding SEM image is shown in **Figure 6.12.b**. This layer is seen to contain ribbon like features at the surface; however the EDS compositional mapping did not show any noticeable signal for bismuth or other elements in these ribbons. It is possible that the ribbons are very thin and detection limitations of the EDS compositional mapping mode may hinder detection of the Bi signal.

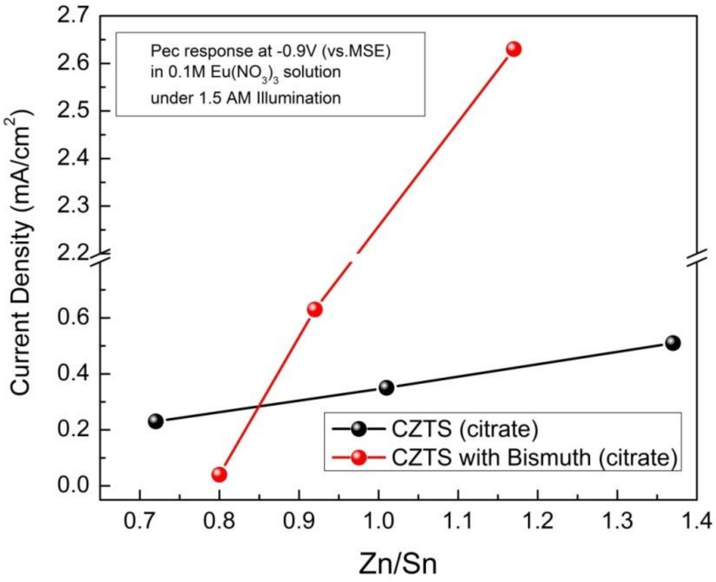

Figure 6.13 Comparison of PEC response of CZTS layers with and without bismuth

Figure 6.13 shows the photoresponse of CZTS only and CZTS-Bi layers as a function of Zn/Sn ratio. Sn-rich CZTS-Bi layer show the lowest photoresponse, whereas Zn-rich CZTS-Bi exhibit the highest PEC response. According to our experiments we found that the PEC response of the CZTS-Bi layers is more sensitive to the Zn/Sn ratio changes in comparison to the undoped CZTS films. The strong dependence of the properties of Bi-containing layers on the Zn/Sn ratio may be due to the formation of additional Bi-rich secondary phases and/or to changes in the defect chemistry.

VI. Conclusion

Bismuth-containing CZTS layers with the target composition (Cu-poor, Zn-rich with respect to the stoichiometric composition) have been obtained by electrodeposition of Cu-Zn-Sn-Bi (Bi ~ 0.5 at%) from a simple citrate based electrolyte, followed by sulfurization. We found that Bi additions do increase the grain size, suggesting that it is acting as a fluxing agent; in addition, the increase in PEC response evidences the additional role of Bi as a dopant for CZTS materials. The CZTS lattice parameters increased slightly and the grain size of the crystals about doubled after the addition of bismuth. The incorporation of Bi into the CZTS lattice is found to be limited to ~0.5 at% Bi, and above this amount we observed Bi-rich secondary phases in the layers. We also investigated the relative amount of disordered type and order type kesterite in the CZTS-Bi layers. Bi-containing CZTS layers show more ordered type kesterite in comparison to CZTS film. The FWHM analyses of films with XRD and Raman spectra are in agreement with regard to the better crystallinity of Bi-containing CZTS films vs. CZTS layers. CZTS-Bi layer also showed the highest PEC response in our studies, with a 2.65 mA/cm^2 photoresponse at -0.95 V. The photoresponse of the CZTS-Bi layers is higher than the CZTS layers for Zn/Sn ratio above 0.90. We attributed the improvement of the PEC performance to two reasons; the increase of the grain size and the improvement of the chemical order of the CZTS lattice, which influences the electronic structure of the CZTS. However, further investigations are needed to determine what type of defects Bi generates in the lattice, and why the CZTS-Bi layers PEC results are strongly dependent on the Zn/Sn ratio.

Chapter 7-Solar Cell Performance of CZTS Based Absorber Layers

In this chapter, we investigate the electrical and optical properties of the CZTS based absorber materials and the solar cell performance of CZTS based solar cells. For this purpose, we first synthesized CZT metallic precursors with ~2 cm^2 size (necessary to test solar cells with the available instrumentation) and sulfurized them to form CZTS layers. Successively we investigated the power conversion efficiency (pce) of the devices through current density-voltage measurements. We found a correlation between compositional distribution of the CZTS films and the cell efficiency and we analyzed the I-V curves to understand the role of compositional trends on the performance parameters of these cells. Second, we inspected the morphological properties of the layers with SEM and EDS mapping to understand the influence of secondary phases and pinholes in the absorber on the solar cell performance. Further investigations on the electrical and optical properties were carried out by measuring the Hall coefficient, and the capacitance-voltage curves to determine the carrier concentration via the Mott-Schottky method. Finally, in order to understand loss mechanisms in the bulk and at the interfaces, we measured the minority carrier lifetime of the CZTS layers with time resolved photoluminescence and the photoresponse by determining the external quantum efficiency (EQE).

I. Current Density-Voltage Characteristics

The manufacturing process for ~2 cm^2 size CZTS based solar cells is presented in **Appendix 3**. In brief, upon sulfurization of CZT layers to form CZTS, we deposited successively the CdS, ZnO and ITO layers as described in **Chapter 2**. The solar cell performance was investigated by current density vs. voltage (I-V) curves for each of the CZTS layers discussed in the following. The full size of the solar cell device was ~ 2.0 cm^2, which however consisted of 9 or 15 smaller subcells, all with the size of 8 mm^2, which could be tested separately via Ni/Al contacts obtained by photolithography and metal deposition.

To investigate the correlation between efficiency and the composition of CZTS layers we examined the subcells of each CZTS based devices. For the sake of clarity, we assigned numbers to each subcell and color-coded in red the subcells with less than 0.1% efficiency (**Figure 7.1.a**). **Figure 7.1.b-d** show the schematic figures for the efficiency of subcells and the compositional trends for each CZTS based device, which had been synthesized via sulfurization of precursors electrodeposited with vertical (CZTS_Citrate and CZTS_Bi) and horizontal (CZTS-Pyro) deposition set-up. Since the top layers ZnO and ITO (Indium tin oxide) contain some of the same elements as the absorber layer, like Zn and Sn, we were unable to analyze the exact composition of individual subcells after building the device. Fortunately, our previous, detailed studies on the compositional analyses of the CZTS films formed via CZT sulfurization with similar composition and absorber layer size provides a reliable compositional trend for the samples under study in this chapter. The highest efficiency (average among all the subcells) of the three samples that have been measured is observed with the CZTS_Citrate based device, which reached 0.27 %; the lowest average efficiency instead is observed with CZTS_Pyro based device, with 0.10 %, which also contains some nonfunctional subcells. Even though all the subcells of the CZTS_Citrate device show that all of its subcells are working, the best subcell efficiency is still only 0.64 %, which is well below the reported efficiencies for CZTS cells grown with similar methods[78].

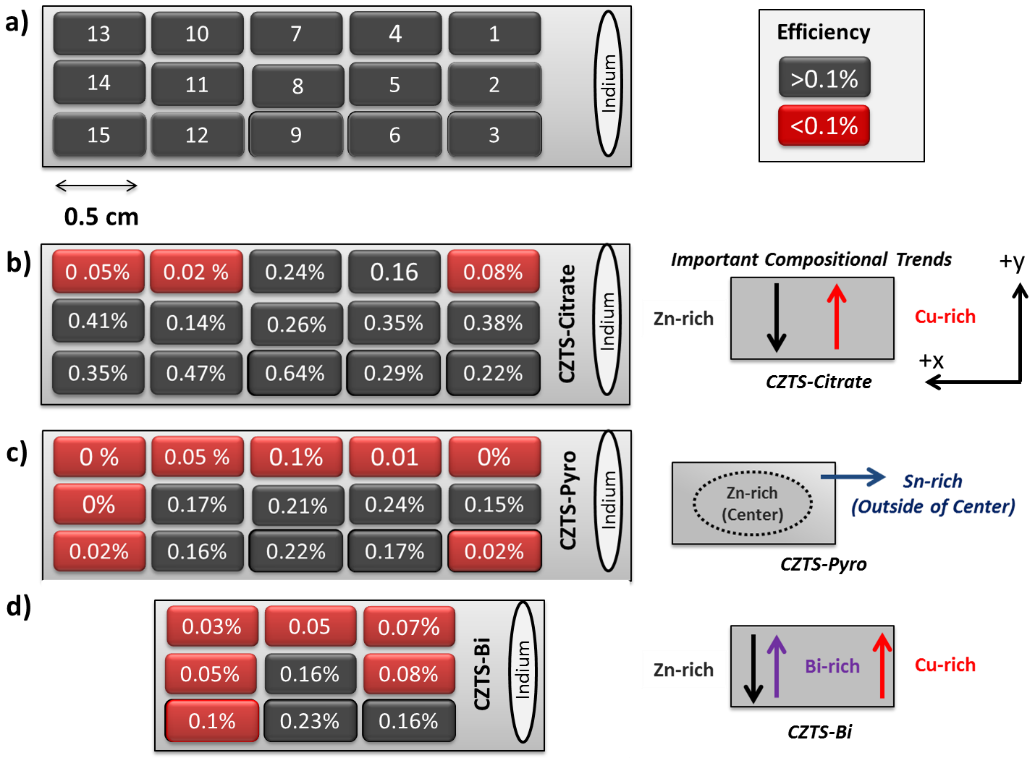

Figure 7.1 a) Schematic of a CZTS based device with numbered subcells, b) efficiency of subcells of a CZTS_Citrate device, c) efficiency of subcells of a CZTS_Pyro device, d) efficiency of subcells of a CZTS_Bismuth device and their corresponding compositional trends.

We investigated the correlation between the solar cell efficiency and the compositional trends of the subcells for each CZTS absorber layer based device (**Figure 7.1**). Based on previous studies in Chapter 4 and Chapter 5, the degree of compositional homogeneity for each CZTS based solar device was determined during the electrodeposition of metallic precursors. The standard deviation for the CZT precursors and the CZTS films are shown in **Appendix 3**. Since we increased the size of the precursors, the standard deviation of these films did increase from 0.2-1.7 at% to 0.9-3.5 at% for CZT_Citrate, from 0.5-0.7 at% to 1.4-3.6 at% for CZT-Pyro, but CZTB precursors maintained the same standard deviation ~0.9-1.7 at%. The CZTS-Citrate and CZTS-Bi layers show an increasing Cu fraction along the y positive direction, corresponding to a higher position during electrodeposition, and an increasing Zn fraction along the negative y direction, i.e. the lower position during electrodeposition. CZTS-Bi layers also exhibit an increased Bi fraction in the positive y direction. All these precursor layers are electrodeposited in a vertical deposition set up, which leads to turbulence and flow instability, resulting in an inhomogeneous current distribution, particularly in the y direction. Even though the standard deviation of the elements is between 0.9 and 3.5 at% for the CZT-Citrate precursors, we found a clear efficiency trend for a ~ 2.25 cm^2 size metallic precursor: the Cu rich regions have lower efficiencies than the Zn-rich region. We observed a similar trend for the CZTS-Bi layer subcells; however this device was also sensitive to the amount of Bi across the layer. Bi-rich subcells (>0.6 at%) show low efficiencies comparing to subcells with moderate Bi fraction (0.4-0.5 at%). CZTS-Pyro subcells also show a correlation between composition and efficiency, but this trend is different from that of CZTS-Citrate or CZTS-Bi layers. This is probably due to the fact that CZT-Pyro precursors are electrodeposited in a horizontal deposition set up as described in **Chapter 5**. The central region of the device is found to be Zn-rich and the outer region is Sn-rich; the Sn-rich subcells at the edges mostly show low efficiency and some non-functional subcells. On the other hand, the Zn-rich central region and some of the relatively Sn-rich regions have better efficiency than the rest of the subcells. The findings above evidence the importance of the composition distribution on the solar cell efficiency even in a small area solar cell.

Three selected I-V curves of each CZTS based solar cell from different regions of the device are reported to understand the influence of compositional trend on the open circuit voltage (V_{oc}), short circuit current (J_{sc}), fill factor (FF), series resistance (R_s) and shunt resistance(R_{sh}). The Cu-rich subcells at the top row had the lowest efficiency of 0.02%, and also the lowest average efficiency of 0.11%. The average efficiency increased to 0.30% in the middle row and the highest average efficiency, 0.39 %, was observed in the Zn-rich bottom row. I-V curves for the selected CZTS_Citrate based subcells, from a Cu-rich top row region (subcell 1), middle row (subcell 5) and Zn-rich bottom row (subcell 9), are shown in **Figure 7.2.** Subcell 1 is relatively Cu-rich and Zn-poor, and has one of the lowest efficiency for this device, partly due to the lowest shunt resistance, which suggests the presence of a highly conductive phase. The efficiency of subcell 5 was 0.35 % due to the increase of Jsc and Voc; however, the series resistance of these subcells increased as well. This suggests the presence of high resistivity phases in subcell 5. The highest short circuit current was measured as 3.87 mA/cm^2 and the largest open circuit voltage was 390 mV for cell 9, which showed also the highest pce with 0.64%. Subcell 9 also had the lowest R_s and the highest R_{sh}, which may be the reason for the relatively high performance. The FF of subcell 9 also is slightly higher than the other subcells, which is consistent with the other I-V curve results.

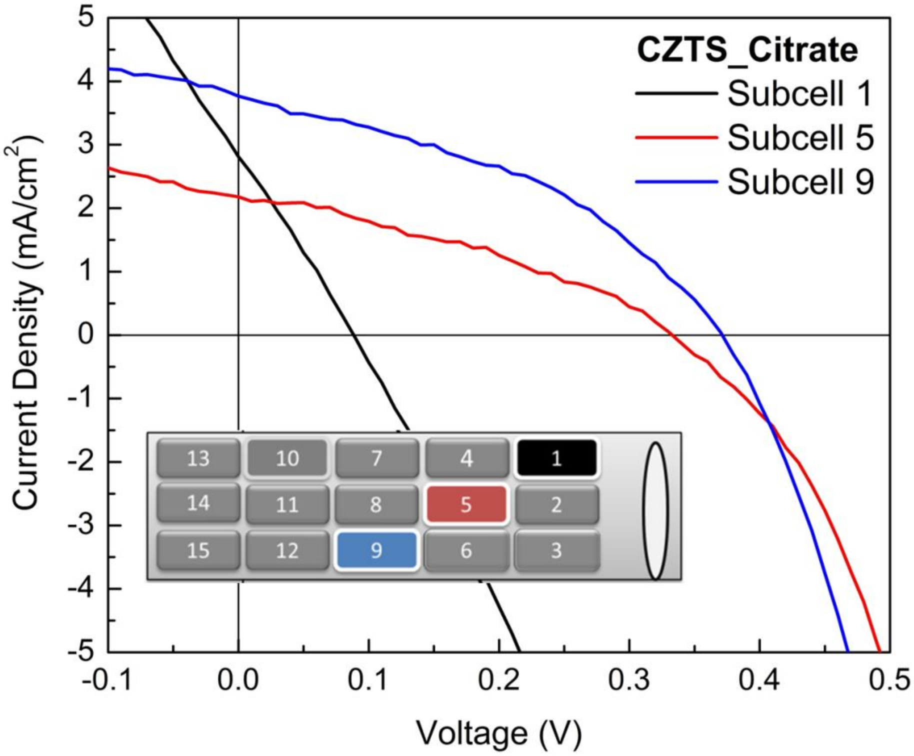

Figure 7.2 Current density and voltage curves of CZTS_Citrate based solar cells

Table 7.1 J-V curve parameters of CZTS_Citrate based Solar Cells

CZTS_Cell Citrate	Jsc (mA/cm^2)	Voc (V)	Jmp (mA/cm^2)	Vmp (V)	FF (%)	η (%)	Rs (Ωcm²)	Rsh (Ωcm²)
Subcell 1	2.52	0.09	1.41	0.06	37	0.08	29.62	36.9
Subcell 5	2.76	0.30	1.82	0.19	42	0.35	57.3	138.3
Subcell 9	3.87	0.39	2.93	0.22	43	0.64	38.3	186.2

I-V curves for the CZTS_Pyro cell collected from a Zn-rich central region and Sn-rich outer regions are shown in **Figure 7.3**. Sn-rich subcells outside of the center region had lower efficiency than the Zn-rich central part. The Sn-rich subcell 10 had the lowest efficiency with low shunt resistance and low Voc. Even though the efficiency of subcell 12 was higher than subcell 10, a very low shunt resistance and low FF of this Sn-rich subcell indicated the presence of metallic like conduction. The observed increase in efficiency is due to the increase in Jsc from a conductive phase. The highest efficiency of this device is observed in the Zn-rich middle region, showing the highest Voc, 220 mV, FF, and Rsh. Even though there is an improvement in the efficiency for subcell 5, the high series resistance suggests low semiconductor quality of the absorber layer.

Table 7.2 J-V curve parameters of CZTS_Citrate based Solar Cells

CZTS_Cell Pyro	Jsc (mA/cm^2)	Voc (V)	Jmp (mA/cm^2)	Vmp (V)	FF (%)	η (%)	Rs (Ωcm²)	Rsh (Ωcm²)
Subcell 10	3.55	0.05	2.76	0.02	31	0.05	14.7	17.3
Subcell 12	9.33	0.07	5.54	0.03	25	0.16	8.2	7.72
Subcell 5	2.31	0.22	1.83	0.13	47	0.24	56.82	102.5

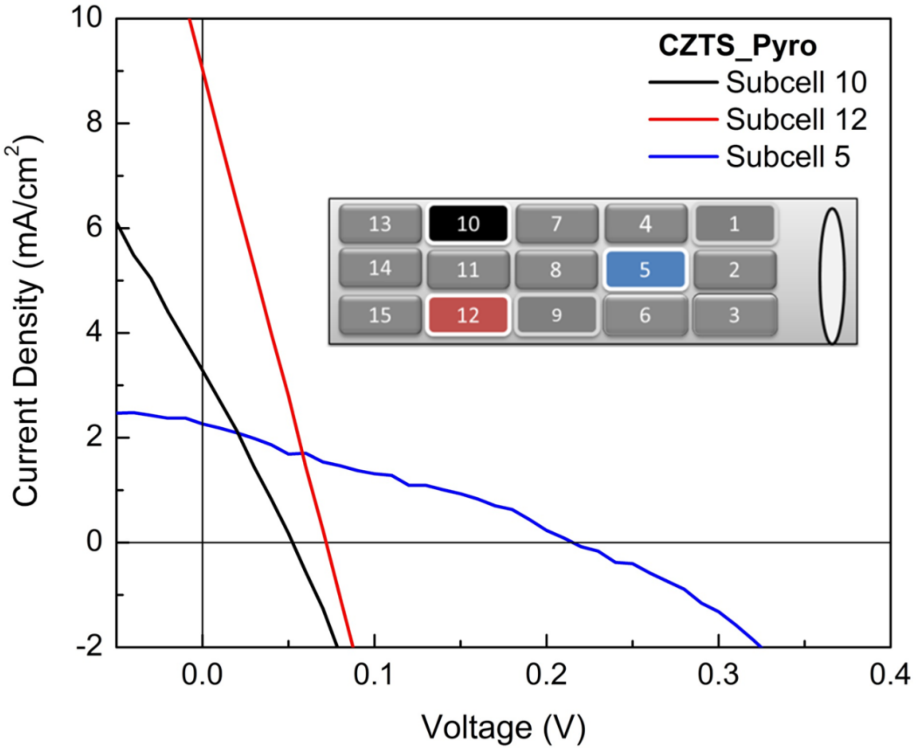

Figure 7.3 Current density and voltage curves of CZTS_Pyro based solar cells

Figure 7.4 shows the J –V curves for a selected CZTS_Bismuth absorber layer based device. Subcell 4 is a relatively Cu-rich layer with 0.8 at% Bi and low efficiency. In our previous experiments, we found that > 0.7 at% Bi is forming Bi-rich secondary phases; therefore the low efficiency of the cells in the top row could be due to the presence of Bi-rich and/or Cu-rich secondary phases. In the middle row, the efficiency of the subcells increased with lower Cu fraction and higher Zn composition. As an example from the middle row, we present the I-V curve of subcell 5, which increased slightly (0.15 %) with the increase of Rsh in the solar cell parameters. The highest average efficiency was observed at the bottom row with the highest efficiency of 0.23 % with subcell 6, showing the highest Voc of 320 mV and the highest Rsh of 272 Ωcm^2. This cell is relatively Zn-rich and contains an optimum amount of bismuth ~0.5 at%, according to our analyses in **Chapter 6**. The increase in Rsh can be related to a lower volume fraction of Cu-rich secondary phases and the lower amount of ZnS in the CZTS-Bi layers, according to Raman spectra analyses shown in **Chapter 6**.

Table 7.3 J-V curve parameters of CZTS_Bismuth based Solar Cells

CZTS_Cell Bismuth	Jsc (mA/cm^2)	Voc (V)	Jmp (mA/cm^2)	Vmp (V)	FF (%)	η (%)	Rs (Ωcm^2)	Rsh (Ωcm^2)
Subcell 4	1.69	0.13	0.90	0.06	25	0.05	71.4	75.4
Subcell 5	2.11	0.25	1.12	0.14	29	0.15	76.92	147.1
Subcell 6	1.98	0.32	1.14	0.20	36	0.23	73.50	272.7

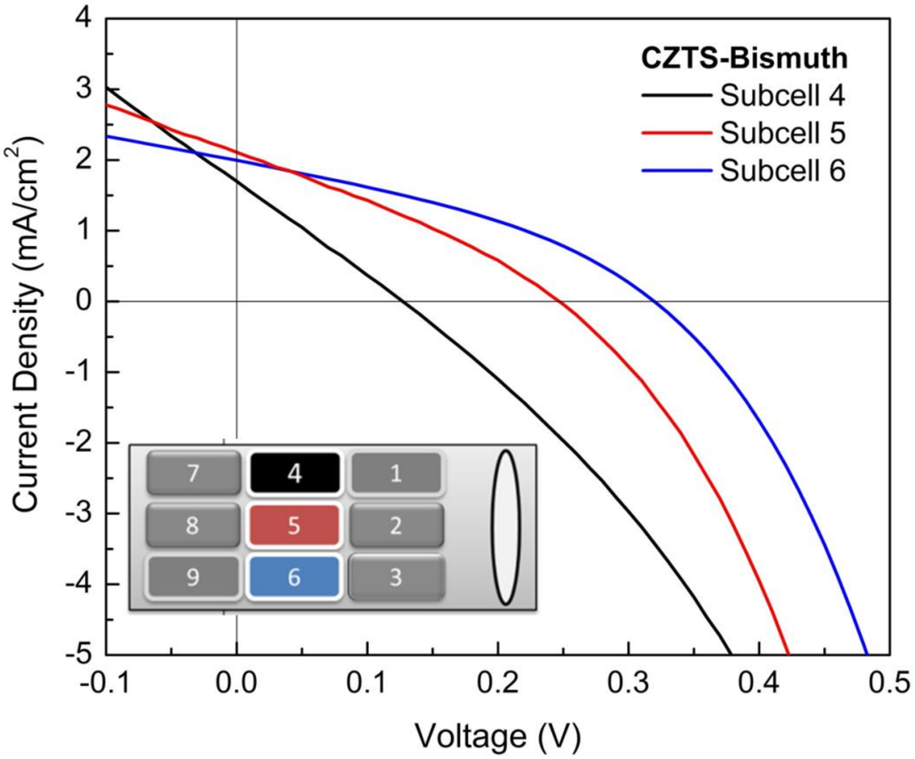

Figure 7.4 Current density and voltage curves of CZTS_Citrate based solar cells

Table 7.4 provides a general comparison of the solar cell parameters measured on our cells with high efficiency CZTS based cells, as reported by Ennaoui et al. [79]. In their study, the authors did grow the CZT metallic alloy from a pyrophosphate based solution and sulfurized to form CZTS layers; the efficiency was 3.6% with 529 mV Voc, 15.9 mA/cm^2 Jsc and 42% FF [78].

Our solar cell parameters are significantly lower than the reported ones, particularly for the Jsc [78, 132, 172–176].

Table 7.14 Comparison of solar cell parameters with relatively high efficiency CZTS from literature

CZTS based cell	Jsc (mA/cm^2)	Voc (V)	FF (%)	η (%)	Rs (Ωcm^2)	Rsh (Ωcm^2)
Literature [78]	15.9	0.53	42	3.60	4.5	243.2
CZTS_Citrate	3.87	0.39	43	0.64	38.3	186.2
CZTS_Pyro	2.31	0.22	47	0.24	56.82	102.5
CZTS_Bismuth	1.98	0.32	36	0.23	73.50	272.7

II. Influence of Secondary Phases on the Performance of CZTS Based Solar Cells

In this section, we focus on the influence of the secondary phases on the solar cell performance. **Figure 7.5** shows the most common secondary phases in CZTS absorber layers. Secondary phases may influence the solar cell performance in different ways, primarily depending on their band gap and band alignment with the primary phase CZTS. XRD analysis showed the presence of Cu_xS_y, SnS_2, SnS and Cu_2SnS_3 phases, and Raman spectroscopy evidences a Cu_xS_y phase (**Appendix 3**). We observed relatively large hexagonal features with SEM images of the CZTS_Pyro and CZTS_Citrate based layers, which were confirmed to be Cu-based phases with the EDS compositional mapping. CZTS_Pyro contains mainly Cu-rich secondary phases (**Figure 7.6.a**) and CZTS_Citrate includes mostly Sn-rich secondary phases (**Figure 7.6.b**). $Cu_{2-x}S$ phase is sufficiently conductive to shunt the solar cell [27, 177]. The hexagonal Sn-rich features may correspond to SnS, SnS_2 or Sn_2S_3 phases, which have different electronic properties and lower band gap than CZTS (**Figure 7.7**); the presence of these phases lower Jsc and Voc, decreasing the solar cell performance[27, 178]. The n-type SnS_2, with a more insulating nature, lowers the efficiency since the mismatch of the band edges is sufficient to generate significant current collection losses (**Figure 7.7**) and also forms a secondary diode in the absorber layer, which lowers the Voc of the cell [27, 178]. We did not detect significant amounts of ZnS phase at the surface of the CZTS films with Raman Spectra analyses. However the observed high series resistance suggests there should be a highly insulating material in the bulk or at the interfaces [27, 52].

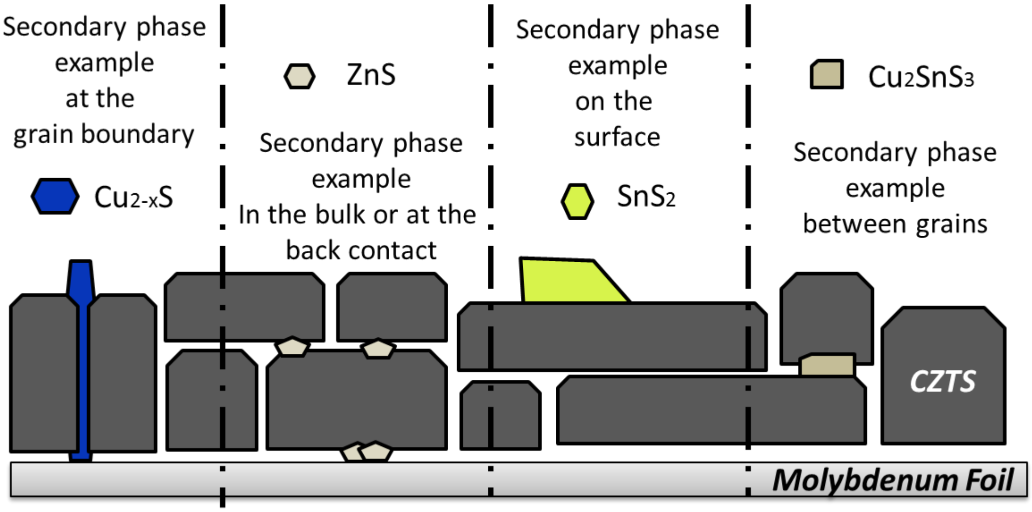

Figure 7.5 The most common secondary phases in CZTS absorber layers

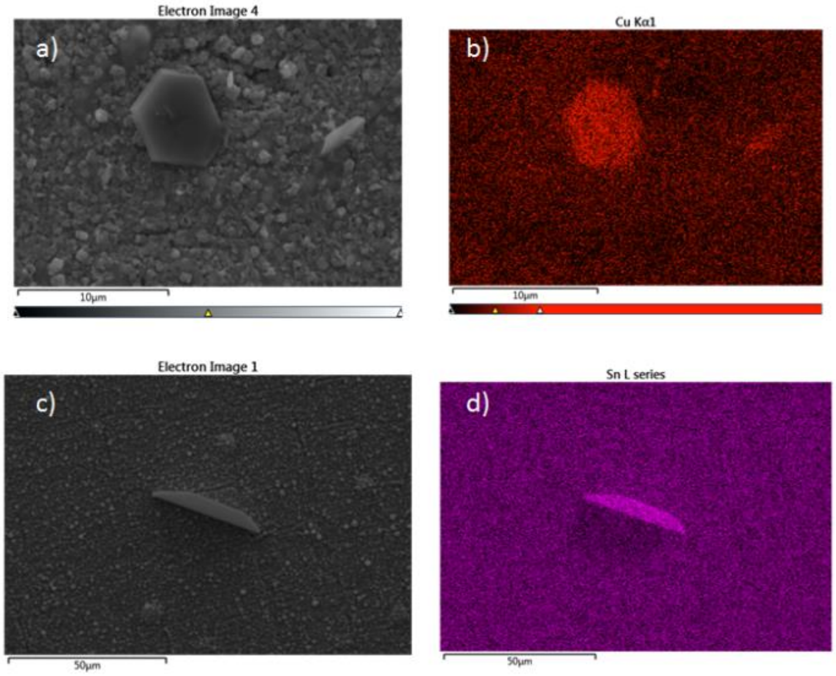

Figure 7.6 SEM image of a) CZTS _Pyro and c) CZTS_Citrate and corresponding EDS compositional mapping of b) copper for CZTS_Pyro and d) tin for CZTS_Citrate

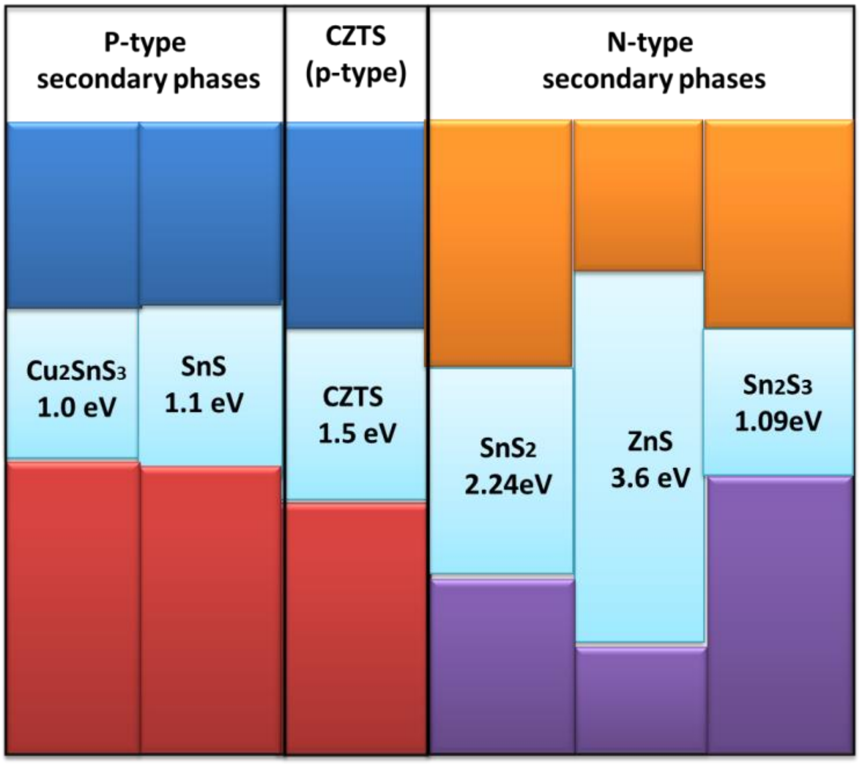

Figure 7.7 Band alignment of CZTS absorber layer and some of the secondary phases [52, 178–180]

We also observed some large pinholes on the complete cells, which we did not observe after deposition of CdS; this suggest that the large pinholes developed after growing the top layers, probably due to accumulation of internal stresses. **Figure 7.8** shows SEM images of ITO/ZnO/CdS/CZTS/Mo layer stacks forming the solar cell; the images show some blisters with cracks (**Figure 7.8.a** and **c**) and some voids, which are probably formed from the blisters after cracking (**Figure 7.8.b** and **d**). These gaps and cracks may also act as shunt paths, thus lowering the Jsc of the cells.

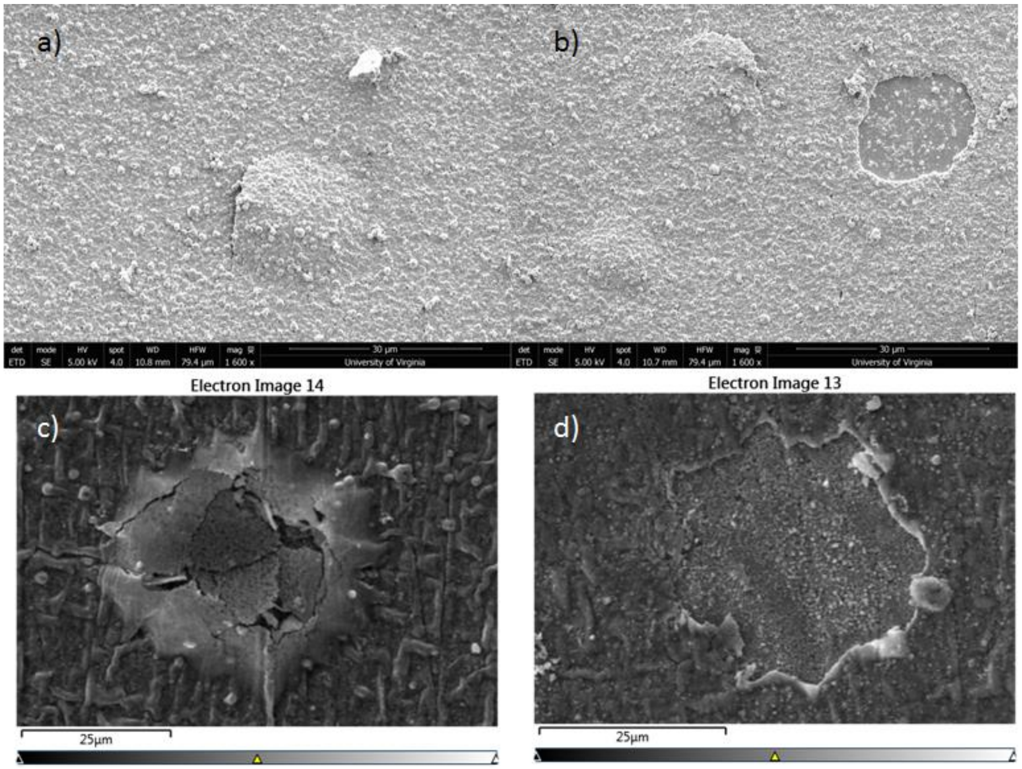

Figure 7.8 SEM images for hole and crack formation a) and b) for ITO/ZnO/CdS/CZTS_Citrate based solar cell and c) and d) for ITO/ZnO/CdS/CZTS_Pyro based solar cell

The back contact side of the CZTS based device, i.e. the interface CZTS/Mo, also contains some secondary phases which cause increase in series resistance and decreases in the shunt resistance. To investigate the phases at the back contact, we removed the ITO/ZnO/CdS/CZTS layer with an adhesive carbon tape and analyzed the remaining film pieces on the Mo substrate with Raman spectra. **Figure 7.9** shows a dominant peak for MoS_2, which coexists with CZTS, Cu_xS_y and SnS at the back contact, all phases being formed during the sulfurization process. The presence of these phases at the back contact is probably the reason for the high series resistance, which lead to low Jsc and Voc.

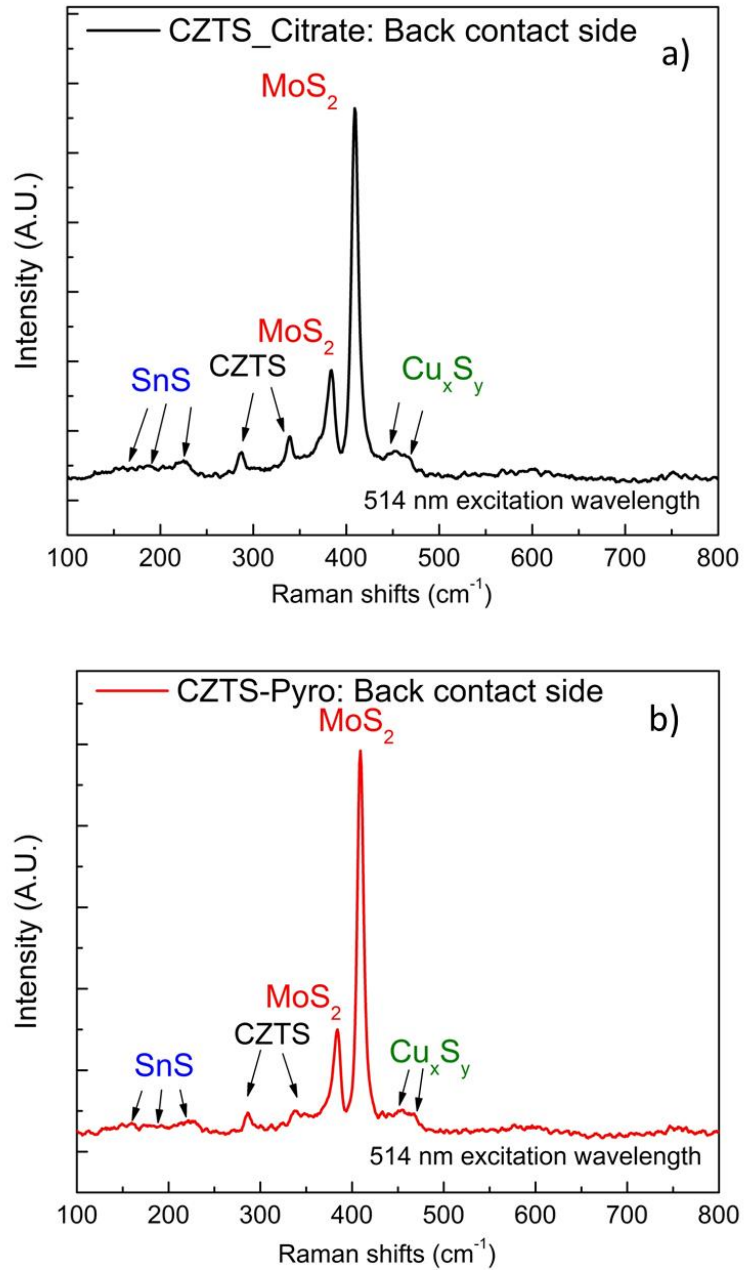

Figure 7.9 Raman spectra of CZTS based layers from back contact side after removal of CZTS layers a) CZTS_Citrate and b) CZTS_Pyro

III. Electrical and Optical Properties of CZTS Based Solar Cells

We investigated the charge carrier concentration of the CZTS_Citrate layers by performing Hall Effect measurements; Ag evaporated through a maskwas used to provide an ohmic contact. **Figure 7.10.a** shows the ohmic contact behavior of the Ag/CZTS as a function of the Zn/Sn ratio; the resistance decreases with increasing Zn/Sn ratio. The carrier concentration and the conductivity of the layers of the CZTS films are shown in **Figure 7.10.b**. The carrier concentration decreased and the conductivity of the layers increased with the increasing Zn/Sn ratio as expected. The carrier concentration was 1.1x 10^{14} cm^{-3} for the CZTS layer with Zn/Sn ratio 0.96. This carrier concentration is slightly lower than values reported in the literature [181–183], probably related to the different composition of the CZTS layers.

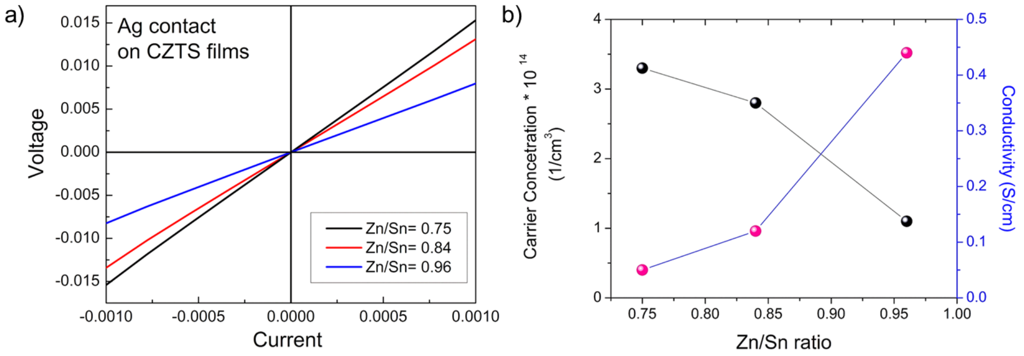

Figure 7.10 a) I-V curve for Ag contact on CZTS_Citrate films and b) carrier concentration and conductivity of CZTS layers with Hall Effect measurements

We also used Mott-Schottky(M-S) measurements to determine the carrier concentration and the flat band potential V_{FB} of the Zn-rich CZTS_Citrate and Zn-rich CZTS_Pyro layers. The M-S plots are shown in **Figure 7.11**. The CZTS layers show p-type conductivity; the carrier concentration of the layers are $4.0*10^{16}$ cm^{-3} and $6.6*10^{15}$ cm^{-3}, respectively. The flat bad potentials are -0.61 (V vs. MSE) and -0.93 (V vs. MSE) for CZTS_Citrate and CZTS_Pyro layers, respectively. The charge carrier concentrations and the flat band potential are close to values reported in the literature [184, 185]. The difference in V_{FB} between the various CZTS layers may cause slightly different band alignment with the CdS layers, which potentially result in performance variations.

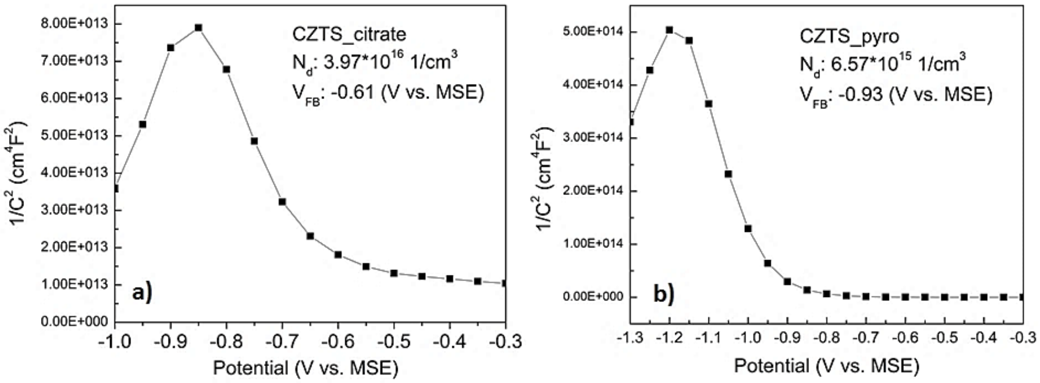

Figure 7.11 Mott-Schottky curves of a) CZTS_Citrate and b) CZTS_Pyro films

Figure 7.12 shows the solid state capacitance voltage (C-V) characteristics for cell 5 of the CZTS_Pyro device. The result shows p-type conductivity with a flat band potential at -0.22 V. The carrier concentration of subcell 5 is 2.0*10^{17} cm^{-3}, which is within the same range as literature values; however, the charge carrier density is slightly higher than the value determined by the M-S method[184, 186]. Note however that the M-S measurements were performed on the absorber layer only, while C-V measurements were performed on the whole CZTS device stack, including the top layers, ITO/ZnO/CdS. The variance between charge carrier densities can be related to differences in the measurement techniques (a surface technique vs. nominally a bulk technique) as well as to the contribution of large pinholes in the CZTS layer, which formed after deposition of the ITO/ZnO layers.

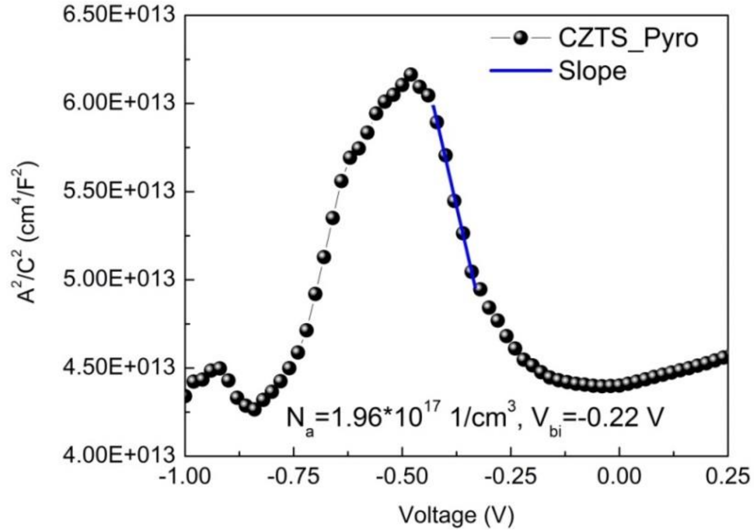

Figure 7.12 Capacitance-Voltage curve for ITO/ZnO/CdS/CZTS_Pyro

Time resolved photoluminescence (TRPL) measurements are used to evaluate the minority carrier lifetime of CZTS_Citrate (subcell 9) and CZTS_Pyro (subcell 5), the best performing ones (**Figure 7.13**). The mean decay time of the CZTS_Citrate absorber layer (1.5 ns) is twice the value of CZTS_Pyro layer (0.7 ns). In the literature, effective minority carrier lifetimes are reported around 0.2-5 ns for kesterite based solar cells [187, 188]. The first decay time τ_1 , which is attributed to the charge separation time, is 0.5 ns for both samples [189]. The second decay time τ_2 is slightly higher for CZTS_Citrate than CZTS_Pyro. τ_2 is attributed to the various recombination losses, due to scattering at grain boundaries, deep defects in the grains, and losses at the CZTS/Mo interface [189]. Our Raman spectra analyses performed at the back of the CZTS layers (**Figure 7.9**) show similar phases for CZTS_Citrate and CZTS_Pyro layers. Therefore, the relatively shorter lifetime results of CZTS_Pyro layer are probably originated by losses in the bulk. The bilayer nature of CZTS_Pyro, seen in cross sectional SEM images (**Figure A3.3**) may be one of the reasons besides other bulk related losses. However, both samples show relatively short lifetimes, which suggest the presence of a high density of recombination centers within the bulk of the absorber layers and at the back contact.

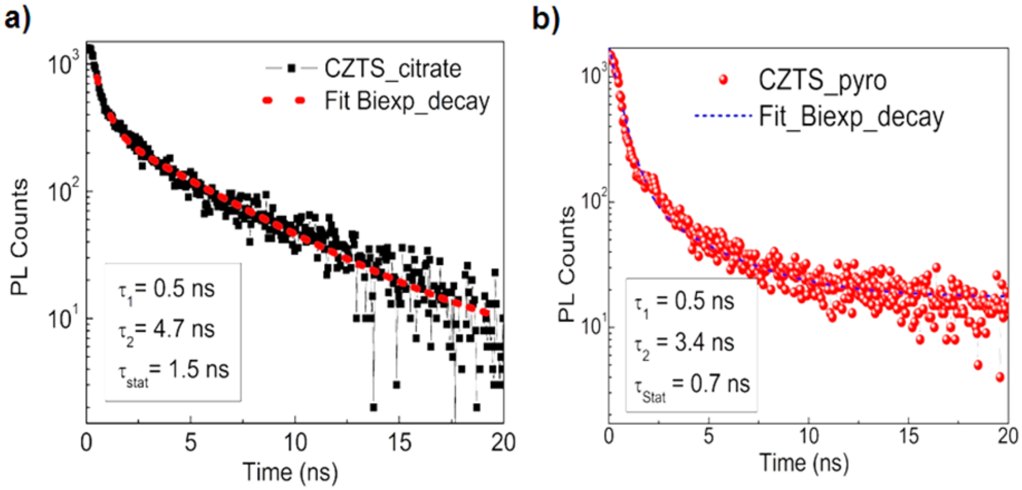

Figure 7.13 Time resolved photoluminescence measurements of a) CdS/CZTS_Citrate and b) CdS/CZTS_Pyro films

The external quantum efficiency (EQE) of the CZTS layers as a function of photon wavelength is shown in **Figure 7.14.a.** The measurements are from subcell 9 for CZTS-Citrate and subcell 5 for CZTS-Pyro. Both devices show photoresponse in the region of 300 nm to 900 nm with maximum EQE values of 11 % and 19% around 520 nm for CZTS_Pyro and CZTS_Citrate, respectively, confirming a significant recombination. The relatively high EQE result of CZTS_Citrate is consistent with the higher Jsc of this device compared to CZTS_Pyro. However, the highest value in the EQE curves are much lower than the reported values[187, 190].

The EQE spectra show significant absorption at short wavelengths around 400 nm, which originates from the ZnO phase, and the absorption around 500 nm due to the CdS layer [132, 190]. The absorption of CZTS_Citrate cell declines faster in the blue region of the spectrum (~450-500 nm) compared to CZTS_Pyro. The recombination in the CdS layer may be due to the relatively thicker or uneven layer of CdS in the CZTS_Citrate cell[191–193]. We attributed the difference in CdS thickness to a rough surface of the underlying layer, that in turn induces roughening during the chemical bath deposition of CdS.

The CZTS light absorption region ranges roughly from 400 to 800 nm and the photoresponse of CZTS cells stop at around 900 nm. In the longer wavelength region between 550 and 900 nm, the EQE data decay significantly. These drop offs can be attributed to high recombination at the interfaces, CdS/CZTS and CZTS/Mo, due to poor contact quality and/or short carrier diffusion length in the bulk of absorber layer as well as in the depletion region[187, 194, 195]. Poor carrier diffusion in the bulk of the CZTS layers is also observed with our TRPL results.

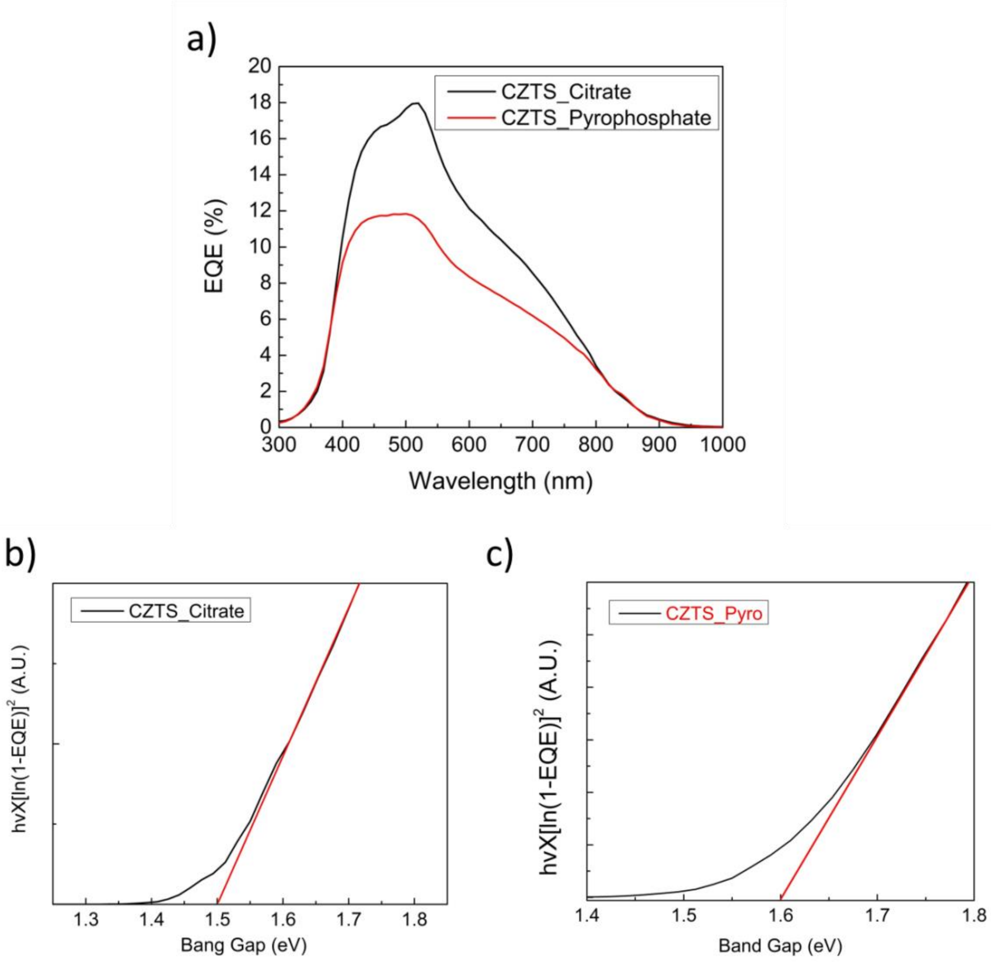

Figure 7.14 a) External quantum efficiency of CZTS films and band gaps of b) ITO/ZnO/CdS/CZTS_Citrate and c) ITO/ZnO/CdS/CZTS-Pyro cells

The band gaps are determined from the EQE data as described in **Chapter 2** and the corresponding Tauc curves are presented in **Figure 7.14.b** and **Figure 7.14.c.** The calculated band gaps are 1.5 eV and 1.6 eV for CZTS_Citrate and CZTS_Pyro, respectively. Even though the maximum EQE responses are low compared to literature values [190, 193, 194], the band gap of absorbers in the solar cells are in reasonable agreement with reported band gap values (1.45-1.6 eV) [56, 57, 196] .

VI. Conclusion

CZTS absorber layers are formed by sulfurization of electrodeposited Cu-Zn-Sn (CZT) alloy precursors from three different electrolytes on ~ 2cm^2 Mo substrate, and ITO/ZnO/CdS/CZTS/Mo solar cell devices were synthesized on top of these films. The absorber layers exhibited Cu-poor and Zn-rich composition with respect to the ideal stoichiometry, and in most cases these films contained secondary phases, particularly Cu_xS_y and Sn-rich binary phases at the surface, and Cu_2SnS_3 mostly in the bulk. The performance of the CZTS_Citrate based layers (0.64 %) was slightly better than both the CZTS_Pyro and the CZTS-Bi layers; the corresponding short circuit current Jsc was 3.87 mA/cm^2 and the open circuit voltage Voc was 390 mV. The band gap was within 1.5-1.6 eV, for both CZTS_Citrate and CZTS_Pyro; unfortunately, the pce of all cells are much lower than the values reported in the literature. We attribute these results mainly to cracks, pinholes and other morphological imperfections that are the result of the growth of a multilayer device, since the photocurrent measurements on the absorber layer, that quantify the intrinsic ability to convert radiation in charge carriers, are similar to those reported in the literature. EQE and TRPL studies suggest that the poor carrier diffusion in the absorber layer and at the interfaces, mainly originated by morphological defects, lowered the Voc, Jsc and increased the series resistance. Low Voc is attributed to the presence of secondary phases with high band gap, such as ZnS and SnS_2, which play a key role in lowering the efficiency by increasing the series resistance of the bulk. A thick layer of MoS_2 at the back contact is also a limiting factor to obtain low series resistance. On the other hand, low Jsc is attributed to the presence of the conductive phase CuxSy and to the surface imperfections, acting as a shunt path and lowering the resistance in the circuit.

Chapter 8-Conclusion and Future Work

This research effort has developed significant understanding of the potential and limitation of the electrodeposition of Cu-Zn-Sn (CZT) based metallic alloys for the synthesis of CZTS absorber layers in solar cells. Specifically, this work has investigated in detail the influence of CZT composition and sulfurization conditions on the phase purity, crystallographic properties, photoelectrochemical and solar cell performance of CZTS films. These studies provide a path forward towards a potential manufacturing method for the electrodeposition of CZT and CZT-Bi alloys using a simple electrolyte recipe for the synthesis of CZTS absorber layers, suitable for photovoltaic applications.

I. CZTS Layers Formed via Sulfurization of CZT Layers Electrodeposited from an Acidic Solution

The influence of composition of CZT metallic precursors and sulfurization temperature on the crystallographic properties and photoelectrochemical (pec) response of CZTS layers was studied and linked to the phase purity of the films. CZT metallic precursors grown on 1 cm^2 substrates showing optimum performance were Zn-rich (27-29 at%) and Cu-poor (47-49 at%) with a standard deviation of ~1.7 at% for Cu and Zn and~ 0.2 at% for Sn(~26 at%). These alloys transformed into relatively phase pure CZTS layers after sulfurization at 500 °C and 550 °C temperature, showing reasonably high pec response of 0.5 and 0.99 mA/cm^2, respectively. In our experiments, we also investigated the coexistence of ordered and disordered kesterite as it could influence the photoelectrochemical performance of the CZTS layers. XRD and Raman spectroscopy analyses revealed that the phase pure Zn-rich CZTS layer with Zn/Sn=1.34 had the highest crystallinity and a higher fraction of ordered type kesterite compared to Sn-rich layers. Solar cell characterization was performed using ~ 2.0 cm^2 size CZT based metallic precursors, which showed a higher elemental standard deviation for Cu (2.6 at%) , Zn (3.5 at%) and Sn (0.9 at%), resulting in the formation of more secondary phases in the final CZTS film. Solar cells made onto CZTS films grown from a citrate electrolyte achieved the highest efficiency of 0.64 % with 390 mV Voc, 3.87 mA/cm^2 Jsc and 43% FF. We found that Zn-rich and Cu-poor cells featured higher cell efficiency compared to Cu-rich and Zn-poor cells, a trend that was consistent with the pec response analyses and literature findings. Although all the cells of CZTS_Citrate based device were functioning with reasonable FF and moderate Voc values for CZTS type semiconductors, the presence of highly resistive phases such as SnS_2 and conductive phases like Cu_2S caused high series resistance and low shunt resistance at different locations. These phases would hinder current flow and may act as a shunt path, respectively. These detrimental phases together with the MoS_2 phase formed at the back contact were found to be responsible for the high recombination losses in the bulk and at the back contact of all of the CZTS based absorber layer solar cells discussed in this dissertation. At a different spatial scale, the presence of cracks, pinholes and morphological defects on the cell surface generate abundant recombination paths, posing significant limitations towards high efficiency.

II. CZTS Layers Formed via Sulfurization of CZT Layers Electrodeposited from an Alkaline Solution

The influence of the electrochemical deposition set up on the compositional standard deviation of the CZT based metallic precursors and the formation of secondary phases besides CZTS was studied. We found that the horizontal deposition set up decreased the standard deviation of the CZT metallic precursors from 2.3-4.5 at% to 0.5-0.7 at% in comparison with the vertical deposition set up. Top down SEM and EDS mapping analyses on the surface of the layers suggested improved phase purity at the surface of CZTS films formed from horizontally deposited CZTS precursors. Structural analyses with Raman spectroscopy also showed that phase pure CZTS layers have better crystallinity, which also showed higher pec response for Zn-rich CZTS layers with similar composition. Even though the standard deviation of the small size (0.8 cm^2) precursors was improved by using the horizontal deposition set up, the standard deviation of CZT metallic precursors became more non-uniform (1.4-3.6 at%) with the increase of the precursor size (2.0 cm^2). CZTS absorber layer grown from pyrophosphate electrolytes and the resulting solar cell device showed some non-operational regions for Sn-rich cells, whereas Zn-rich cells performed better, showing higher Voc and FF. Efficiency of the cells were less than 0.25 % due to the presence of conductive phases such as Cu_2S and MoS_2 at the back contact, similarly to the cells made with the CZTS film grown in citrate electrolyte. However, cells made by absorber layers grown by pyrophosphate showed some lateral cracks which formed bilayers in the CZTS layer. The presence of these lateral cracks could operate as a large defect in the cells, lowering the efficiency.

III. CZTS Absorber Layers Containing Bismuth

Electrodeposition of CZT-Bi layers was investigated to determine the effects of Bi (as a fluxing agent and/or as dopant) on the efficiency of the absorber layer; the metallic precursors showed more uniform layers in both 0.8 cm^2 and 2.0 cm^2 size precursors, exhibiting a lower standard deviation compared to CZT metallic precursors. The highest photoelectrochemical response, ~2.65 mA/cm^2, was observed on CZTS-Bi layer with ~0.4 at% Bi, which was attributed to the improved crystallographic properties as well as enhanced phase purity. XRD analyses evidenced an increase in crystallinity and grain size, probably owed to the growth modifier role of Bismuth in the CZTS layers. The increase in lattice parameters suggested a substitutional position of Bi atoms, possibly resulting in a dopant role for Bismuth into the CZTS crystal. However, excess amount of Bismuth (>0.5 at%) results in the growth of Bi-rich secondary phases, which reduced both pec and solar cell performance of the CZTS-Bi layers. Even though the compositional uniformity of CZTS-Bi layers were better than CZT precursors and the pec response was larger than CZTS films, the solar cell performance of CZTS-Bi was worse than CZTS based solar cells due to the presence of relatively high amount of Bi (0.6-0.9 at %) at some regions of the cells. On the other hand, Bi containing layers exhibited the highest shunt resistance among all experiments, which indicated the promising effect of Bi on the solar cell parameters.

IV. Future Work

According to the research completed in this dissertation, some additional efforts are advisable for further exploration.

Our studies are limited to only one type of acidic solution and one alkaline solution that do not contain any complexing agent. Alternative electrolytes with complexing agents should be investigated to improve the standard deviation of ternary or quaternary metallic alloys by narrowing the electrodeposition window to grow films with desirable composition; in addition, it is imperative that other additives such as organic compounds be investigated to improve the morphology and ensure film continuity and smoothness. Indeed, the low quality of the film stack has been identified as one of the main sources for the significant recombination and losses. Of particular interest for citrate based solutions, polyethylene glycol (PEG) has the potential to modify the deposition mechanism of zinc in Cu-Zn-Sn system[44, 197] by hindering rough and dendritic growth, which would decrease the surface roughness and improve the successive deposition of the CdS layer, resulting in better electrical connection at the CdS/CZTS interface to potentially prevent some losses at the front contact.

CZT metallic precursors grown from a basic solution show a relatively smooth surface; however, the lateral crack formation observed in the bulk of CZTS_Pyro layers is a problem, even if we improve the phase purity and crystallinity of the absorber layers. The reason behind the formation of such bilayer is unknown and high resolution compositional and structural investigations may help to understand the problem. The examination of in-plane compositional distribution of the metallic precursor and sulfurized films can quantify the compositional inhomogeneity, which may cause uneven growth of CZTS grains. Also, segregation of some secondary phases could be explored with improved resolution by using phase maps with Raman spectra analyses, which could be used also to inspect the bilayer problem.

Based on this work, bismuth is a promising addition for kesterite based films and its effects should be studied in detail to determine the optimum amount of Bi and its exact role in varying properties of CZTS absorber layers. Electrodeposition of Bi is possible in the Cu-Zn-Sn acidic electrolyte, resulting in a low standard deviation; however we have found that CZTS-Bi layers formed Bi-rich secondary phases for films containing more than ~0.7 at% of Bi in the CZTS layer. Therefore, a study based on the incorporation of a smaller amount of bismuth with more controlled standard deviation may result in better pec and solar cell performance. Besides, our studies showed that synthesis of Cu-Zn-Sn alloys with small amount of modifier (band gap and/or grain size) metals for CZTS is possible with electrodeposition. Electrodeposition furthermore can be used to study other promising growth modifier metals. In particular, Ni and Co could be studied, since they have been reported to modify the lattice constant and band gap of the CZTS and promote better band alignment at the Cd/CZTS interface [198–200]. Furthermore, cobalt and nickel can be co-electrodeposited from a citrate based solution owing to their suitable reduction potential in the Cu-Zn-Sn electrodeposition system as an alternative simple method to dope CZTS films[76, 201, 202]. Cobalt-containing $Cu_2Co_xZn_{1-x}SnS_4$ and Cu_2CoSnS_4 materials have been grown as nanofibers and nanorods before[198, 203]; however, a low doping amount in CZTS films for the modification of CdS/CZTS band alignment has not been reported as yet. Nickel containing $Cu_2Ni_xZn_{1-x}SnS_4$ and Cu_2NiSnS_4 materials have been grown as a film, nanofiber and nanorods [198, 199, 203]; nevertheless none of these studies reported the photoelectrochemical or solar cell performance of these materials. Cobalt containing CZTS films can be synthesized via sulfurization of co-electrodeposited Cu-Zn-Sn-Co metallic precursors on Mo substrate with varying compositional ratios for the optimization of band gap as well as band alignment for CdS/CZTS interface. In a similar way, CZTS films containing Ni can also be grown with varying compositions for further investigations in solar cell performances.

Having found a similar trend in the pec and solar cell performance for CZTS-Citrate and CZTS-Pyro, one can use pec results acquired on small size (~1 cm^2) semiconductor films to assess the ideal manufacturing process for higher performance solar cell devices. It is hoped that practical manufacturing of electrodeposited ternary and quaternary alloys to explore the compositional, crystallographic and pec studies will accelerate and lower the manufacturing cost for further investigation of CZTS and/or promising doped CZXTS based films as absorber layers for photovoltaic applications.

Appendix-1

Optimization of Sulfur Amount on the Phase Purity and PEC Performance of CZTS Layers

The first aim of these experiments is to understand the effect of amount of sulfur incorporated into the metallic precursor during the sulfurization process. The target composition for sulfur is ~50 at% for the phase pure CZTS material. Second, we seek a better understanding on the influence of sulfur amount in the quartz tube on the crystallization of the CZTS material. In the literature, sulfur partial pressure P_S has been reported to be an important parameter for the phase purity and the photoelectrochemical response of the CZTS layers[47, 139]; it is therefore important to investigate the influence of P_S on the phase formation of kesterite CZTS in our encapsulation system. To this end, we grow a set of identical samples deposited from the citrate based solution in **Chapter 3,** and sulfurize them in a quartz tube in Ar atmosphere for 1 hour at different P_S. The composition of the initial metallic precursors is close to Cu: 49.2±1.8, Zn: 26.5 ±1.2 and Sn: 24.2 ±0.7.

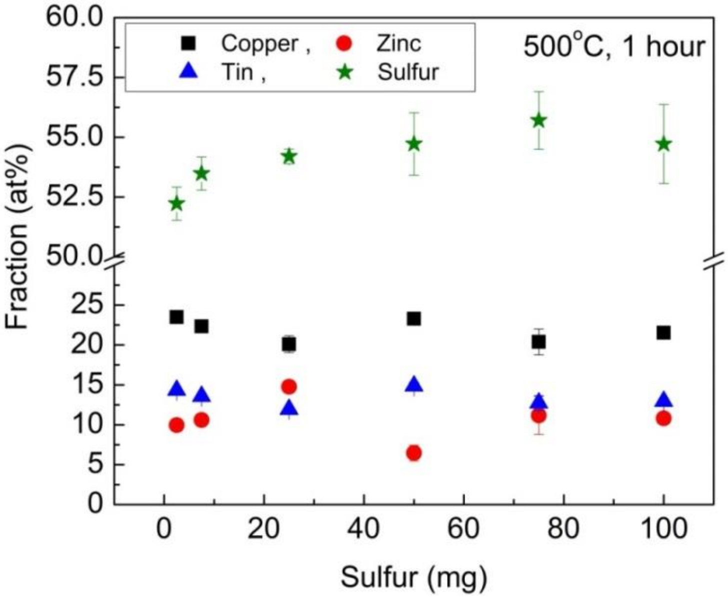

Figure A1.1 Atomic fraction of the four elements as a function of sulfur amount under sulfurization conditions of 500 °C and 1 hour

Figure A1.1 shows the composition of CZTS layers as a function of sulfur amount from 2.5 to 100 mg. The fraction of sulfur in CZTS is between 52 and 55 at % after sulfurization, and increased slightly with sulfur mass, as expected. The standard deviation of the sulfur fraction also increased with the mass of sulfur (with the exception of the 25 mg sulfur data point). The other elements on the other hand showed slightly different trend. CZTS layers was Cu-poor (< 25 at %) under all conditions, and loss of zinc was observed for most of the films. Observation of highly off-stoichiometric values suggests the possible existence of secondary phases besides the primary CZTS phase.

To gather a better insight on the bulk and surface phases of the metallic precursors after sulfurization, we investigated the structural properties with X-ray diffraction and Raman spectroscopy. Kesterite CZTS phase is observed in the X-ray patterns together with CTS phases in **Figure A1.2** CZTS sulfurized with 25 mg sulfur matches better with the theoretical peaks of the kesterite phases, with an intense peak at around $2\theta = 28.5^{o}$ and small intensity peaks at around 2θ = 18.2, 36.9 and 37.9. The presence of the low intensity peaks from the kesterite phase suggests high quality crystallization of the kesterite type materials. Even though the X-ray patterns suggests the presence of only two phases, CTS and CZTS, Raman spectroscopy studies suggests the existence of more ternary and binary phases.

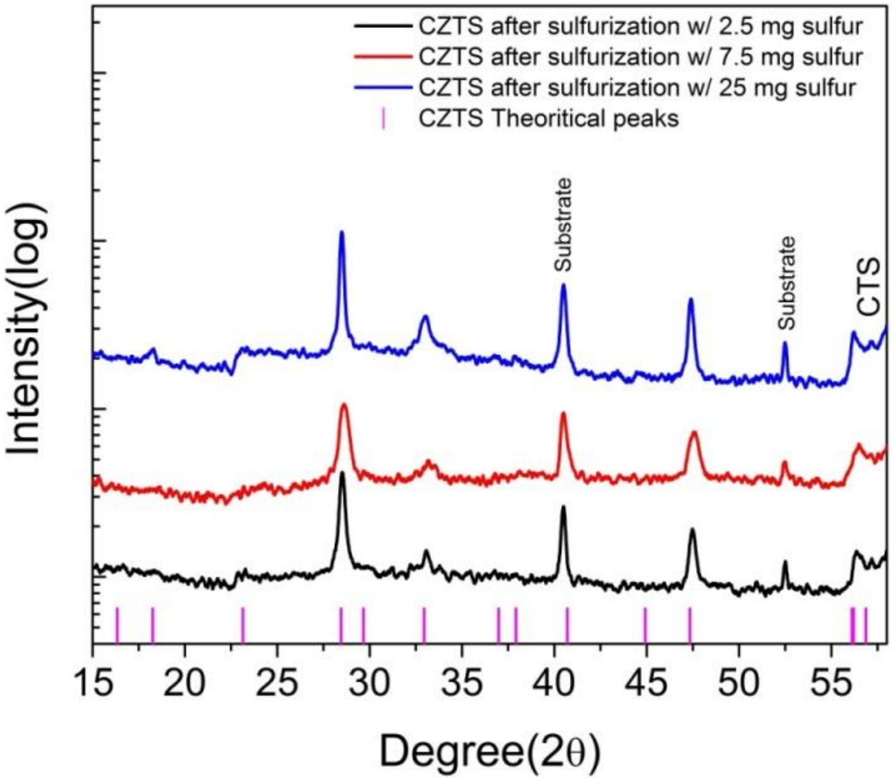

Figure A1.2 X-ray diffraction patterns for the CZTS layers sulfurized with 2.5 mg (black) , 7.5 mg (red) and 25 mg sulfur (blue)

Figure A1.3.a shows Raman spectra of the CZTS films, with markers at the bottom representing the most common secondary phases from 100 cm^{-1} to 550 cm^{-1} Raman shift. The most intense peak is observed around 337 cm^{-1} for the main CZTS Raman mode in all films. Cu_xS_y related peaks are observed for relatively high sulfur amounts, 50-100 mg, at around 475-495 cm^{-1}. A closer investigation of the Raman shift between 250 cm^{-1} and 400 cm^{-1} in **Figure A1.3.b** gives a clear proof for the existence of other secondary phases in the region between 200 cm^{-1} and 400 cm^{-1}.The broad peak at around 287 cm^{-1} indicates the existence of multiple phases other than CZTS for sulfur amounts between 2.5 mg and 7.5 mg. These phases are Sn-rich, mostly cubic CTS and some SnS_2. The Raman mode of CZTS at 287 cm^{-1} becomes sharper with increasing amount of sulfur. However, the line fitting study suggests the existence of SnS_2 phase and CTS phases when the sulfur amount was 50 to 100 mg. The Raman spectra analyses also suggest that the CZTS layer sulfurized with 25 mg sulfur fits better to the theoretical vibrational modes in comparison to the other layers.

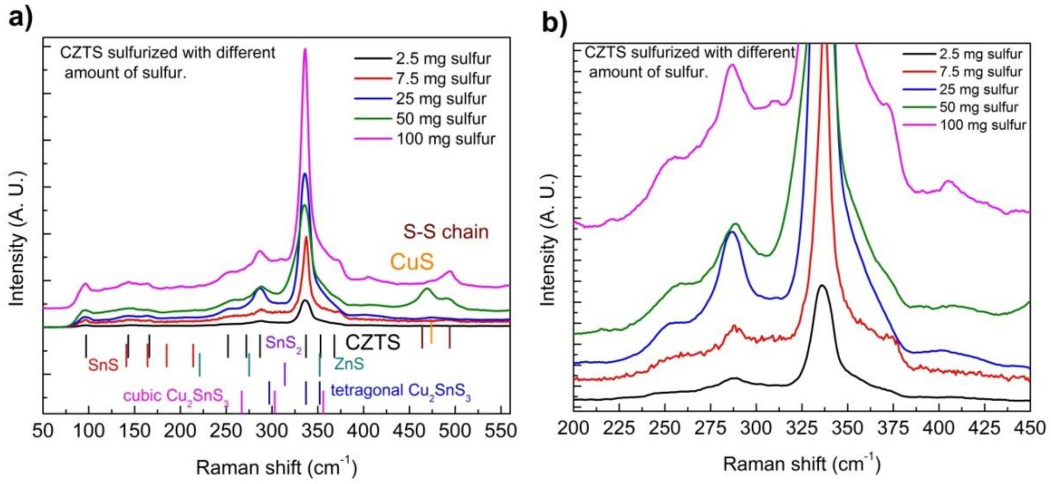

Figure A1.3 Raman spectra of CZTS layers sulfurized with different amount of sulfur a) wide range and b) narrow range

Both structural characterization methods used above have some limitations: XRD is unable to rigorously distinguish various phases, while Raman cannot probe the entire film thickness. In this context SEM images play a key role to better identify phases and assess material quality. **Figure A1.4** shows SEM images of the CZTS layers sulfurized with different amounts of sulfur. In the first two images, **Figure A1.4.a** and **Figure A1.4.b,** features with different shapes and sizes are observed. On the other hand, CZTS layer sulfurized with 25 mg and 100 mg sulfur (**Figure A1.4.c** and **Figure A1.4.d)** show uniform features with bigger grain size. However, CZTS layer formed with 100 mg sulfur shows some Sn-rich hexagonal flakes at the surface identified as SnS_2 according to Raman Spectra analysis.

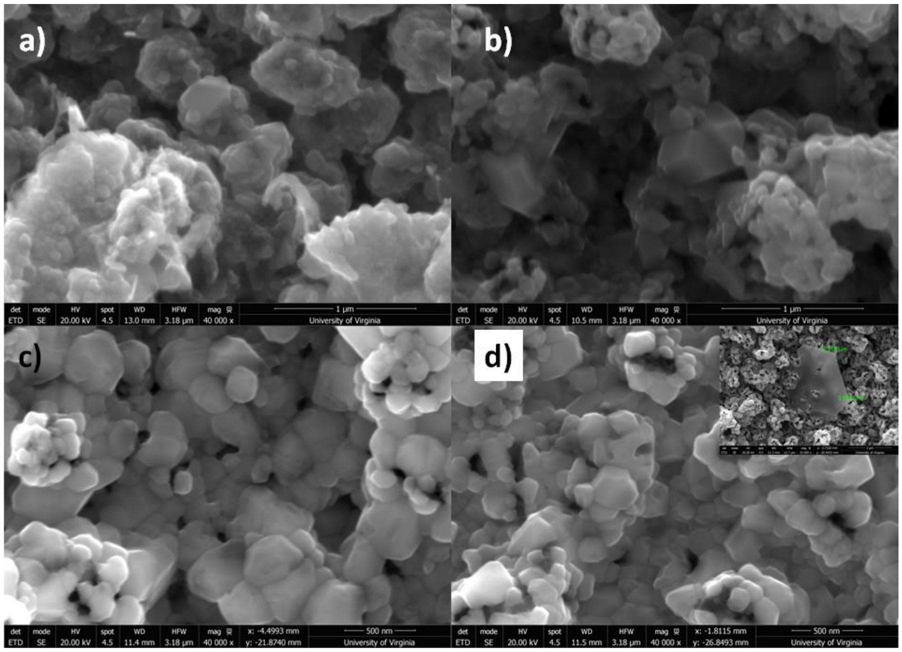

Figure A1.4 SEM image of CZTS layers sulfurized with a) 2.5 mg (scale bar 1μm) , b) 7.5mg (scale bar 500 nm), c) 25 mg (scale bar 500 nm) and d) 100 mg sulfur (scale bar 500 nm) and the inset shows a hexagonal feature for a Sn-rich secondary phase

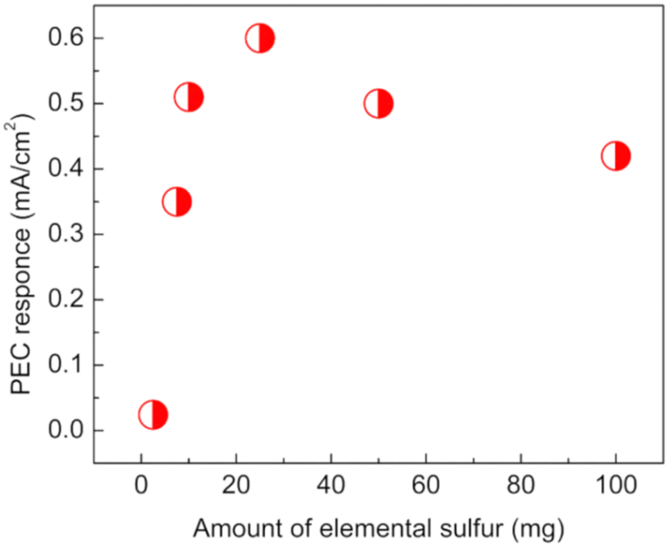

Figure A1.5 Photoelectrochemical responses of CZTS layers as a function of sulfur amount in the sulfurization tube in 0.1M Eu$(NO_3)_3$ solution with pH 2.3

The photoelectrochemical response of the CZTS layers under AM 1.5 illumination at the potential of -0.93 V_{MSE} are shown in **Figure A1.5**. The photocurrent increases with the higher amount of sulfur in the sulfurization tube up to 25 mg sulfur and begins to decrease slightly above this amount. The increase in the photoresponse is attributed mainly to the improvement of the phase purity and crystallinity between 2.5 mg and 25 mg sulfur range. The photoresponse decay above 25 mg sulfur is attributed to the presence of SnS_2, evidenced by hexagonal flakes at the surface of the CZTS layers.

Appendix-2

Influence of Sulfurization Parameters on the Formation of CZTS Layers Formed: CZT Precursors Deposited From an Alkaline Solution

Our aim is to optimize the sulfurization parameters for CZT metallic precursors electrodeposited from a basic solution. We would like to obtain continuous layer with big grain size. The grain size of polycrystalline CZTS material is reported to increase for longer sulfurization time and higher temperatures in the literature[204–209]. Increase of the grain size is desirable, because the enhancement of the grain size of the polycrystalline semiconductor limits recombination during the cell operation, which increases device performance.

To optimize the sulfurization temperature and time of our CZT precursors, first we investigated the influence of temperature and second, we studied the influence of sulfurization time for times of 20 minutes, 1 hour and 3 hours. After these processes, we investigated the morphological and structural properties of these layers, and compared the photoelectrochemical properties of the CZTS layers.

I Sulfurization Temperature and the Phase Purity of CZTS Layers

In this section, we present the influence of sulfurization temperature on the structural properties to investigate the phase purity and morphology of CZTS with relatively big grains. The sulfurization temperatures are 500°C and 550 °C with the same sulfurization conditions in Chapter 5 (1 hour with 25 mg sulfur in Ar atmosphere). All metallic precursors have close to stoichiometric Zn/Sn (stoichiometric Zn/Sn=1) and Cu-poor (Cu/(Zn+Sn)<1) ratio.

Table A2.1 shows the composition of CZT precursor layer, that of CZTS layers after sulfurization at different temperatures and the stoichiometric values for the kesterite crystal.

Table A2.1 Atomic fractions of the CZTS layers before and after sulfurization at 500 °C and 550 °C

Sulfurization Temperature (°C)	Copper (at %)	Zinc (at %)	Tin (at %)	Sulfur (at %)	Zn/Sn	Cu/ (Zn+Sn)	S/ (Cu+Zn +Sn)
As-deposited	~49.3	~23.7	~27.0	-	0.87	0.97	-
500	23.1	14.0	11.0	50.9	1.27	0.92	1.06
550	13.8	3.9	6.5	75.6	0.6	1.33	3.2
Stoichiometric	25.0	12.5	12.5	50.0	1	1	1

Before sulfurization the Zn/Sn ratio and Cu/(Zn+Sn) ratios are Zn-poor and Cu-poor. The sulfur fraction after sulfurization at 550°C increased to 75 at%, which is 25 at% more than CZTS layers sulfurized at 500°C. The ratio sulfur to cations also increased to 3.2, three times more than the stoichiometric value. As we increase the sulfurization temperature to 550 °C, the compositional ratio changes dramatically with the loss of Zn element, resulting in a highly Sn-rich and Cu-rich film. The loss of Zn has also been observed for the citrate based metallic precursors at 550 °C sulfurization temperature.

The change in compositional trend can be understood better by analysis of SEM images and Raman spectra of the CZTS layers. **Figure A2.1** shows the top down SEM images of CZTS layers sulfurized at **a)** 500 °C and **b)** 550 °C. The apparent grain size increased with increasing sulfurization temperature**. Figure A2.1.b** shows a hexagonal like Sn-rich feature much bigger than the rest of the particles.

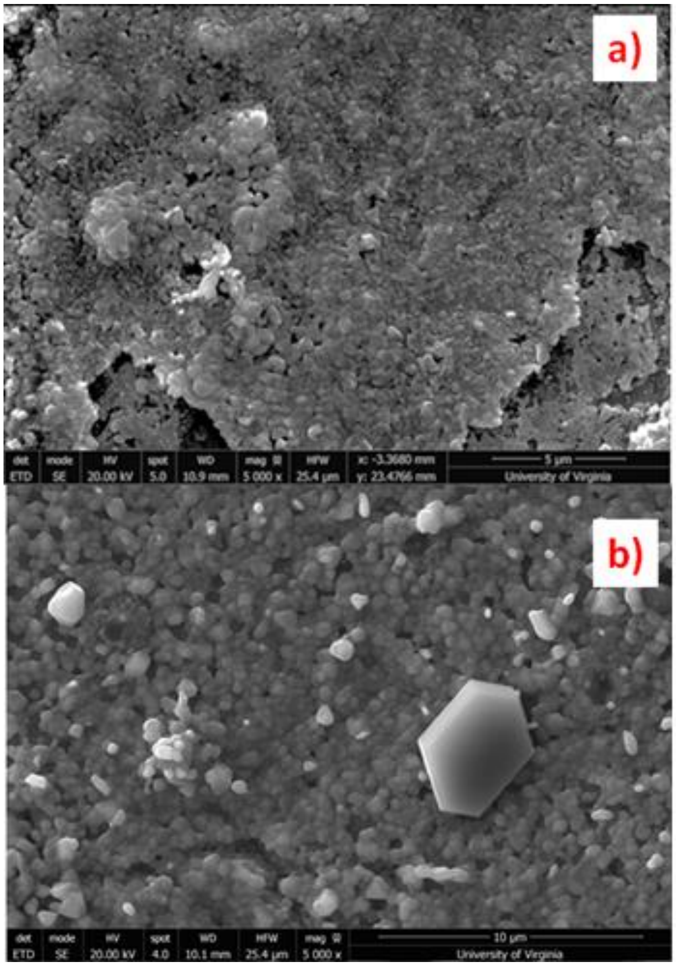

Figure A2.1SEM images of CZTS layers sulfurized at a) 500 °C and b) 550 °C

The Raman spectra acquired with 514 nm Raman excitation wavelength for CZTS layers sulfurized at 500 °C and 550 °C are shown in **Figure A2.2**. CZTS layer sulfurized at 500 C has the identical Raman peaks at 337 cm^{-1} and 287 cm^{-1}, however CZTS film sulfurized at 550 °C shows a Raman peak for the disordered type kesterite at 331 cm^{-1} without any other Raman peaks for kesterite phase. Lorentzian fitting also suggests the contribution of two peaks for the red line at around 314 cm^{-1} and 350 cm^{-1} for SnS_2 and Cu_2SnS_3 respectively. Lastly, a peak from MoS_2 is detected suggesting the existence of pinholes for the CZTS films sulfurized at 550 °C. Formation of Mo_2S is expected at the back contact interface together with phase segregation and formation of secondary phases[64].

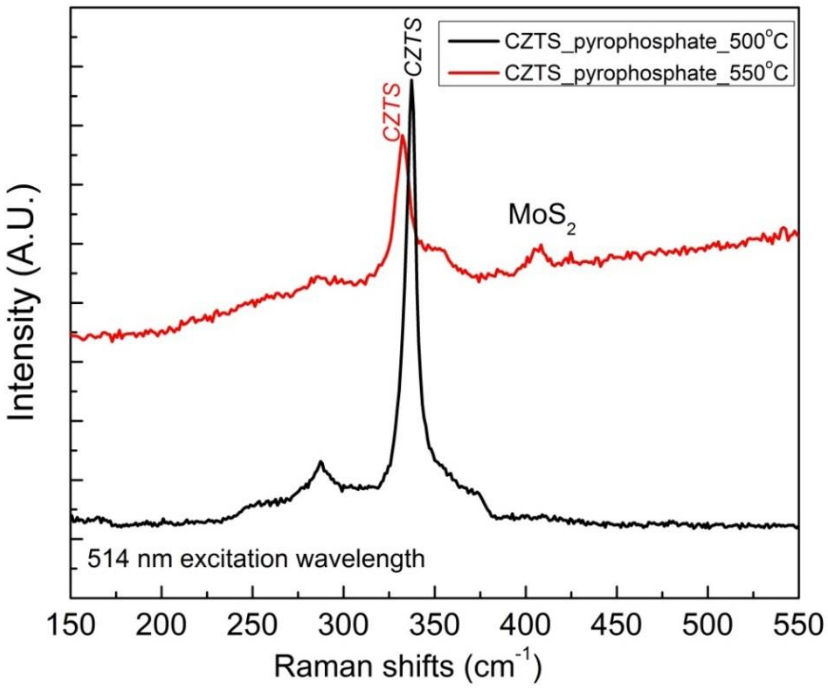

Figure A2.2 Raman Spectra of CZTS layer sulfurized at 500 °C (black line) and at 550 °C (red line)

II. Sulfurization Time and Phase Purity of CZTS layers

This study aims to understand the grain growth of CZTS together with other secondary phases a function of time. **Figure A2.3** shows the SEM image for the CZTS layer sulfurized for 20 minutes. The film has a homogenous distribution of hexagonal like features over the layers. Raman spectra of this film suggest that these hexagonal features are Cu_xS_y and SnS_2 phase. The Raman spectra with 514 nm excitation wavelength suggest that Sn-rich phase is SnS_2 (**Figure A2.4**). The composition of the CZTS layer has not changed dramatically after 20 minutes of sulfurization.

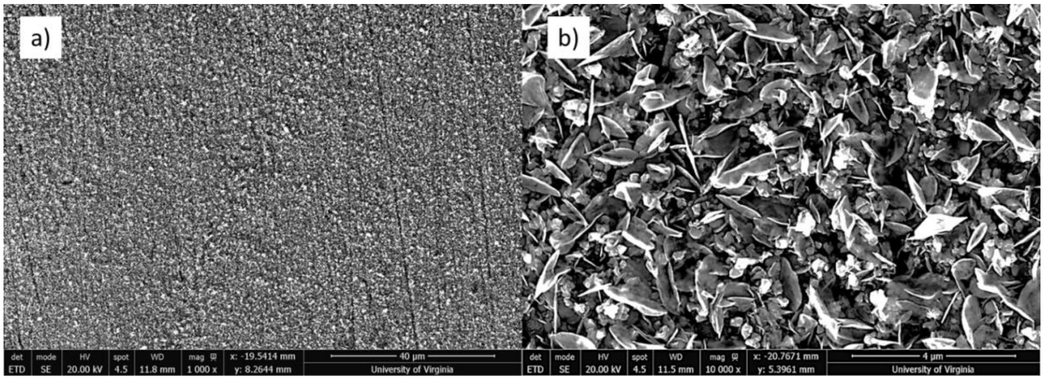

Figure A2.3 SEM image of CZTS layer sulfurized during 20 and scale bars for a) 40 µm and b) 4 µm

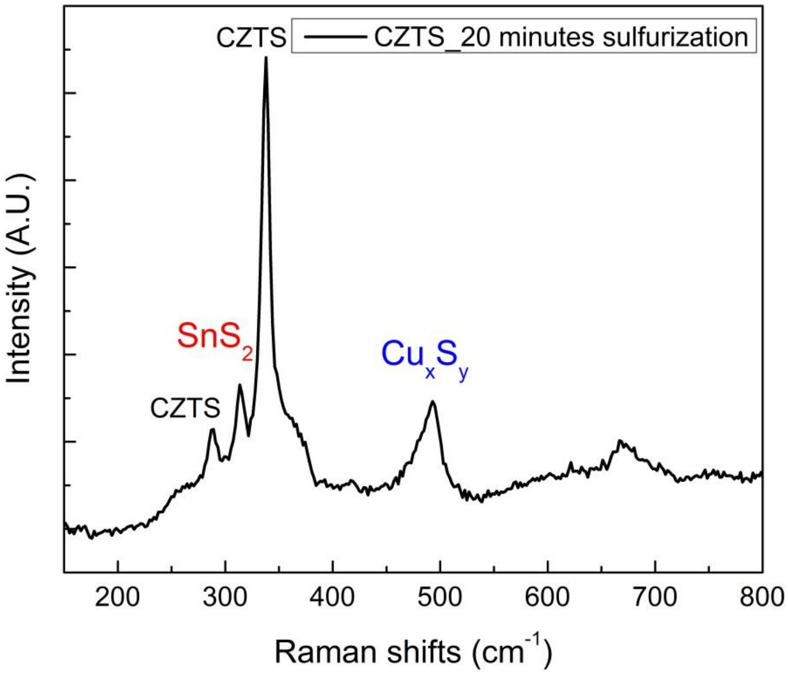

Figure A2.4 Raman spectra of CZTS layer after sulfurization for 20 minutes, 514 nm excitation wavelength

Figure A2.5 shows the SEM image of CZTS layers for sulfurization time 1 hour and 3 hours. The grain size enhancement is barely noticeable when sulfurization is increased to 3 hours (**Figure A2.5.a** and **A2.5.c**). However, we observed different features for longer time sulfurization in the lower magnification image (**Figure A2.5.d**). The composition of the layer after sulfurization for 3 hours is , S: 73.11 ±2.74, Cu: 12.87±0.7, Zn: 5.29 ±1.37, Sn: 8.7 ±0.66. The amount of sulfur and Zn loss are increased with longer sulfurization time.

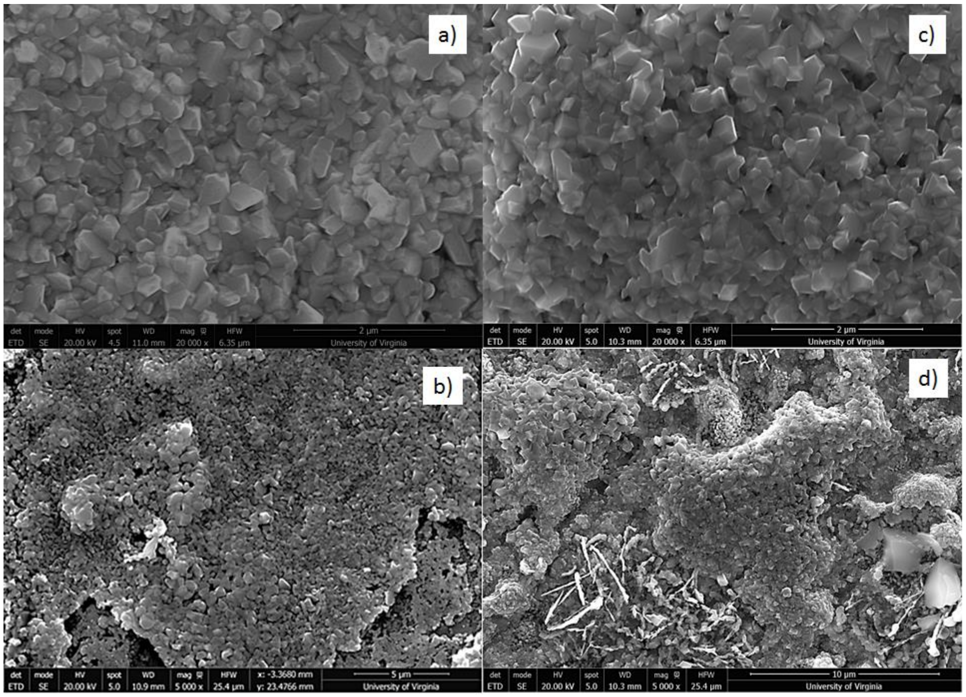

Figure A2.5 SEM images of CZTS layer sulfurized during a) scale bar 2 µm and b) 5 µm for 1 hour and c) scale bar 2 µm and d) 5 µm for 3 hours

Figure A2.6.a shows the X-ray pattern for the CZTS layer sulfurized for 3 hours. The pattern suggests the presence of SnS_2 secondary phases along with the primary phase CZTS and the secondary phase CTS. The CTS phase is also observed after 1 hour sulfurization, while the SnS_2 phase is not. We can explain the formation of the SnS_2 phase recalling the decomposition mechanism of CZTS, discussed in Chapter 5. The decomposition is reported to be related to the pressure and temperature of the system[47]; however, according to our findings the sulfurization time may also be an important factor in the formation of secondary phases even after the formation of CZTS phase. Nevertheless, these findings alone are not sufficient to prove the influence of time on the formation of secondary phases the Cu-Zn-Sn-S system.

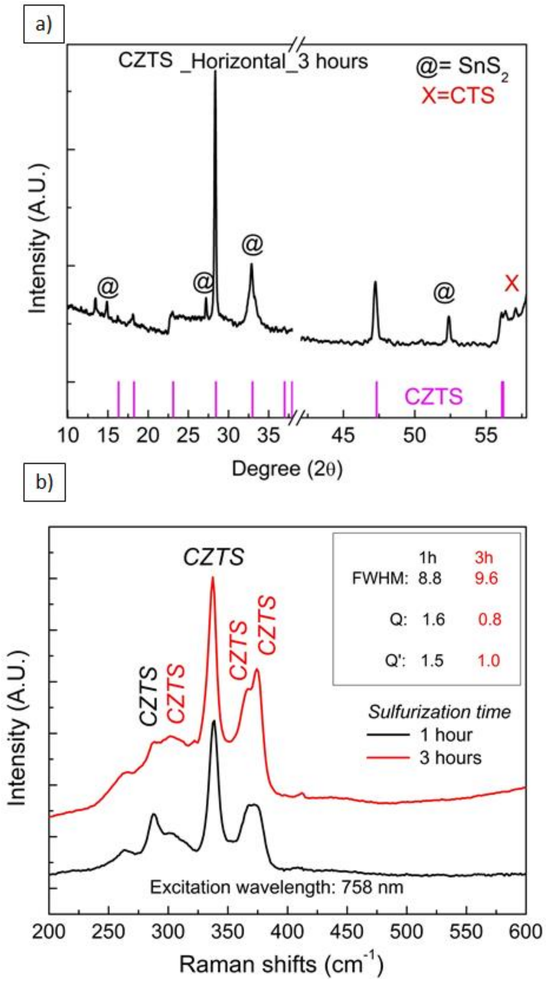

Figure A2.6 a) X-ray diffraction of CZTS layer sulfurized during 3 hours and (b) Raman spectroscopy of CZTS layers for 1 hour (black) and 3 hours (red) sulfurization

Figure A2.6.b shows the Raman spectra (785 nm) after 1 and 3 hours sulfurization time, demonstrating the influence of sulfurization time on the presence of disordered kesterite. The black line shows the spectra for 1 hour sulfurization and the red one for the 3 hours of sulfurization. The FWHM of CZTS are slightly different; however Q and Q' values changed dramatically with the increase of the sulfurization time. As the sulfurization time increases the disordered type related peaks (labeled with red CZTS) increased and the relative peak intensity ratio for the ordered type kesterite is decreased.

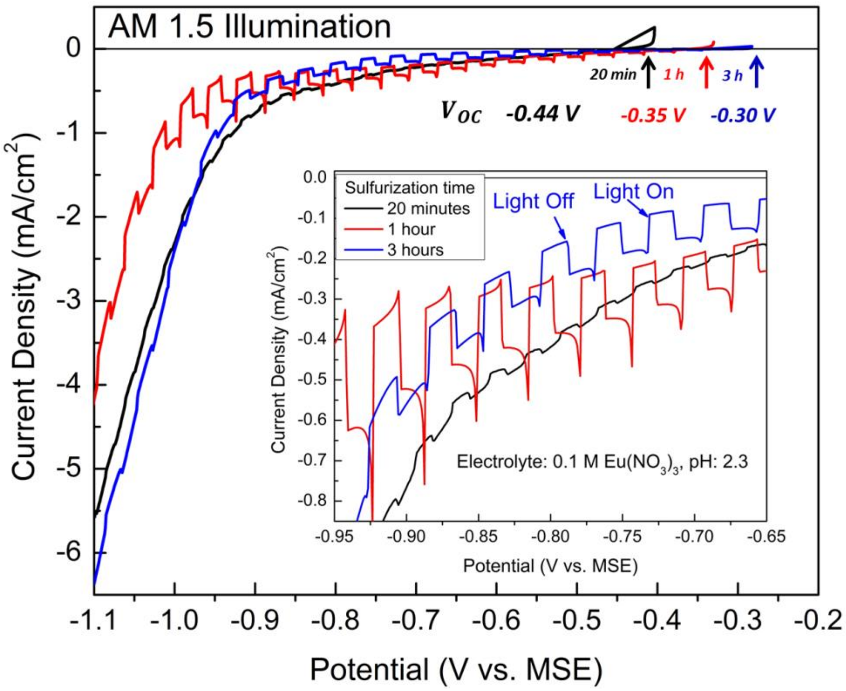

Figure A2.7 Photoelectrochemical response of CZTS layer sulfurized during 20 minutes, 1 hour and 3 hours in 0.1 M Eu(NO$_3$)$_3$ electrolyte under AM 1.5 Illumination

The pec response of the CZTS for different sulfurization times is shown in **Figure A2.7**. All CZTS layers show a photocurrent increase with increasing cathodic bias, suggesting p-type conductivity. A small photoresponse is observed together with a tiny dark current for 20 minute sulfurization time. The highest photoresponse is observed after 1 hour sulfurization, where a ~0.4 mA/cm^2 photo current is measured at potential -0.90V, which is twice more than the photoresponse of the CZTS layer sulfurized for 3 hours. We also found the open circuit potentials of these layers are slightly different than each other. Since pec characterization is sensitive to the surface quality, the different values could be due to the secondary phases at the surface, besides the phase purity of the CZTS layers.

Appendix-3

Synthesis and Characterization of Absorber Layer and Solar Cell

We synthesized CZT metallic precursors with three different recipes and fabricated solar cells with the structure ITO/ZnO/CdS/CZTS/Mo as described in Chapter 2. Since the area of the precursors had to be doubled in this chapter compared to our previous studies, the electrolyte recipe was also changed slightly to reach the desired Cu-poor and Zn-rich composition. After various experiments, we identified suitable electrolytes recipes for three CZT based metallic precursors. The CZT-Citrate electrolyte contains 0.2 M $C_6H_8O_7$, 0.2 M Na_2SO_4, 38 mM CuSO4, 36 mM $ZnSO_4$ and 30 mM $SnSO_4$ with pH 2.3. CZTB electrolyte contains 0.2 M $C_6H_8O_7$, 0.2 M Na_2SO_4, 33 mM $CuSO_4$, 36 mM $ZnSO_4$, 30 mM $SnSO_4$ and 0.5 mM $Bi_2(SO_4)_3$ with pH 2.3. The basic electrolyte consists of 0.2 M $K_2P_4O_7$, 8 mM $CuSO_4$, 30 mM $ZnSO_4$ and 5 mM $SnSO_4$ with pH 9.5. The compositional values and the standard deviation for the metallic precursors are shown in **Table A3.1**. All the precursors are Cu-poor and Zn-rich with minor differences. However, we must note that the standard deviation of these layers is higher in comparison with metallic precursors in Chapter 3, 5 and 7 due to the increase of the precursor size.

Table A3.1 Fraction of CZT based metallic precursors before sulfurization

Precursor	Copper (at%)	Zinc (at%)	Tin (at%)	Bismuth (at%)
CZT -Citrate	**44.9 ±2.6**	**31.9±3.5**	**23.2±0.9**	
CZT-Pyro	**45.8±2.3**	**31.2±3.6**	**23.0±1.4**	
CZTB	**48.7±1.1**	**28.4±1.4**	**21.4±0.7**	**1.4±0.3**

The composition of the CZTS based layers after 1 h sulfurization at 500 °C are shown in **Table A3.2**. Layers are Cu-poor and Zn-rich with close to stoichiometric sulfur expect CZTS-Bi layer, which consist of 55.5 at% sulfur with ~0.5 at% bismuth.

Table A3.2 Fraction of CZTS based metallic precursors after sulfurization

CZTS	Copper (at%)	Zinc (at%)	Tin (at%)	Bismuth (at%)	Sulfur (at%)
CZTS -Citrate	**22.9±1.1**	**14.4±1.4**	**13.8±0.9**		**48.7±1.2**
CZTS-Pyro	**23.8±1.4**	**14.6±1.3**	**12.1±1.2**		**49.5±2.9**
CZTS-Bismuth	**22.4±0.4**	**13.4±1.8**	**7.9±0.5**	**0.47±0.2**	**55.5±1.07**

The top down SEM images in **Figure A3.1** are for the Mo foil, CZTS-Pyro, CdS/Mo and CdS/CZTS_Pyro/Mo. CZTS_pyro (**Figure A3.1.b**) has continuous and dense layers of grains after sulfurization. The CdS layer is formed by chemical bath deposition on Mo foil (**Figure A3.1.c**) and on CZTS-Pyro/Mo (**Figure A3.1.d**). We used CdS/Mo image as a reference to understand the quality of the coverage over CZTS-pyro by comparing the images. The CdS films show granular grains in both cases, and CZTS-pyro crystals are covered completely. The CdS films are formed under the same conditions on CZTS-citrate and CZTS-Bismuth layers before fabricating the full cell with ZnO/ITO and metal contacts.

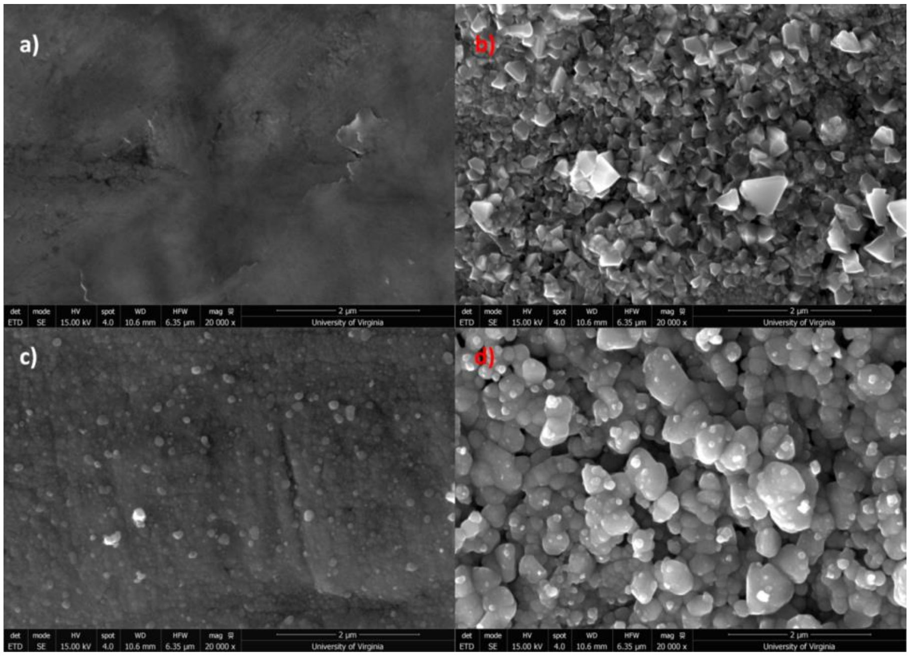

Figure A3.1 Top down SEM images of a) Mo foil, b) CZTS layer grown from pyrophosphate based solution, c) CdS on Mo foil and d) CdS/CZTS(pyro) on Mo foil

The cross section images for the CZTS-citrate and ITO/ZnO/CZTS-citrate are shown in **Figure A3.2**. The thickness of the CZTS-citrate is between 850 nm to 1120 nm with reasonably packed layer (**Figure A3.2.a**). ZnO layer has a good coverage over the CZTS layer and ITO layer has some thickness differences due to the dendrite formations of ITO.

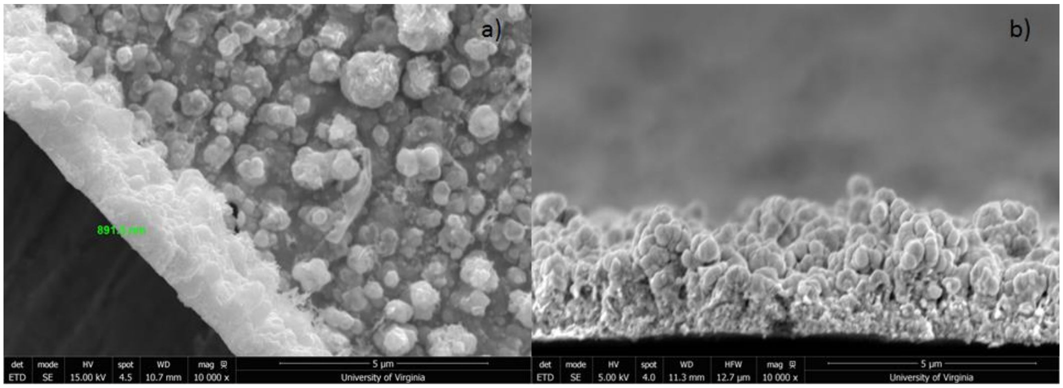

Figure A3.2 a) CZTS(citrate) SEM image and b) cross section image of ITO/ZnO/CdS/CZTS(citrate)

The thickness of the CZTS-pyro is around 1050 nm; however this layer shows a bilayer morphology, which has not been completely understood (**Figure A3.3**). **Figure A3.3.b** shows the EDS compositional mapping of the cross sectional image. The bottom part shows yellow rich color for the molybdenum substrate and the reddish color consist of the Cu-Zn-Sn-S elements for the CZTS-pyro layer. The top part of the layer shows blue rich color for the zinc and indium from ZnO and ITO layers.

XRD patterns of the CZTS_Citrate and CZTS_Pyro are shown in **Figure A3.4**. We observed peaks for the CZTS phase together with SnS and CTS phases for both films. XRD patterns of CZT films grown on 1 cm^2 substrates did not show the SnS phase, which suggests a higher fraction of secondary phases with larger size samples due to the higher standard compared to the smaller size CZT layers.

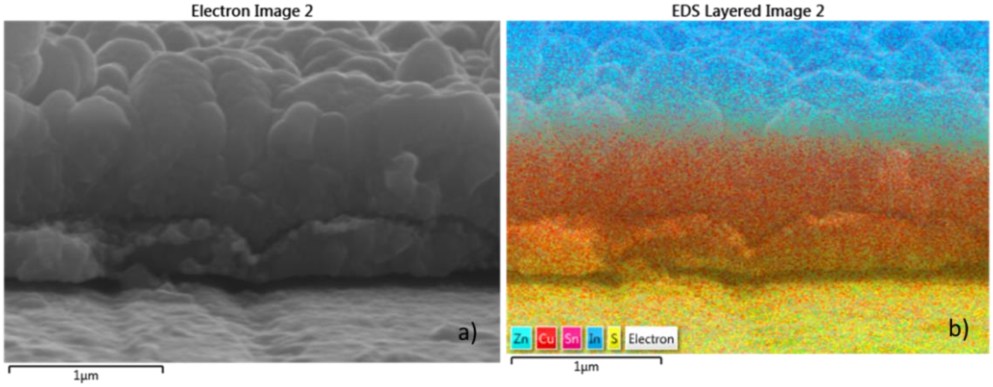

Figure A3.3 a) Cross section image of CZTS-pyro cell and b) EDS compositional mapping, color code; red for copper, light blue for zinc, pink for tin, yellow for sulfur (and molybdenum) and blue for indium

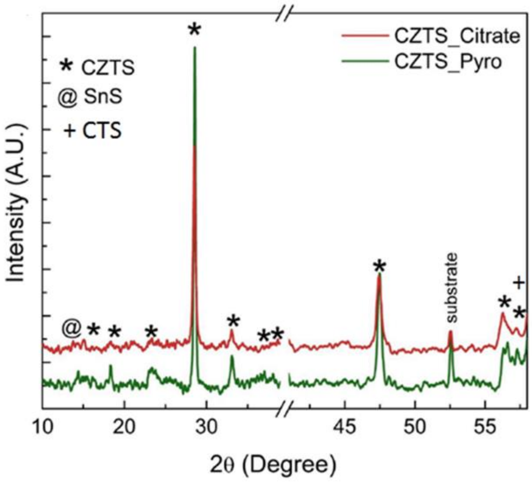

Figure A3.4 XRD patterns of CZTS_Citrate and CZTS_Pyro layers

The Raman spectrum for the CZTS based absorber layers is shown in **Figure A3.5**. The most intense phases are observed for the CZTS phase in both layers. The fraction of disordered kesterite is higher for the CZTS_Pyro compared to CZTS_Citrate according to the Raman mode intensity ratios I_{337}(ordered type kesterite)/I_{331}(disordered type kesterite). The FWHM of the CZTS_Citrate is also less than the CZTS_Pyro layer, suggesting a better crystallinity of the CZTS_Citrate film. FWHM values are close to the values observed in Chapter 4 and Chapter 6 with smaller size absorbers.

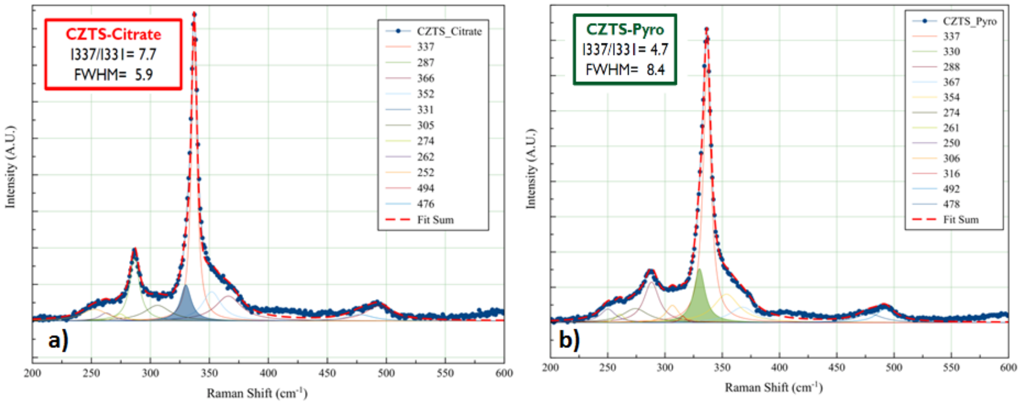

Figure A3.5 Raman spectra of a) CZTS_Citrate and b) CZTS_Pyro with 514 nm excitation wavelength

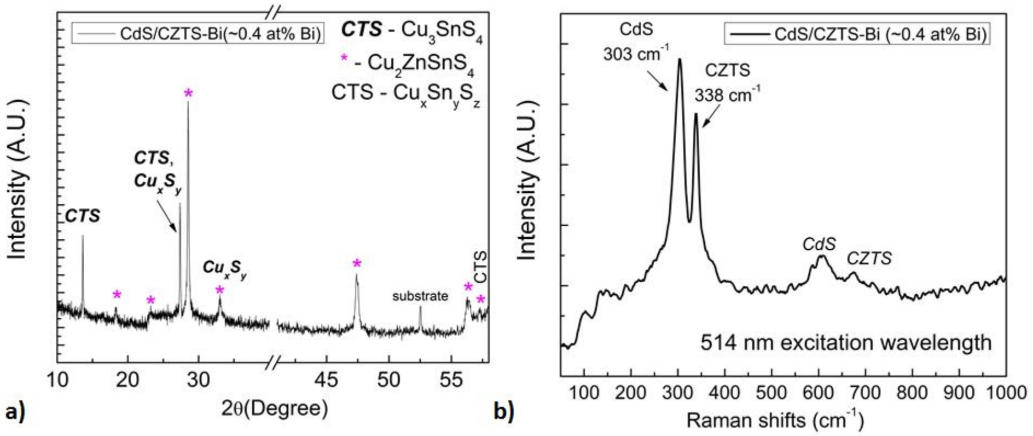

Figure A3.6 a) XRD pattern of CZTS-Bi and b) Raman spectra of CdS/CZTS-Bi with 514nm excitation wavelength

X-ray diffraction pattern and Raman spectra of CZTS-Bi layer are shown in **Figure A3.6**. The CZTS-Bismuth phase coexists with Cu_xS_y and Cu_2SnS_3 phases (**Figure A3.6**).

We also note the observation of some Bi-rich features, randomly distributed across the layer (**Figure A3.7**), and Cu-rich secondary phases in the some regions of the CZTS-Bi layers (**Figure A3.8**).

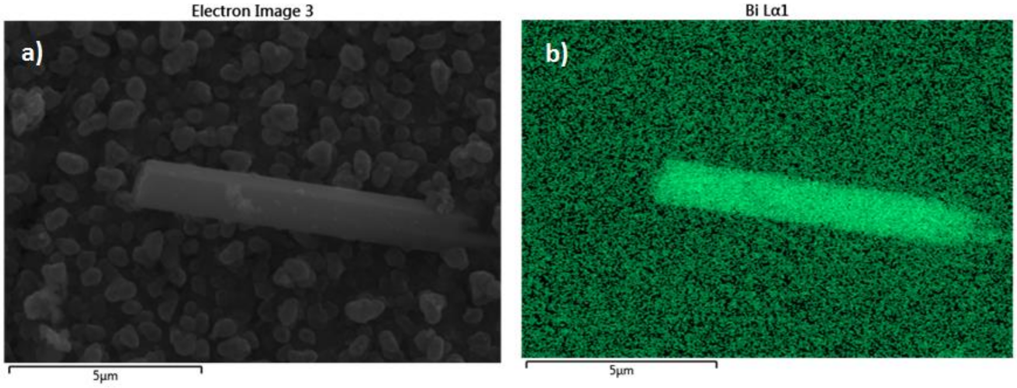

Figure A3.7 SEM image for a) CdS/CZTS-Bi absorber layer and b) EDS compositional mapping for bismuth for CdS/CZTS-Bi

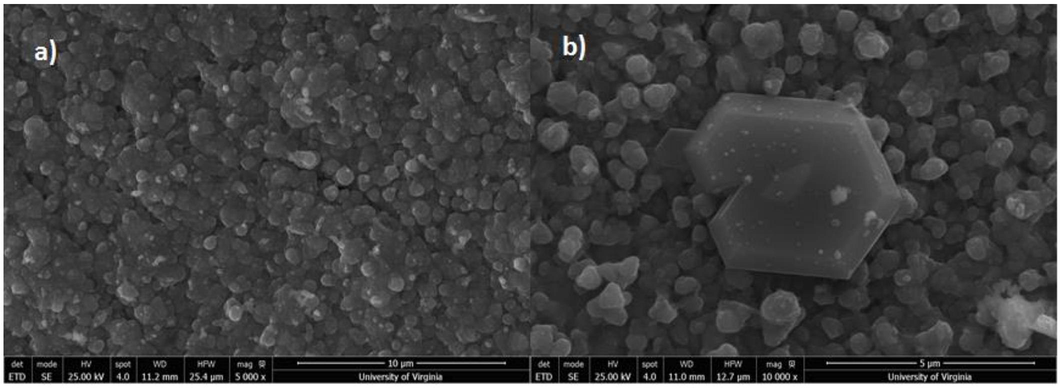

Figure A3.8 Top down SEM images of a) CdS/CZTS-Bi and b) an example for a Cu-rich secondary phase on CdS/CZTS-Bi

References

1. World Energy Council (2013) World Energy Scenarios: Composing energy futures to 2050. Rep From Http//WwwWorldenergyOrg/ 1–288.
2. DOE/EIA (2011) International energy outlook.
3. REN 21. 2014 Renewables 2014: Global Status Report.
4. International Energy Agency IEA (2014) Solar Photovoltaic Energy. Technol Roadmap 60. doi: 10.1007/SpringerReference_7300
5. Eirgrid and SONI (2013) Annual Renewable Energy Report.
6. Green M a. (2007) Thin-film solar cells: review of materials, technologies and commercial status. J Mater Sci Mater Electron 18:15–19. doi: 10.1007/s10854-007-9177-9
7. Marwede M, Reller A (2014) Estimation of life cycle material costs of cadmium telluride- and copper indium gallium diselenide-photovoltaic absorber materials based on life cycle material flows. J Ind Ecol 18:254–267. doi: 10.1111/jiec.12108
8. Parida B, Iniyan S, Goic R (2011) A review of solar photovoltaic technologies. Renew Sustain Energy Rev 15:1625–1636. doi: 10.1016/j.rser.2010.11.032
9. Peter LM (2011) Towards sustainable photovoltaics: the search for new materials. Philos Trans R Soc A Math Phys Eng Sci 369:1840–1856. doi: 10.1098/rsta.2010.0348
10. Colegrove E, Banai R, Blissett C, et al. (2012) High-efficiency polycrystalline CdS/CdTe solar cells on buffered commercial TCO-coated glass. J Electron Mater 41:2833–2837. doi: 10.1007/s11664-012-2100-z
11. “Flisom: Flexible PV from Lab to Fab” (2014) Flisom.
12. Jiang C, Noufi R, Ramanathan K, et al. (2005) Local Built-in Potential on Grain Boundary of Cu (In , Ga) Se2 Thin Films.
13. Redlinger M, Eggert R, Woodhouse M (2015) Evaluating the availability of gallium, indium, and tellurium from recycled photovoltaic modules. Sol Energy Mater Sol Cells 138:58–71. doi: 10.1016/j.solmat.2015.02.027
14. Snaith HJ (2013) Perovskites : The Emergence of a New Era for Low-Cost , High-. J Phys Chem Lett 4:3623−3630. doi: 10.1021/jz4020162
15. Jeon NJ, Noh JH, Kim YC, et al. (2014) Solvent engineering for high-performance inorganic-organic hybrid perovskite solar cells. Nat Mater 13:1–7. doi: 10.1038/nmat4014
16. Yu J, Zheng Y, Huang J (2014) Towards High Performance Organic Photovoltaic Cells: A Review of Recent Development in Organic Photovoltaics. Polymers (Basel) 6:2473–2509. doi: 10.3390/polym6092473
17. Kamat PVP (2013) Quantum Dot Solar Cells . The Next Big Thing in Photovoltaics. J Phys Chem Lett 4:908–918. doi: 10.1021/jz400052e
18. Bera D, Qian L, Tseng TK, Holloway PH (2010) Quantum dots and their multimodal applications: A review. Materials (Basel) 3:2260–2345. doi: 10.3390/ma3042260
19. Barkhouse DAR, Gunawan O, Gokmen T, et al. (2012) Device characteristics of a 10.1% hydrazine-processed Cu2ZnSn(Se,S)4 solar cell. Prog Photovoltaics Res Appl 20:6–11. doi: 10.1002/pip
20. Septina W, Ikeda S, Kyoraiseki A, et al. (2013) Single-step electrodeposition of a microcrystalline Cu2ZnSnSe4 thin film with a kesterite structure. Electrochim Acta 88:436–442. doi: 10.1016/j.electacta.2012.10.076
21. Grossberg M, Krustok J, Timmo K, Altosaar M (2009) Radiative recombination in Cu2ZnSnSe4 monograins studied by photoluminescence spectroscopy. Thin Solid Films 517:2489–2492. doi: 10.1016/j.tsf.2008.11.024
22. Kar M, Hillhouse HW, Agrawal R (2012) Chemical liquid deposition of CuInSe 2 and CuIn (S , Se) 2 films for solar cells. Thin Solid Films 520:5431–5437. doi: 10.1016/j.tsf.2012.04.012
23. Repins I, Beall C, Vora N, et al. (2012) Co-evaporated Cu2ZnSnSe4 films and devices. Sol

Energy Mater Sol Cells 101:154–159. doi: 10.1016/j.solmat.2012.01.008
24. Wang W, Winkler MT, Gunawan O, et al. (2014) Device characteristics of CZTSSe thin-film solar cells with 12.6% efficiency. Adv Energy Mater 4:1–5. doi: 10.1002/aenm.201301465
25. Wallace SK, Mitzi DB, Walsh A (2017) The Steady Rise of Kesterite Solar Cells. ACS Energy Lett 776–779. doi: 10.1021/acsenergylett.7b00131
26. Kumar M, Dubey A, Adhikari N, et al. (2015) Strategic review of secondary phases, defects and defect-complexes in kesterite CZTS–Se solar cells. Energy Environ Sci 8:3134–3159. doi: 10.1039/C5EE02153G
27. Kumar M, Dubey A, Adhikari N, et al. (2015) Strategic review of secondary phases, defects and defect-complexes in kesterite CZTS–Se solar cells. Energy Environ Sci 8:3134–3159. doi: 10.1039/C5EE02153G
28. Scragg JJS, Larsen JK, Kumar M, et al. (2016) Cu-Zn disorder and band gap fluctuations in Cu2ZnSn(S,Se)4: Theoretical and experimental investigations. Phys Status Solidi Basic Res 253:247–254. doi: 10.1002/pssb.201552530
29. Berg DM, Arasimowicz M, Djemour R, et al. (2014) Discrimination and detection limits of secondary phases in Cu2ZnSnS4 using X-ray diffraction and Raman spectroscopy. Thin Solid Films 569:113–123. doi: 10.1016/j.tsf.2014.08.028
30. Walsh A, Wei S-H, Chen S, Gong XG (2009) Design of quaternary chalcogenide photovoltaic absorbers through cation mutation. 2009 34th IEEE Photovolt Spec Conf 001875–001878. doi: 10.1109/PVSC.2009.5411555
31. Hall SR, Szymanski JT, Stewart JM (1978) Kesterite, Cu2(Zn,Fe)SnS4 and Stannite Cu2(Fe,Zn)SnS4, structurally similar but distinct minerals. Can Mineral 16:131–137.
32. Shibuya T, Goto Y, Kamihara Y, et al. (2014) From kesterite to stannite photovoltaics: Stability and band gaps of the Cu2(Zn,Fe)SnS4 alloy. Appl Phys Lett 104:3–6. doi: 10.1063/1.4862030
33. Zhao W, Du L-Y, Liu L-L, et al. (2017) Low-temperature phase transformation of CZTS thin films. Chinese Phys B 26:46402. doi: 10.1088/1674-1056/26/4/046402
34. Kentaro Ito, Copper Zinc Tin Sulfide-Based Thin Film Solar Cells, John Wiley & Sons, United Kingdom, Chapter 3.
35. Yu K, Carter EA (2015) A strategy to stabilize kesterite CZTS for high-performance solar cells. Chem Mater 27:2920–2927. doi: 10.1021/acs.chemmater.5b00172
36. Bourdais S, Choné C, Delatouche B, et al. (2016) Is the Cu/Zn Disorder the Main Culprit for the Voltage Deficit in Kesterite Solar Cells? Adv Energy Mater 6:1–21. doi: 10.1002/aenm.201502276
37. Olekseyuk ID, Dudchak I V., Piskach L V. (2004) Phase equilibria in the Cu2S-ZnS-SnS2 system. J Alloys Compd 368:135–143. doi: 10.1016/j.jallcom.2003.08.084
38. G. Moh (1975) Tin containing mineral systems. II. Phase relations and mineral assemblages in the copper-iron-zinc-tin-sulfur system. Chemie der Erde 34:1–61.
39. Lund EA, Du H, Hlaing Oo WM, et al. (2014) Investigation of combinatorial coevaporated thin film Cu 2ZnSnS4 (II): Beneficial cation arrangement in Cu-rich growth. J Appl Phys 115:1–11. doi: 10.1063/1.4871665
40. Vasyl Tomashyk, Petro Feychuk LS (2014) Ternary Alloys Based on II-VI Semiconductor Compounds. Taylor & Fisher, Boca Raton, FL
41. Guan H, Shen H, Gao C, He X (2013) Structural and optical properties of Cu2SnS3 and Cu3SnS4 thin films by successive ionic layer adsorption and reaction. J Mater Sci Mater Electron 24:1490–1494. doi: 10.1007/s10854-012-0960-x
42. Fiechter S, Martinez M, Schmidt G, et al. (2003) Phase relations and optical properties of semiconducting ternary sulfides in the system Cu-Sn-S. J Phys Chem Solids 64:1859–1862. doi: 10.1016/S0022-3697(03)00172-0
43. Tong Z, Yan C, Su Z, et al. (2014) Effects of potassium doping on solution processed kesterite Cu2ZnSnS4 thin film solar cells. Appl Phys Lett. doi: 10.1063/1.4903500

44. Slupska M, Ozga P (2014) Electrodeposition of Sn-Zn-Cu alloys from citrate solutions. Electrochim Acta 141:149–160. doi: 10.1016/j.electacta.2014.07.039
45. He J, Sun L, Chen Y, et al. (2015) Influence of sulfurization pressure on Cu2ZnSnS4 thin films and solar cells prepared by sulfurization of metallic precursors. J Power Sources 273:600–607. doi: 10.1016/j.jpowsour.2014.09.088
46. Piacente V, Foglia S, Scardala P (1991) Sublimation study of the tin sulphides SnS2, Sn2S3 and SnS. J Alloys Compd 177:17–30. doi: 10.1016/0925-8388(91)90053-X
47. Scragg JJ, Ericson T, Kubart T, et al. (2011) Chemical insights into the instability of Cu2ZnSnS4 films during annealing. Chem Mater 23:4625–4633. doi: 10.1021/cm202379s
48. Alvarez A, Exarhos S, Mangolini L (2016) Tin disulfide segregation on CZTS films sulfurized at high pressure. Mater Lett 165:41–44. doi: 10.1016/j.matlet.2015.11.090
49. Zhou X, Zeng X, Yan X, et al. (2014) Shape- and phase-controlled ZnS nanostructures and their optical properties. Mater Res Bull 59:25–31. doi: 10.1016/j.materresbull.2014.06.027
50. Zhang H, Huang F, Gilbert B, Banfield JF (2003) Molecular Dynamics Simulations, Thermodynamic Analysis, and Experimental Study of Phase Stability of Zinc Sulfide Nanoparticles. J Phys Chem B 107:13051–13060. doi: 10.1021/jp036108t
51. Baars J, Brandt G (1973) Structural Phase Transition in ZnS. J Phys Chem Solids 34:905–909.
52. Nagoya A, Asahi R, Kresse G (2011) First-principles study of Cu $_2$ ZnSnS $_4$ and the related band offsets for photovoltaic applications. J Phys Condens Matter 23:404203. doi: 10.1088/0953-8984/23/40/404203
53. Chakrabarti DJ, Laughlin DE (1983) The Cu-S (Copper-Sulfur) system. Bull Alloy Phase Diagrams 4:254–271. doi: 10.1007/BF02868665
54. Berg DM (2012) Kesterite Equilibrium Reaction and the Discrimination of Secondary Phases from Cu2ZnSnS4. Dr Thesis 187.
55. Lukashev P, Lambrecht WRL, Kotani T, van Schilfgaarde M (2007) Electronic and crystal structure of Cu2-xS : Full-potential electronic structure calcul. Phys Rev B 76:195202. doi: 10.1103/PhysRevB.76.195202
56. Jackson AJ, Walsh A (2014) Abinitio thermodynamic model of Cu 2 ZnSnS 4. J Mater Chem A 2:7829–7836. doi: 10.1039/C4TA00892H
57. Siebentritt S, Schorr S (2012) Kesterites — a challenging material for solar cells. Prog Photovoltaics Res Appl. doi: 10.1002/pip
58. Jia Z, Chen Q, Chen J, et al. (2015) The photovoltaic properties of novel narrow band gap Cu 2 SnS 3 films prepared by a spray pyrolysis method. RSC Adv 5:28885–28891. doi: 10.1039/c5ra01610j
59. Zhai YT, Chen S, Yang JH, et al. (2011) Structural diversity and electronic properties of Cu2SnX 3 (X=S, Se): A first-principles investigation. Phys Rev B - Condens Matter Mater Phys 84:1–6. doi: 10.1103/PhysRevB.84.075213
60. Price LS, Parkin IP, Hardy AME, et al. (1999) Atmospheric Pressure Chemical Vapor Deposition of Tin Sulfides (SnS, Sn2S3 , and SnS2) on Glass. Chem Mater 11:1792–1799. doi: 10.1021/cm990005z
61. Kurnia F, Hart JN (2015) Band-Gap Control of Zinc Sulfide: Towards an Efficient Visible-Light-Sensitive Photocatalyst. ChemPhysChem 16:2397–2402. doi: 10.1002/cphc.201500264
62. Chen, S., Gong, X., Walsh, A., & Wei S (2011). Structural, Electronic and Defect Properties of Cu2ZnSn(S,Se)4 Alloys. MRS Proceedings, 1370. doi:10.1557/opl.2011.764.
63. Jackson P, Hariskos D, Lotter E, et al. (2011) New world record efficiency for Cu (In , Ga) Se 2 thin-film solar cells beyond 20 %. 894–897. doi: 10.1002/pip
64. Scragg JJ, Kubart T, J. Timo Wätjen JT, et al. (2013) Effects of back contact instability on Cu2ZnSnS4 devices and processes. Chem Mater 25:3162–3171. doi: 10.1021/cm4015223
65. Mitzi DB, Gunawan O, Todorov TK, et al. (2011) The path towards a high-performance

solution-processed kesterite solar cell. Sol Energy Mater Sol Cells 95:1421–1436. doi: 10.1016/j.solmat.2010.11.028

66. Yakuphanoglu F (2011) Nanostructure Cu2ZnSnS4 thin film prepared by sol-gel for optoelectronic applications. Sol Energy 85:2518–2523. doi: 10.1016/j.solener.2011.07.012
67. Sivula K (2014) Enhancing the Charge Separation in Nanocrystalline Cu 2 ZnSnS 4 Photocathodes for Photoelectrochemical Application: The Role of Surface Modi fi cations. J Phys Chem Lett 5:3902–3908. doi: 10.1021/jz501996s
68. Araki H, Kubo Y, Jimbo K, et al. (2009) Preparation of Cu 2 ZnSnS 4 thin films by sulfurization of co-electroplated Cu-Zn-Sn precursors. Phys Status Solidi 6:1266–1268. doi: 10.1002/pssc.200881182
69. Scragg JJ, Berg DM, Dale PJ (2010) A 3.2% efficient Kesterite device from electrodeposited stacked elemental layers. J Electroanal Chem 646:52–59. doi: 10.1016/j.jelechem.2010.01.008
70. Ahmed S, Reuter KB, Gunawan O, et al. (2012) A High Efficiency Electrodeposited Cu2ZnSnS4 Solar Cell. Adv Energy Mater 2:253–259. doi: 10.1002/aenm.201100526
71. Jiang F, Ikeda S, Harada T, Matsumura M (2014) Pure Sulfide Cu2ZnSnS4 thin film solar cells fabricated by preheating an electrodeposited metallic stack. Adv Energy Mater 4:2–5. doi: 10.1002/aenm.201301381
72. Yao L, Ao J, Jeng MJ, et al. (2017) A CZTSe solar cell with 8.2% power conversion efficiency fabricated using electrodeposited Cu/Sn/Zn precursor and a three-step selenization process at low Se pressure. Sol Energy Mater Sol Cells 159:318–324. doi: 10.1016/j.solmat.2016.09.028
73. Colombara D, Crossay, A.Jaime S, Arasimowicz M, et al. (2015) Electrodeposition of kesterite thin films for photovoltaic applications: Quo vadis? Phys Status Solidi 212:88–102. doi: 10.1002/pssa.201431364
74. Li J, Ma T, Wei M, et al. (2012) The Cu2ZnSnSe4 thin films solar cells synthesized by electrodeposition route. Appl Surf Sci 258:6261–6265. doi: 10.1016/j.apsusc.2012.03.006
75. Gougaud C, Rai D, Delbos S, et al. (2013) Electrochemical Studies of One-Step Electrodeposition of Cu-Sn-Zn Layers from Aqueous Electrolytes for Photovoltaic Applications. J Electrochem Soc 160:D485–D494. doi: 10.1149/2.105310jes
76. Chen Z, Han L, Wan L, et al. (2011) Cu2ZnSnSe4 thin films prepared by selenization of co-electroplated Cu-Zn-Sn precursors. Appl Surf Sci 257:8490–8492. doi: 10.1016/j.apsusc.2011.04.139
77. Juškėnas R, Kanapeckaitė S, Karpavičienė V, et al. (2012) A two-step approach for electrochemical deposition of Cu–Zn–Sn and Se precursors for CZTSe solar cells. Sol Energy Mater Sol Cells 101:277–282. doi: 10.1016/j.solmat.2012.02.007
78. Ennaoui A, Lux-Steiner M, Weber A, et al. (2009) Cu2ZnSnS4 thin film solar cells from electroplated precursors: Novel low-cost perspective. Thin Solid Films 517:2511–2514. doi: 10.1016/j.tsf.2008.11.061
79. Schurr R, Hölzing A, Jost S, et al. (2009) The crystallisation of Cu2ZnSnS4 thin film solar cell absorbers from co-electroplated Cu–Zn–Sn precursors. Thin Solid Films 517:2465–2468. doi: 10.1016/j.tsf.2008.11.019
80. Khalil MI, Bernasconi R, Ieffa S, et al. (2015) Effect of co-electrodeposited Cu-Zn-Sn precursor compositions on sulfurized CZTS thin films for solar cell M. I. Khalil. ECS Trans 64:33–41.
81. Khalil MI, Bernasconi R, Pedrazzetti L, et al. (2017) Co-Electrodeposition of Metallic Precursors for the Fabrication of CZTSe Thin Films Solar Cells on Flexible Mo Foil. J Electrochem Soc 164:D302–D306. doi: 10.1149/2.1001706jes
82. Kondrotas R, Juškėnas R, Naujokaitis a., et al. (2015) Characterization of Cu2ZnSnSe4 solar cells prepared from electrochemically co-deposited Cu–Zn–Sn alloy. Sol Energy Mater Sol Cells 132:21–28. doi: 10.1016/j.solmat.2014.08.010

83. Clauwaert K, Binnemans K, Matthijs E, Fransaer J (2016) Electrochemical studies of the electrodeposition of copper-zinc-tin alloys from pyrophosphate electrolytes followed by selenization for CZTSe photovoltaic cells. Electrochim Acta 188:344–355. doi: 10.1016/j.electacta.2015.12.013
84. Zhang Y, Liao C, Zong K, et al. (2013) Cu2ZnSnSe4 thin film solar cells prepared by rapid thermal annealing of co-electroplated Cu-Zn-Sn precursors. Sol Energy 94:1–7. doi: 10.1016/j.solener.2013.05.002
85. Hreid T, O'Mullane AP, Spratt HJ, et al. (2016) Investigation of the electrochemical growth of a Cu–Zn–Sn film on a molybdenum substrate using a citrate solution. J Appl Electrochem 46:769–778. doi: 10.1007/s10800-016-0967-8
86. Kondrotas R, Juškėnas R, Naujokaitis a., et al. (2015) Characterization of Cu2ZnSnSe4 solar cells prepared from electrochemically co-deposited Cu–Zn–Sn alloy. Sol Energy Mater Sol Cells 132:21–28. doi: 10.1016/j.solmat.2014.08.010
87. Gougaud C, Rai D, Delbos S, et al. (2013) Electrochemical Studies of One-Step Electrodeposition of Cu-Sn-Zn Layers from Aqueous Electrolytes for Photovoltaic Applications. J Electrochem Soc 160:D485–D494. doi: 10.1149/2.105310jes
88. Khalil I, Bernasconi R, Magagnin L (2014) CZTS layers for solar cells by an electrodeposition-annealing route. Electrochim Acta 145:154–158. doi: 10.1016/j.electacta.2014.09.001
89. Jiang F, Ikeda S, Harada T, Matsumura M (2014) Pure Sulfide Cu2ZnSnS4 thin film solar cells fabricated by preheating an electrodeposited metallic stack. Adv Energy Mater 4:2–5. doi: 10.1002/aenm.201301381
90. Chen S, Walsh A, Gong X-G, Wei S-H (2013) Classification of lattice defects in the kesterite Cu2ZnSnS4 and Cu2ZnSnSe4 earth-abundant solar cell absorbers. Adv Mater 25:1522–39. doi: 10.1002/adma.201203146
91. Colombara D, Crossay a., Vauche L, et al. (2015) Electrodeposition of kesterite thin films for photovoltaic applications: Quo vadis? Phys Status Solidi Appl Mater Sci 212:88–102. doi: 10.1002/pssa.201431364
92. Liu F, Deng Y, Han X, et al. (2016) Electrodeposition of metals and alloys from ionic liquids. J Alloys Compd 654:163–170. doi: 10.1016/j.jallcom.2015.09.137
93. Mirzamohammadi S, Khorsand H, Aliofkhazraei M (2017) Effect of different organic solvents on electrodeposition and wear behavior of Ni-alumina nanocomposite coatings. Surf Coatings Technol 313:202–213. doi: 10.1016/j.surfcoat.2017.01.025
94. JCPDS (1996) International Centre for Diffraction Data. 0–45.
95. Patterson AL (1939) The scherrer formula for X-ray particle size determination. Phys Rev 56:978–982. doi: 10.1103/PhysRev.56.978
96. Kentaro Ito, Copper Zinc Tin Sulfide-Based Thin Film Solar Cells, John Wiley & Sons, United Kingdom, Chapter 5.
97. D. Abou-Ras, T. Kirchartz, U. Rau "Advanced Characterization Techniques for Thin Film Solar Cells" Wiley-VCH Weinheim Germany 7 APR 2011, Chapter 14.
98. Fernandes PA, Salom PMP (2011) Study of polycrystalline Cu 2 ZnSnS 4 films by Raman scattering. J Alloys Compd 509:7600–7606. doi: 10.1016/j.jallcom.2011.04.097
99. Dimitrievska M, Fairbrother A, Pe, ASaucedo E (2014) Raman scattering crystalline assessment of polycrystalline Cu 2 ZnSnS 4 thin films for sustainable photovoltaic technologies : Phonon confinement model. 70:272–280. doi: 10.1016/j.actamat.2014.02.035
100. Dumcenco D, Huang Y-S (2013) The vibrational properties study of kesterite Cu2ZnSnS4 single crystals by using polarization dependent Raman spectroscopy. Opt Mater (Amst) 35:419–425. doi: 10.1016/j.optmat.2012.09.031
101. Dimitrievska M, Fairbrother A, Fontané X, et al. (2014) Multiwavelength excitation Raman scattering study of polycrystalline kesterite Cu2ZnSnS4 thin films. Appl Phys Lett 104:4–9. doi: 10.1063/1.4861593

102. Scragg JJS, Choubrac L, Lafond A, et al. (2014) A low-temperature order-disorder transition in Cu2ZnSnS4 thin films. Appl Phys Lett 104:41911. doi: 10.1063/1.4863685
103. Paris M, Choubrac L, Lafond A, et al. (2014) Solid-State NMR and Raman Spectroscopy To Address the Local Structure of Defects and the Tricky Issue of the Cu/Zn Disorder in Cu-Poor, Zn-Rich CZTS Materials. Inorg Chem 53:8646–8653. doi: 10.1021/ic5012346
104. Caballero R, Garcia-Llamas E, Merino JM, et al. (2014) Non-stoichiometry effect and disorder in Cu2ZnSnS4 thin films obtained by flash evaporation: Raman scattering investigation. Acta Mater 65:412–417. doi: 10.1016/j.actamat.2013.11.010
105. Scragg JJS, Larsen JK, Kumar M, et al. (2015) Cu-Zn disorder and band gap fluctuations in $Cu_2ZnSn(S,Se)_4$: Theoretical and experimental investigations. Phys Status Solidi n/a-n/a. doi: 10.1002/pssb.201552530
106. Scragg JJS, Choubrac L, Lafond A, et al. (2014) A low-temperature order-disorder transition in Cu2ZnSnS4 thin films. Appl Phys Lett 104:41911–4. doi: 10.1063/1.4863685
107. K.Rajeshwar, “Fundamentals of Semiconductor Electrochemistry and Photoelectrochemistry,” in “Encyclopedia of Electrochemistry” (edited by S. Licht), Chapter 1, pp. 3 -53, Wiley-VCH, Weinheim (2001).
108. Jalinous, Reza LP Fundamental and Technical Aspects of TMS, Chapter 1. 1–28. doi: 10.1039/9781782620419-00001
109. Colombara D, Dale PJ, Kissling GP, et al. (2016) Photoelectrochemical Screening of Solar Cell Absorber Layers: Electron Transfer Kinetics and Surface Stabilization. J Phys Chem C acs.jpcc.5b12531. doi: 10.1021/acs.jpcc.5b12531
110. G. Biedermann HBS et al. O the SP, of the Eu3+− Eu2+ Couple. Acta Chem. Scand. 1973, 27 3761−3768. On the Standard Potential of the Eu3+− Eu2+ Couple.
111. Orazem, M. E.; Tribollet, B. Electrochemical Impedance Spectroscopy; John Wiley & Sons: Hoboken, NJ, 2008; pp 211−236.
112. Gelderman K, Lee L, Donne SW (2007) Flat-Band Potential of a Semiconductor: Using the Mott–Schottky Equation. J Chem Educ 84:685. doi: 10.1021/ed084p685
113. Ramanathan K, Keane J, Noufi R, Vista LB (2005) Properties of High-Efficiency CIGS Thin-Film Solar Cells. Natl. Renew. Energy Lab. Report, 31st IEEE Photovoltaics Spec. Conf. Exhib. Florida
114. Ramanathan K, Wiesner H, Asher S, et al. (1998) High-Efficiency Cu (In , Ga) Se 2 Thin Film Solar Cells Without Intermediate Buffer Layers.
115. Dong Z-Y, Li Y-F, Yao B, et al. (2014) An experimental and first-principles study on band alignments at interfaces of Cu_2ZnSnS_4/CdS/ZnO heterojunctions. J Phys D Appl Phys 47:75304. doi: 10.1088/0022-3727/47/7/075304
116. Kaur K, Kumar N, Kumar M (2017) Strategic review of interface carrier recombination in earth abundant Cu-Zn-Sn-S-Se solar cells: Current challenges and future prospective. J Mater Chem A 5:3069–3090. doi: 10.1039/C6TA10543B
117. Liu CC, Liang YC, Kuo CC, et al. (2009) Fabrication and opto-electric properties of ITO/ZnO bilayer films on polyethersulfone substrates by ion beam-assisted evaporation. Sol Energy Mater Sol Cells 93:267–272. doi: 10.1016/j.solmat.2008.10.016
118. Hegedus SS, Shafarman WN (2004) Thin-film solar cells: device measurements and analysis. Prog Photovoltaics Res Appl 12:155–176. doi: 10.1002/pip.518
119. Luque A, Hegedus S (2011) Handbook of Photovoltaic Science and Engineering. Handb Photovolt Sci Eng. doi: 10.1002/9780470974704
120. Lindholm FA, Fossum JG, Burgess EL (1979) Application of the Superposition Principle to Solar-Cell Analysis. IEEE Trans Electron Devices 26:165–171. doi: 10.1109/T-ED.1979.19400
121. Sinton RA, Cuevas A (1996) Contactless determination of current–voltage characteristics and minority-carrier lifetimes in semiconductors from quasi-steady-state photoconductance data. Appl Phys Lett 69:2510. doi: 10.1063/1.117723

122. Green MA (1981) Solar cell fill factors: General graph and empirical expressions. Solid State Electron 24:788–789. doi: 10.1016/0038-1101(81)90062-9
123. http://pveducation.org/pvcdrom/short-circuit-current.
124. Schroder DK Semiconductor Material and Device Characterization 2nd ed, Wiley, New York, 1998, Chapter 4.
125. Wang W, Winkler MT, Gunawan O, et al. (2014) Device characteristics of CZTSSe thin-film solar cells with 12.6% efficiency. Adv Energy Mater 4:1–5. doi: 10.1002/aenm.201301465
126. J. Tauc, R. Grigorvici and Y. Yanca, "Optical Properties and Electronic Structure of Amorphous Germanium," Physica Status Solidi, Vol. 15, No. 2, 1966, pp. 627-637. doi:10.1002/pssb.19660150224.
127. Tripathi SK, Sharma M (2012) Analysis of the forward and reverse bias I-V and C-V characteristics on Al/PVA:n-PbSe polymer nanocomposites Schottky diode. J Appl Phys. doi: 10.1063/1.3698773
128. Chen S, Walsh A, Gong X-G, Wei S-H (2013) Classification of Lattice Defects in the Kesterite Cu(2) ZnSnS(4) and Cu(2) ZnSnSe(4) Earth-Abundant Solar Cell Absorbers. Adv Mater 1522–1539. doi: 10.1002/adma.201203146
129. Chou C yi, Chen S wen (2006) Phase equilibria of the Sn-Zn-Cu ternary system. Acta Mater 54:2393–2400. doi: 10.1016/j.actamat.2006.01.014
130. K.N. Tu, Cu/Sn interfacial reactions: thin-film case versus bulk case, Materials Chemistry and Physics, 46 (1996) 217–223.
131. Wang H, Hreid T, Li J, et al. (2015) Effects of metal ions concentration on electrodeposited CuZnSn film and its application in kesterite Cu2ZnSnS4 solar cells. RSC Adv 65114–65122. doi: 10.1039/C5RA09966H
132. Lin Y, Ikeda S, Septina W, et al. (2014) Mechanistic aspects of preheating effects of electrodeposited metallic precursors on structural and photovoltaic properties of Cu2Zn SnS4 thin films. Sol Energy Mater Sol Cells 120:218–225. doi: 10.1016/j.solmat.2013.09.006
133. Wronkowska AA, Czerniak G, Wronkowski A, Skowroński (2013) Optical and microstructural characterisation of Au-Sn and Cu-Sn diffusive layers. Appl Surf Sci 281:30–37. doi: 10.1016/j.apsusc.2013.01.115
134. Y. Gamburg and G. Zangari, 2011, Theory and Practice of Metal Electrodeposition, New York, USA, Springer.
135. Weber A, Mainz R, Schock HW (2010) On the Sn loss from thin films of the material system Cu-Zn-Sn-S in high vacuum. J Appl Phys 107:1–6. doi: 10.1063/1.3273495
136. Johnson MC, Wrasman C, Zhang X, et al. (2015) Self-regulation of cu/sn ratio in the synthesis of Cu2ZnSnS4 films. Chem Mater 27:2507–2514. doi: 10.1021/acs.chemmater.5b00108
137. Jawhari T, Dimitrievska M, Fairbrother a, Saucedo E (2014) Multiwavelength excitation Raman scattering study of polycrystalline kesterite Cu 2 ZnSnS 4 thin films. 21901:1–5.
138. N. Guijarro, M. S. Prevot MS, Jeanbourquin XA, Yu X, Sivula K (2015) Autodecomposition Approach for the Low-Temperature Mesostructuring of Nanocrystal Semiconductor Electrodes Ne s. Chem Mater. doi: 10.1021/acs.chemmater.5b02894
139. Zhang Y, Ouyang S, Yu Q, et al. (2015) Modulation of sulfur partial pressure in sulfurization to significantly improve the photoelectrochemical performance over the Cu2ZnSnS4 photocathode. Chem Commun 51:14057–9. doi: 10.1039/c5cc04812e
140. Peter LM (2013) Energetics and kinetics of light-driven oxygen evolution at semiconductor electrodes : the example of hematite. 550:315–326. doi: 10.1007/s10008-012-1957-3
141. Jiang F, Ikeda S, Harada T, et al. (2014) Fabrication of an efficient electrodeposited Cu2ZnSnS4-based solar cells with more than 6% conversion efficiency using a sprayed Ga-doped ZnO window layer. RSC Adv 4:24351. doi: 10.1039/c4ra03857f

142. Emrani A, Vasekar P, Westgate CR (2013) Effects of sulfurization temperature on CZTS thin film solar cell performances. Sol Energy 98:335–340. doi: 10.1016/j.solener.2013.09.020
143. Ge J, Chu J, Yan Y, et al. (2015) Co-electroplated Kesterite Bifacial Thin-Film Solar Cells: A Study of Sulfurization Temperature. ACS Appl Mater Interfaces 7:10414–28. doi: 10.1021/acsami.5b01641
144. Altamura G, Vidal J (2016) Impact of minor phases on the performances of CZTSSe thin film solar cells. Chem Mater acs.chemmater.6b00069. doi: 10.1021/acs.chemmater.6b00069
145. Chaudhari S, Palli S, P.k. K, Dey SR (2016) Pulsed electrodeposition of Cu2ZnSnS4 absorber layer precursor for photovoltaic application. Thin Solid Films 600:169–174. doi: 10.1016/j.tsf.2016.01.021
146. Clauwaert K, Binnemans K, Matthijs E, Fransaer J (2016) Electrochemical studies of the electrodeposition of copper-zinc-tin alloys from pyrophosphate electrolytes followed by selenization for CZTSe photovoltaic cells. Electrochim Acta 188:344–355. doi: 10.1016/j.electacta.2015.12.013
147. Y Zhang, K Tse, X Xiao, J Zhu, A novel strategy to control defects and secondary phases of CZTS by surfactant Potassium - arXiv preprint arXiv:1509.00717, 2015. 4:
148. Johnson M, Baryshev S V., Thimsen E, et al. (2014) Alkali-metal-enhanced grain growth in $Cu_2 ZnSnS_4$ thin films. Energy Environ Sci 7:1931–1938. doi: 10.1039/C3EE44130J
149. Marshall G, Mocskos P, Swinney H, Huth J (1999) Buoyancy and electrically driven convection models in thin-layer electrodeposition. Phys Rev E 59:2157–2167. doi: 10.1103/PhysRevE.59.2157
150. Gonzalez G, Marshall G, Molina F, Dengra S (2002) Transition from gravito- to electroconvective regimes in thin-layer electrodeposition. Phys Rev E - Stat Nonlinear, Soft Matter Phys 65:1–8. doi: 10.1103/PhysRevE.65.051607
151. Tsui L, Mibus M, Unveroglu B, Zangari G (2016) Electrochemical Deposition of Binary Alloys : Effect of Gravity on Composition , Morphology and Dendritic Growth. 33:1–9. doi: 10.15011//jasma.33.330404
152. Redinger A, Berg DM, Dale PJ, Siebentritt S (2011) The consequences of kesterite equilibria for efficient solar cells. J Am Chem Soc 133:3320–3323. doi: 10.1021/ja111713g
153. Feng Y, Yu B, Cheng G, et al. (2015) Searching for a fabrication route of efficient $Cu_2 ZnSnS_4$ solar cells by post-sulfuration of co-sputtered Sn-enriched precursors. J Mater Chem C 3:9650–9656. doi: 10.1039/C5TC02486B
154. Altamura G, Wang M, Choy K-L (2016) Influence of alkali metals (Na, Li, Rb) on the performance of electrostatic spray-assisted vapor deposited Cu2ZnSn(S,Se)4 solar cells. Sci Rep 6:22109. doi: 10.1038/srep22109
155. Chirilă A, Reinhard P, Pianezzi F, et al. (2013) Potassium-induced surface modification of Cu(In,Ga)Se2 thin films for high-efficiency solar cells. Nat Mater 12:1107–1111. doi: 10.1038/nmat3789
156. Yatsushiro Y, Nakakoba H, Mise T, et al. Effects of Antimony Doping on Cu (In1- x , Ga x) Se2 Thin Films and Solar Cells. 5–9.
157. Sutter-Fella CM, Stückelberger JA, Hagendorfer H, et al. (2014) Sodium Assisted Sintering of Chalcogenides and Its Application to Solution Processed Cu 2 ZnSn(S,Se) 4 Thin Film Solar Cells. Chem Mater 26:1420–1425. doi: 10.1021/cm403504u
158. Ionkin AS, Fish BM, Marshall WJ, Senigo RH (2012) Use of inorganic fluxes to control morphology and purity of crystalline késterite and related quaternary chalcogenides. Sol Energy Mater Sol Cells 104:23–31. doi: 10.1016/j.solmat.2012.04.042
159. Maeda T, Kawabata A, Wada T (2015) First-principles study on alkali-metal effect of Li, Na, and K in $Cu_2 ZnSnS_4$ and $Cu_2 ZnSnSe_4$. Phys Status Solidi 12:631–637. doi: 10.1002/pssc.201400345
160. Jackson P, Wuerz R, Hariskos D, et al. (2016) Effects of heavy alkali elements in

Cu(In,Ga)Se2 solar cells with efficiencies up to 22.6%. Phys Status Solidi - Rapid Res Lett 10:583–586. doi: 10.1002/pssr.201600199

161. Carrete A, Shavel A, Fontane X, et al. (2013) Antimony-based ligand exchange to promote crystallization in spray-deposited Cu2ZnSnSe4 solar cells. J Am Chem Soc 135:15982–15985. doi: 10.1021/ja4068639
162. Chantana J, Hironiwa D, Watanabe T, et al. (2015) Bismuth-doped Cu(In,Ga)Se2 absorber prepared by multi-layer precursor method and its solar cell. Phys Status Solidi Curr Top Solid State Phys 12:680–683. doi: 10.1002/pssc.201400239
163. Tong Z, Zhang K, Sun K, et al. (2016) Modification of absorber quality and Mo-back contact by a thin Bi intermediate layer for kesterite Cu2ZnSnS4 solar cells. Sol Energy Mater Sol Cells 144:537–543. doi: 10.1016/j.solmat.2015.09.066
164. Rawat K, Shishodia PK (2016) Enhancement of photosensitivity in bismuth doped Cu 2 ZnSnS 4 thin films. 5:1–5. doi: 10.1002/pssr.201600335
165. Chen FS, Ma JS, Sung JC, Lu CH (2014) Bismuth-ion doped Cu(In,Ga)Se2 thin films: Preparation, microstructures, and electrical properties. Sol Energy Mater Sol Cells 124:166–171. doi: 10.1016/j.solmat.2013.12.023
166. Slater JC (1964) Atomic Radii in Crystals. J Chem Phys 41:3199–3204. doi: 10.1063/1.1725697
167. Himmrich M, Haeuseler H (1991) Far infrared studies on stannite and wurtzstannite type compounds. Spectrochim Acta Part A Mol Spectrosc 47:933–942. doi: 10.1016/0584-8539(91)80283-O
168. Cheng A-J, Manno M, Khare A, et al. (2011) Imaging and phase identification of Cu_2ZnSnS_4 thin films using confocal Raman spectroscopy. J Vac Sci Technol A Vacuum, Surfaces, Film 29:51203. doi: 10.1116/1.3625249
169. Wang J, Zhang P, Song X, Gao L (2014) Surfactant-free hydrothermal synthesis of Cu2ZnSnS4 (CZTS) nanocrystals with photocatalytic properties. RSC Adv 4:27805. doi: 10.1039/c4ra03444a
170. Huang D, Persson C (2013) Band gap change induced by defect complexes in Cu2ZnSnS 4. Thin Solid Films 535:265–269. doi: 10.1016/j.tsf.2012.10.030
171. Khare A, Himmetoglu B, Cococcioni M, Aydil ES (2012) First principles calculation of the electronic properties and lattice dynamics of $Cu_2ZnSn(S_{1-x}Se_x)_4$. J Appl Phys 111:123704. doi: 10.1063/1.4728232
172. Li Y, Yuan T, Jiang L, et al. (2014) Cu2ZnSnS4 thin film solar cell fabricated by co-electrodeposited metallic precursor. J Mater Sci Mater Electron 26:204–210. doi: 10.1007/s10854-014-2384-2
173. Ge J, Jiang J, Yang P, et al. (2014) A 5.5% efficient co-electrodeposited ZnO/CdS/Cu2ZnSnS4/Mo thin film solar cell. Sol Energy Mater Sol Cells 125:20–26. doi: 10.1016/j.solmat.2014.02.020
174. Pawar SM, Inamdar AI, Pawar BS, et al. (2014) Synthesis of Cu2ZnSnS4 (CZTS) absorber by rapid thermal processing (RTP) sulfurization of stacked metallic precursor films for solar cell applications. Mater Lett 118:76–79. doi: 10.1016/j.matlet.2013.12.047
175. Araki H, Kubo Y, Jimbo K, et al. (2009) Preparation of Cu2ZnSnS4 thin films by sulfurization of co-electroplated Cu-Zn-Sn precursors. Phys Status Solidi Curr Top Solid State Phys 6:1266–1268. doi: 10.1002/pssc.200881182
176. Rajeshmon VG, Kartha CS, Vijayakumar KP, et al. (2011) Role of precursor solution in controlling the opto-electronic properties of spray pyrolysed Cu2ZnSnS4 thin films. Sol Energy 85:249–255. doi: 10.1016/j.solener.2010.12.005
177. Platzer-Björkman C, Scragg J, Flammersberger H, et al. (2012) Influence of precursor sulfur content on film formation and compositional changes in Cu2ZnSnS4 films and solar cells. Sol Energy Mater Sol Cells 98:110–117. doi: 10.1016/j.solmat.2011.10.019
178. Burton L a, Colombara D, Abellon RD, et al. (2013) Synthesis, Characterization, and

Electronic Structure of Single-Crystal SnS, Sn 2 S 3 , and SnS 2. Chem Mater 25:4908–4916. doi: 10.1021/cm403046m

179. Chen S, Gong XG, Walsh A, Wei S-H (2009) Crystal and electronic band structure of Cu[sub 2]ZnSnX[sub 4] (X=S and Se) photovoltaic absorbers: First-principles insights. Appl Phys Lett 94:41903. doi: 10.1063/1.3074499
180. Lokhande AC, Chalapathy RB V, He M, et al. (2016) Development of Cu2SnS3 (CTS) thin film solar cells by physical techniques: A status review. Sol Energy Mater Sol Cells 153:84–107. doi: 10.1016/j.solmat.2016.04.003
181. Tang A, Li Z, Wang F, et al. (2017) One step electrodeposition of Cu2ZnSnS4 thin films in a novel bath with sulfurization free annealing. Appl Surf Sci 402:70–77. doi: 10.1016/j.apsusc.2017.01.079
182. Zhi J, Shurong W, Zhishan L, et al. (2017) Effects of temperature-time profile on Cu2ZnSnS4 films and cells based on sulfur-contained precursors. Mater Sci Semicond Process 57:239–243. doi: 10.1016/j.mssp.2016.10.035
183. Yang F, Ma R, Zhao W, et al. (2016) Fabrication of Cu2ZnSnS4 (CZTS) absorber films based on different compound targets. J Alloys Compd 689:849–856. doi: 10.1016/j.jallcom.2016.08.053
184. Saha SK, Guchhait A, Pal AJ (2012) Cu2ZnSnS4 (CZTS) nanoparticle based nontoxic and earth-abundant hybrid pn-junction solar cells. Phys Chem Chem Phys 14:8090. doi: 10.1039/c2cp41062a
185. Gupta GK, Dixit A (2016) Room temperature electrical properties of solution derived p-type Cu2ZnSnS4 thin films. 20678:20678. doi: 10.1063/1.4946729
186. Guchhait A, Su Z, Tay YF, et al. (2016) Enhancement of Open-Circuit Voltage of Solution-Processed Cu $_2$ ZnSnS $_4$ Solar Cells with 7.2% Efficiency by Incorporation of Silver. ACS Energy Lett 1:1256–1261. doi: 10.1021/acsenergylett.6b00509
187. Ge J, Chu J, Yan Y, et al. (2015) Co-electroplated Kesterite Bifacial Thin−film Solar Cells: a Study of Sulfurization Temperature. ACS Appl Mater Interfaces 150414102112008. doi: 10.1021/acsami.5b01641
188. Yan C, Sun K, Huang J, et al. (2017) Beyond 11% Efficient Sulfide Kesterite Cu $_2$ Zn $_x$ Cd $_{1-x}$ SnS $_4$ Solar Cell: Effects of Cadmium Alloying. ACS Energy Lett 930–936. doi: 10.1021/acsenergylett.7b00129
189. Gunawan O, Todorov TK, Mitzi DB (2010) Loss mechanisms in hydrazine-processed Cu2ZnSn(Se,S)4 solar cells. Appl Phys Lett 97:233506. doi: 10.1063/1.3522884
190. Woo K, Kim Y, Yang W, et al. (2013) Band-gap-graded Cu2ZnSn(S1-x,Sex)4 Solar Cells Fabricated by an Ethanol-based, Particulate Precursor Ink Route. Sci Rep 3:1–7. doi: 10.1038/srep03069
191. Liu X, Huang J, Zhou F, et al. (2016) Understanding the Key Factors of Enhancing Phase and Compositional Controllability for 6% Efficient Pure-Sulfide Cu2ZnSnS4 Solar Cells Prepared from Quaternary Wurtzite Nanocrystals. Chem Mater 28:3649–3658. doi: 10.1021/acs.chemmater.5b04620
192. Wang W, Shen H, Wong LH, et al. (2016) A 4.92% efficiency Cu $_2$ ZnSnS $_4$ solar cell from nanoparticle ink and molecular solution. RSC Adv 6:54049–54053. doi: 10.1039/C6RA08604G
193. Tao J, Chen L, Cao H, et al. (2016) Co-electrodeposited Cu2ZnSnS4 thin-film solar cells with over 7% efficiency fabricated via fine-tuning of the Zn content in absorber layers. J Mater Chem A 4:3798–3805. doi: 10.1039/C5TA09636G
194. Dalapati GK, Zhuk S, Masudy-Panah S, et al. (2017) Impact of molybdenum out diffusion and interface quality on the performance of sputter grown CZTS based solar cells. Sci Rep 7:1–12. doi: 10.1038/s41598-017-01605-7
195. Zhang K, Su Z, Zhao L, et al. (2014) Improving the conversion efficiency of Cu2ZnSnS4 solar cell by low pressure sulfurization. Appl Phys Lett. doi: 10.1063/1.4870508

196. Chen S, Gong X, Walsh A, Wei S-H (2009) Electronic structure and stability of quaternary chalcogenide semiconductors derived from cation cross-substitution of II-VI and I-III-VI2 compounds. Phys Rev B 79:165211. doi: 10.1103/PhysRevB.79.165211
197. Ballesteros JC, Díaz-Arista P, Meas Y, et al. (2007) Zinc electrodeposition in the presence of polyethylene glycol 20000. Electrochim Acta 52:3686–3696. doi: 10.1016/j.electacta.2006.10.042
198. Thompson MJ, Blakeney KJ, Cady SD, et al. (2016) Cu2ZnSnS4 Nanorods Doped with Tetrahedral, High Spin Transition Metal Ions: Mn2+, Co2+, and Ni2+. Chem Mater 28:1668–1677. doi: 10.1021/acs.chemmater.5b04411
199. Chen H-J, Fu S-W, Wu S-H, et al. (2016) Structural and photoelectron spectroscopic studies of band alignment at the Cu_2ZnSnS_4/CdS heterojunction with slight Ni doping in Cu_2ZnSnS_4. J Phys D Appl Phys 49:335102. doi: 10.1088/0022-3727/49/33/335102
200. Xiao C, Li K, Zhang J, et al. (2014) Magnetic ions in wide band gap semiconductor nanocrystals for optimized thermoelectric properties. Mater Horiz 1:81–86. doi: 10.1039/C3MH00091E
201. Survila A, Mockus Z, Kanapeckaite S (2000) Kinetics of Sn and Co codeposition in citrate solutions. Electrochim Acta 46:571–577. doi: 10.1016/S0013-4686(00)00633-2
202. Gómez E, Pané S, Vallés E (2005) Electrodeposition of Co-Ni and Co-Ni-Cu systems in sulphate-citrate medium. Electrochim Acta 51:146–153. doi: 10.1016/j.electacta.2005.04.010
203. Gonce MK, Aslan E, Ozel F, Hatay Patir I (2016) Dye-Sensitized Cu2XSnS4 (X=Zn, Ni, Fe, Co, and Mn) Nanofibers for Efficient Photocatalytic Hydrogen Evolution. ChemSusChem 9:600–605. doi: 10.1002/cssc.201501661
204. Chalapathy RB V, Jung GS, Ahn BT (2011) Fabrication of Cu2ZnSnS4 films by sulfurization of Cu/ZnSn/Cu precursor layers in sulfur atmosphere for solar cells. Sol Energy Mater Sol Cells 95:3216–3221. doi: 10.1016/j.solmat.2011.07.017
205. Tao J, Liu J, He J, et al. (2014) Synthesis and characterization of Cu2ZnSnS4 thin films by the sulfurization of co-electrodeposited Cu-Zn-Sn-S precursor layers for solar cell applications. Rsc Adv 4:23977–23984. doi: 10.1039/c4ra02327g
206. Guan H, Shen H, Gao C, He X (2013) Sulfurization time effects on the growth of Cu2ZnSnS4 thin films by solution method. J Mater Sci Mater Electron 24:2667–2671. doi: 10.1007/s10854-013-1153-y
207. Tsai H-W, Chen C-W, Thomas SR, et al. (2016) Facile Growth of Cu2ZnSnS4 Thin-Film by One-Step Pulsed Hybrid Electrophoretic and Electroplating Deposition. Sci Rep 6:19102. doi: 10.1038/srep19102
208. Aldalbahi A, Mkawi E, Ibrahim K FM (2016) Effect of sulfurization time on the properties of copper zinc tin sulfide thin films grown by electrochemical deposition. Nat Publ Group. doi: 10.1007/s10854-013-1657-5
209. Pawar SM, Inamdar AI, Gurav K V., et al. (2014) Growth of void free Cu2ZnSnS4 (CZTS) thin films by sulfurization of stacked metallic precursor films. Vacuum 104:57–60. doi: 10.1016/j.vacuum.2014.01.007